MOF-Enabled Confinement and Related Effects for Chemical Catalyst Presentation and Utilization

Journal:	*Chemical Society Reviews*
Manuscript ID	CS-REV-10-2021-000968.R1
Article Type:	Review Article
Date Submitted by the Author:	09-Dec-2021
Complete List of Authors:	Liu, Jian; Northwestern University, Chemistry; Argonne National Laboratory, Energy System Devision Goetjen, Timothy; Northwestern University, Department of Chemistry Wang, Qining; Northwestern University, Department of Chemistry Knapp, Julia; Northwestern University, Chemistry Wasson, Megan; Northwestern University, Yang, Ying; Northwestern University Syed, Zoha; Northwestern University, Chemistry Delferro, Massimiliano; Argonne National Laboratory, Chemical Sciences and Engineering Division Notestein, Justin; Northwestern University, Chemical and Biological Engineering Farha, Omar; Northwestern University, Department of Chemistry Hupp, Joseph; Northwestern University, Department of Chemistry

SCHOLARONE™
Manuscripts

Chemical Society Reviews

MOF-Enabled Confinement and Related Effects for Chemical Catalyst Presentation and Utilization

Received 00th January 20xx,
Accepted 00th January 20xx

DOI: 10.1039/x0xx00000x

Jian Liu,[a] Timothy A. Goetjen,[a] Qining Wang,[a] Julia G. Knapp,[a] Megan C. Wasson,[a] Ying Yang,[a] Zoha H. Syed,[a] Massimiliano Delferro,[b] Justin M. Notestein,[c] Omar K. Farha,[a,c] and Joseph T. Hupp*,[a]

A defining characteristic of nearly all catalytically functional MOFs is uniform, molecular-scale porosity. MOF pores, linkers and nodes that define them, help regulate reactant and product transport, catalyst siting, catalyst accessibility, catalyst stability, catalyst activity, co-catalyst proximity, composition of the chemical environment at and beyond the catalytic active site, chemical intermediate and transition-state conformations, thermodynamic affinity of molecular guests for MOF interior sites, framework charge and density of charge-compensating ions, pore hydrophobicity/hydrophilicity, pore & channel rigidity vs. flexibility, and other features and properties. Collectively and individually, these properties help define overall catalyst functional behaviour. This review focuses on how porous, catalyst-containing MOFs capitalize on molecular-scale confinement, containment, isolation, environment modulation, energy delivery, and mobility to accomplish desired chemical transformations with potentially superior selectivity or other efficacy, especially in comparison to catalysts in homogeneous solution environments.

1. Introduction

Chemical and physical confinement, containment, or isolation of reactants, intermediates, products, or catalysts themselves, is often key to enabling catalysis and optimizing catalytic activity, chemical selectivity, and catalyst stability. Enzymes, for example, can function well as catalysts only if they are correctly folded; see **Figure 1**.[1-2] Membranes or protein superstructures can provide the confinement needed to enforce folding and inhibit unfolding/denaturation. The folding-defined, molecular-scale spaces created on and within the enzyme itself can serve to protect the active site from poisons, bind and concentrate reactants (recall the binding component of the "Michaelis constant" in simple enzyme kinetics), define channels that facilitate water transport, ion transport, and proton transport, and define the chemical environment. The shape of a confining void-space, and the chemical functionalities the space perimeter presents, can reversibly change as reactions proceed, thereby carrying catalytic optimization to a higher level of chemical sophistication.

Rigid, abiotic, periodically porous, inorganic catalysts, such as zeolites, stand in striking chemical contrast to soft, flexible, protein-based biological catalysts. Here too, however, molecular-scale confinement – nanoconfinement – can play a defining role in chemical catalysis. A justifiably notable example is the ability of ZSM-5 (Zeolite Socony Mobil-5, a porous aluminosilicate featuring an MFI framework) to select mainly for *para*-xylene (over *ortho*- and *meta*-xylene, *i.e.* isomers of dimethylbenzene) in the methanol-based alkylation of toluene.[3-4] The selectivity is thought to arise from ZSM-5's ability to catalyse xylene isomerization in broader pores and then selectively export the least sterically demanding isomer through narrower pores,[5-6] see **Figure 2**.

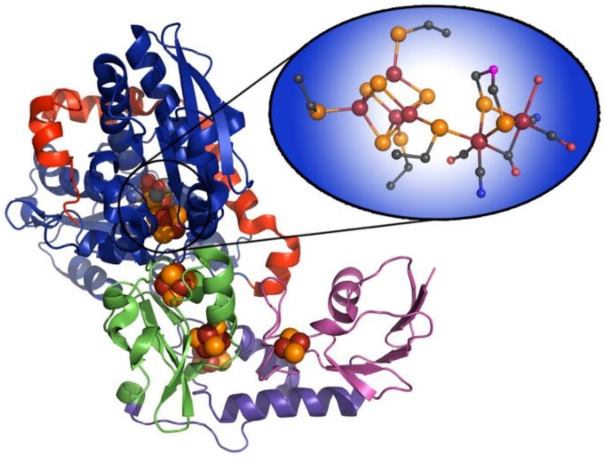

Figure 1. Ribbon representation of Clostridium pasteurianum (CpI) [FeFe] hydrogenase (an enzyme that catalyses the reversible oxidation of molecular hydrogen) with the FeS clusters and H cluster shown as space filling models, and magnification of the H cluster as ball and stick representation. The CpI domains are represented with different colors (C terminus: red, catalytic domain: blue, ferredoxin-like domains: green, purple, and magenta), and the FeS clusters and H cluster are colored to the following scheme: rust (Fe), orange (S), black (C), red (O), blue (N), and magenta (unknown). Adapted with permission from ref. 2. Copyright 2010 National Academy of Sciences.

---

[a] *Department of Chemistry, Northwestern University, 2145 Sheridan Rd., Evanston, IL 60208, United States.*
[b] *Chemical Sciences and Engineering Division, Argonne National Laboratory, Lemont, Illinois 60439, United States.*
[c] *Department of Chemical and Biological Engineering, Northwestern University, 2145 Sheridan Road, Evanston, Illinois 60208, United States*

Electronic Supplementary Information (ESI) available: [details of any supplementary information available should be included here]. See DOI: 10.1039/x0xx00000x

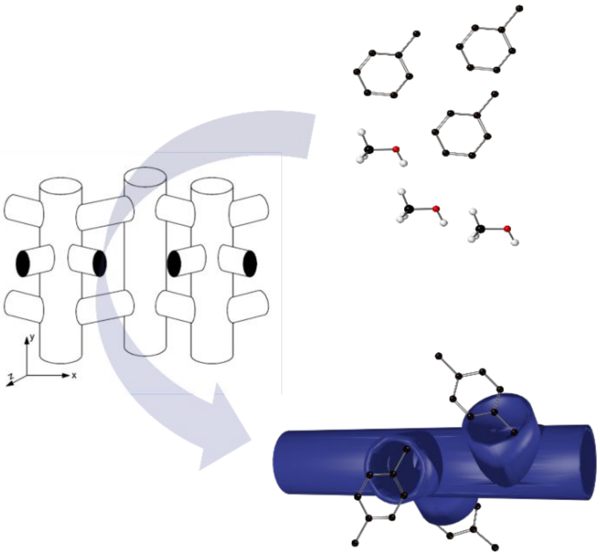

Figure 2. Representation of ZSM-5's ability to catalyse xylene formation and isomerization in broader pores and then selectively export the least sterically demanding isomer through narrower pores. Adapted with permission from ref. 6. Copyright 1997 Royal Society of Chemistry.

Dubbed "soft porous crystals" by Kitagawa,[7-8] metal–organic frameworks (MOFs), like zeolites and enzymes, can function as catalysts. Possessing both crystalline porosity and, to varying degrees, framework flexibility, MOFs comprise components that are distinctly inorganic (nodes)[9] and others that are distinctly organic (linkers). Catalytic MOFs occupy a very broad middle ground between enzymes and catalytic zeolites. Notably, one of the earliest observations of functional behaviour by MOFs was chemical catalysis – specifically, shape- and size-selective cyanylation of aldehydes.[10] Reports of MOF catalytic behaviour have proliferated at an astounding pace,[11-23] no doubt driven by an even more rapid expansion of MOF synthesis space. With synthetic versatility has come increasingly sophisticated demonstrations of catalytic functionality. Some of these demonstrations can reasonably be described as biomimetic or "zeo-mimetic." Many more, however, are better described as bio- or zeo-inspired; the chemistry is different, the implementation is different, but the underlying concepts can be traced to, or at least found in, enzymes or catalytic zeolites. Other demonstrations of MOF catalysis clearly have been inspired by the chemistry of homogeneous molecular catalysts or by classic, non-molecular, metal-oxide-supported, heterogeneous catalysts – in many cases with the aim of circumventing perceived limitations of selected examples of these catalysts. Yet other demonstrations of MOF-based catalysis are original in their presentation of catalyst structures and compositions. Aspirational goals would be selective catalytic transformations and/or catalytic mechanisms that would be difficult to envision outside the realm of MOF chemistry.

Here we highlight and review MOF-centric work that illustrates or relies upon molecular-scale confinement, containment, isolation, and related concepts such as support effects and framework-modulation of molecular transport, to present catalysts and to realize desired catalytic chemical transformations. For the most part, we focus on work published since 2015. Some of the ideas illustrated in recent work have precedents in earlier work. Rather than citing these earlier studies, we've generally pointed to more recent reviews.

The review is organized around the following ideas: (i) node-, linker-, and pore-based presentation and stabilization of catalysts; (ii) node-, linker-, and pore-based tuning of catalytic activity and selectivity, including MOF-enabled size-, shape-, regio-, and enantio-selectivity, and MOF-based catalyst support effects; (iii) MOF-defined molecular transport effects relevant to catalyst@MOF activity or selectivity; and, briefly, (iv) MOF-enabled combining of catalysts. **Figure 3** presents a simplified overview of locations and schemes for siting catalysts in MOFs. We have drawn examples from condensed-phase chemical catalysis, electrochemical catalysis, photochemical catalysis, and gas-phase-reaction catalysis.

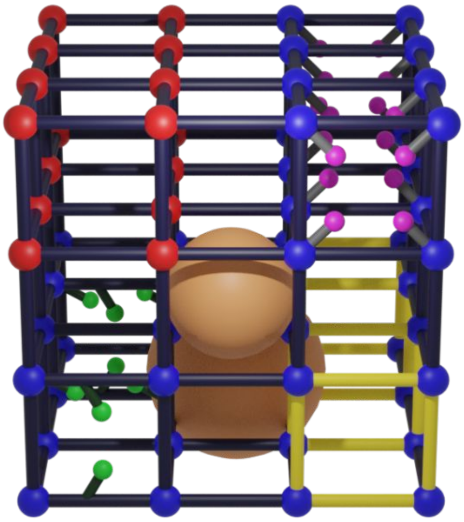

Figure 3. Potential sites in MOF structure for catalyst presentation. (top left, red) isolated nodes as catalysts, (top right, magenta) node supported catalysts, (bottom left, green) linker supported catalysts, (bottom right, yellow) cooperative behaviour between linkers and nodes, and (middle, orange) MOF encapsulated or enshrouded catalysts.

Outside the scope of the review are catalysts derived from pyrolysis of MOFs, catalyst assemblies that are arguably better described as covalent organic frameworks (COFs), catalysts involving nonporous frameworks, and catalysts based on non-crystalline coordination polymers. Also outside the scope are studies where containment, isolation, etc. constitute mainly molecule-like metal-ion coordination or ligation. Finally, "confinement" and "confinement effects" are loaded terms. In the realm of supramolecular chemistry, an area closely related in many respects to MOF chemistry and historically involving some of the same researchers, "confinement effects" include guest containment and isolation within supramolecular hosts, reactive-guest concentration and reaction acceleration within hosts, inhibition of guest aggregation, cavity-templated assembly of chemical species, chiral discrimination for guest uptake, host-based solubilization of otherwise insoluble guests, guest size- and shape-discrimination for host-guest complex formation, protection of reactive guests from exposure to potentially deleterious substances such as water, guest transport into unusual solvents, restriction of guest molecules to specific stereochemical conformations, introduction of second-

This journal is © The Royal Society of Chemistry 20xx

sphere chemical influences for guests, etc.[24-26] In the realm of conventional heterogeneous catalysis, an area closely related in many respects to MOF-based catalysis and increasingly involving some of the same researchers, “confinement” and “confinement effects” usually have much more nuanced meanings.[27] Anticipating a mixed readership, we tilted toward the narrower meanings.

2. Stabilizing and Presenting Catalysts

2.1 MOF-node-based Presentation and Isolation of Catalysts

2.1.1 Metal-ion Containing Nodes as Isolated Catalytic Sites

Nodes themselves can serve as catalysts, for which some form of isolation provides enhanced activity, selectivity, and/or stability. Generally required are nodes that are coordinatively unsaturated, or, if saturated, then, in addition to linkers, the node requires either: a) nonstructural ligands that are easily displaced by reactants, or b) nonstructural ligands that are redox-integrated with node metal ions – for example, hydroxo ligands that lose protons and become oxo ligands upon increase in metal-ion oxidation state. In this subsection, examples of using MOF nodes as catalysts will be discussed, including MOF nodes as stabilizers of reaction intermediates, as open metal sites for substrate adsorption, as Lewis acid sites, and as redox mediators.

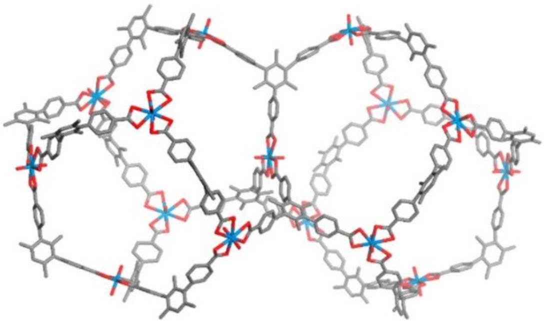

Figure 4. Portion of crystal structure representation of NU-1301, showing uranyl nodes isolated in 3-dimensional space. Uranium (blue), oxygen (red), carbon (gray), and hydrogen omitted for clarity. Adapted with permission from ref. 29. Copyright 2020 American Chemical Society.

An insightful perspective article by Young, *et al.*[28] likens MOF-node-based metalation and related ideas (including those in **Section 2.1.2**) to matrix isolation, where the goal often is to access unusual chemistry, or chemical properties, that would be lost if species dimerized. A striking example is NU-1301, a MOF with **nun** topology that features linker-isolated uranyl ion (single $[U^{VI}O_2]^{2+}$) units as nodes; see **Figure 4**.[29] The uranyl ion is an extraordinarily strong photo-oxidant (based on ligand-to-metal charge-transfer excitation with blue light), making it effective even as a fluorination catalyst. Isolation of the ions as framework nodes stabilizes the intermediate form of the catalyst, $[U^{V}O_2]^{+}$, against disproportionation into $[U^{VI}O_2]^{2+}$ and insoluble U(IV) species.

Chemical elaboration of the metal ions already present in secondary building units (SBUs)[9] to create more catalytically active species has been realized in many forms.[30-33] For instance, Lin and co-workers[33] transformed a Zr site within the Zr_6 node of MOF-808[34] (also called Zr-BTC, $Zr_6(\mu_3\text{-}O)_4(\mu_3\text{–}OH)_4(BTC)_2(HCO_2)_6$, where BTC = 1,3,5-benzene tricarboxylate and the framework topology is **spn**) into an organometallic species through a stepwise process consisting of removal of residual, nonstructural formate ions, treatment with Me_3SiCl to form a Zr-Cl species, and finally alkylation with alkyl lithium reagents to get ZrR_2-BTC (R = CH_2SiMe_3 or Me). ZrR_2-BTC is inactive for olefin polymerization due to coordinative saturation of Zr sites. But, an *in situ* generated ZrMe-BTC catalyst (**Figure 5**) displays high activity for ethylene polymerization, producing polyethylene with physical properties consistent with a single-site catalyst.

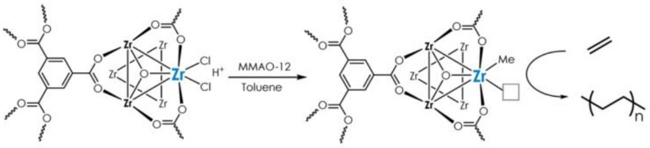

Figure 5. Schematic of the synthesis of ZrMe-BTC for ethylene polymerization. Adapted with permission from ref. 33. Copyright 2017 American Chemical Society.

The partial absence of expected linker molecules at the nodes of MOFs, a common occurrence with nominally twelve-linker-connected UiO-type MOFs (UiO is University of Oslo), can influence catalytic activity for certain chemical transformations by exposing additional node-based coordination sites that present Lewis acid sites, and/or present Brønsted acidic sites.[35-37] Recall that UiO-type MOFs feature hexa-zirconium(IV)-oxy clusters as nodes, with the nodes displaying high affinity for carboxylate-terminated linkers and very high affinity, at defect sites, for phosphonate-terminated ligands. Intentionally altered synthesis conditions can yield reproducibly “defective” frameworks, characterized by missing linkers, missing nodes, or both.[38-41] Small changes in synthesis conditions, particularly with Zr(IV) building blocks and tetratopic linkers, can yield strikingly different MOF topologies with differing pore structures and, at nodes, differing numbers and locations of linker-bound sites versus open coordination sites.[37, 42-43] In some cases these differences can translate into varying reactant confinement and/or catalyst-access effects, as discussed in later sections. Homologous Hf(IV), Ce(IV), and Th(IV) nodes can yield altered catalytic behaviour.[44] While under-explored, Ce(IV), with its ability to reduce to Ce(III) at fairly positive potentials, opens up the opportunities for redox catalysis,[45] linker-to-node charge-transfer photocatalysis,[46] and oxygen-vacancy creation for subsequent binding and activation of molecular oxygen as a co-reactant for chemical catalysis,[47-48] as well as tuneable Lewis and Brønsted acid properties.[49]

Gates and co-workers[50-51] have provided insight into the structure and tuning of defect sites within Zr-based MOFs and the corresponding reactivity with their studies on UiO-type MOFs. Investigating the node chemistry with ethanol dehydrogenation revealed that nonstructural capping ligands as well as linkers themselves are replaced by ethanol, with more highly defective versions of the materials degrading more readily with increasing time on stream. Evidently, for this reaction, there exists a fine balance regarding optimal defect density, with higher density contributing to higher catalytic activity and lower density to greater stability. It is worth noting that for MOFs in the UiO series, catalysis based on Zr(IV) access is impossible, unless linkers are missing or incompletely connected. Nevertheless, fully twelve-connected oxy-Zr_6 nodes can still present Brønsted acid sites, in the form of bridging hydroxo ligands.

Fang *et al.*[52] organized octa-nickel(II)-oxy nodes within PCN-601 (PCN: porous coordination network) by using pyrazolate-terminated porphyrins as linkers; see **Figure 6**. Notable features of the nodes are their ability to accept electrons reversibly, to deliver electrons catalytically to reducible substrates such as CO_2, and to resist degradation by CO_3^{2-} or HCO_3^{-}. These species are typically present when the catalyst substrate is CO_2 in water. Unfortunately, otherwise chemically stable Zr(IV)-, Hf(IV)-, and Al(III)-carboxylate MOFs tend to be degraded by aqueous bicarbonate and, especially, carbonate.[53]

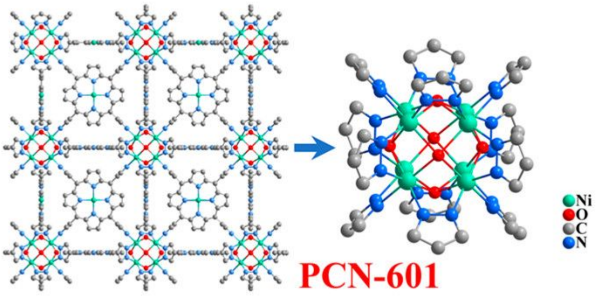

Figure 6. Structural representation of MOF PCN-601 (left) and Ni_8 node (right). Nickel (green), oxygen (red), carbon (gray), nitrogen (blue), and hydrogens omitted for clarity. Adapted with permission from ref. 52. Copyright 2020 American Chemical Society.

The nodes of PCN-601 are somewhat unusual in resisting degradation during redox cycling; metal-ligand bond strengths and associated lability are typically strongly dependent on metal oxidation-state, such that overall MOF stability/instability is likewise strongly connected to the oxidation-state of node metal ions. Nevertheless, oscillation between metal-ion oxidation states is often key to catalytic activity. To deal with this conundrum – catalytic activity at the expense of framework stability – Dincă and co-workers[54] cannily exploited partial cation exchange (also termed post-synthetic metalation, metal metathesis or transmetalation).[55-58] Specifically, they implemented single-metal-ion exchange in the Zn_4O nodes of MOF-5 ($Zn_4O(BDC)_3$ (**Figure 7**), where BDC^{2-} is benzene-dicarboxylate, *i.e.* terephthalate, and in the dinuclear metal nodes of MFU-4 ($Zn_5Cl_4(BTDD)_3$ (**Figure 7**), H_2BTDD = bis(1*H*-1,2,3-triazolo[4,5-*b*],[4′,5′-*i*])dibenzo[1,4]dioxin) and related compounds.[59-66] Under framework-synthesis and subsequent MOF-catalysis conditions, node-based Zn(II) is redox-inert, and sufficient zinc is present both to enable initial assembly and to retain MOF structural integrity after partial trans-metalation. Note that similar trans-metalation is, unfortunately, not feasible with hexa-Zr(IV)-oxy nodes.[67]

Zhou and co-workers[68] showed that subjecting Mg(II)-MOF-74 (**Figure 7**) to trans-metalation with Ti(III), followed by oxidation, can yield the otherwise inaccessible compound, Ti(IV)-MOF-74. The titanium compound is considerably more chemically robust than the parent MOF. More importantly, the modified material's oxy-titanium chains (rod-like secondary building units) are anticipated to behave similarly to the wide-bandgap semiconductor TiO_2 in terms of photophysics and photocatalytic activity. PCN-333 (Sc(III)), MIL-100(Sc(III)) (MIL: Materials from Institut Lavoisier), and Zn(II)-MOF-74 (**Figure 7**) were similarly converted to potentially photo-active form by partial or full trans-metalation by Ti(III), followed by oxidation to Ti(IV).[68]

Several groups have shown that the octa-titanium(IV)-oxy nodes of MIL-125(Ti),[69] like the infinite chains of MOF-74(Ti) (**Figure 7**), can be treated as tiny fragments of the UV-photo-catalytic and surface-redox-active bulk semiconductor TiO_2[70] (note also the Ti containing zeolite ETS-10). MIL-125(Ti) features BDC^{2-} linkers. Amino (or bis-amino) functionalization of the linker[71-72] serves to shift light-absorption and photocatalytic behaviour into the visible region.[70, 73-74] Replacement of one or two of the node titanium ions in MIL-125 with V(III), V(IV), Sn(IV), Cu(II), Nb(V) or other metal ions[75-77] further diversifies the properties, including catalytic properties.

Yaghi and co-workers[79] showed that planar, potentially catalytic, Anderson-type polyoxometalates (POMs) can be isolated and presented in guest-accessible fashion by condensing tetrahedral/tetratopic aldehyde-terminated linkers with amine-functionalized POMs to yield a triply catenated framework, MOF-688 that, nonetheless, exhibits useable porosity; see **Figure 8**.

Fan, *et al.*[80] investigated a Co-based MOF for C-H oxidation of arylalkanes that exhibited high selectivity towards mono-ketone products based on a size selection effect, and excellent catalytic activity based on presentation of a high density of Lewis acid sites. Stavila, *et al.*[81] examined an isoreticular series of Mg-based MOFs, IRMOF-74(I–IV) (IRMOF = isoreticular metal–organic framework) for C=O hydrogenolysis and found that IRMOF-74(III) exhibited unexpectedly high activity relative to smaller and larger members of the series. This enhanced activity was traced to a seemingly minor structural distortion, unique to IRMOF-74(III), that enhances reactant access to Mg(II), the apparent active-site.

2.1.2 Catalytic Metal Ions and Clusters Grafted to MOF nodes

Zr-based MOFs have strong bonds between nodes and linkers, and good thermal and chemical stability, which have been extensively explored for heterogeneous catalysis reactions.[53,82] A common Zr node core composition is the $[Zr_6(\mu_3\text{-}O)_4(\mu_3\text{-}OH)_4]^{12+}$ cluster, which may be 4-,[83] 5-,[84] 6-,[34] 8-,[85] 9-,[86] 10-,[87] or 12-connected[88] depending on synthesis conditions and on the choice of polytopic carboxylate-based ligand. Ideally, bridging or terminal hydroxo and/or aqua node ligands can react with metal ions, labile inorganic complexes, or organometallic complexes, either in the condensed phase (often termed **s**olvothermal deposition **i**n **M**OFs (**SIM**)) or *via* molecular volatilization into the vapor phase (often termed **a**tomic layer deposition **i**n **M**OFs (**AIM**)) to accomplish chemical attachment.[89-97] Subsequent treatment with steam or H_2S can yield node-grafted oxy- or sulfido-metal species – either as individual metal ions or as few-atom clusters.[98-99] A majority of the transition-metal elements and a handful of main-group metals have now been grafted in this way to Zr-MOF nodes. SIM is preferred over AIM if single-crystal X-ray structures of grafted catalysts are desired. Larger clusters, including mixed-metal clusters, can be formed by repeating the two-step installation cycle[100] (**Figure 9**). The need for two steps serves to make individual cycles self-limiting with respect to metal-ion loading.

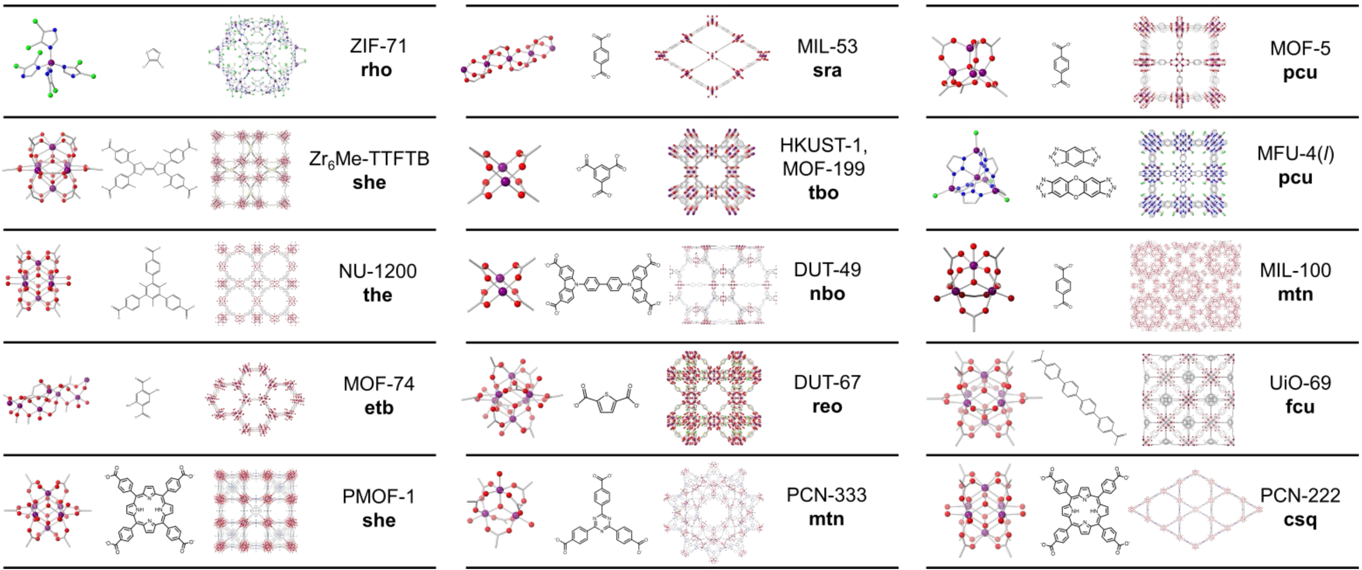

Figure 7. Presentation of MOF SBU (node) unit and linker structures for frameworks that are not shown in other figures. Bold, three-letter sequence indicates topology, which can be obtained from Reticular Chemistry Structure Resource (RCSR) Database[78]. Note: generic metal is shown in purple for each node and MOF structure – many structures can accommodate a variety of metal nodes. Atom colors: carbon (gray), nitrogen (blue), oxygen (red), chlorine (green), interchangeable metal (purple or magenta).

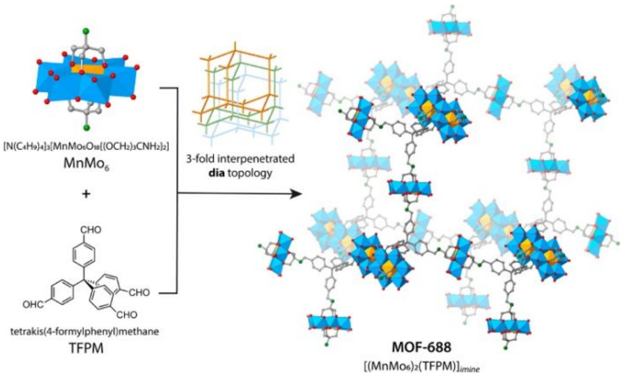

Figure 8. Synthetic strategy and structure illustration of MOF-688. Adapted with permission from ref. 79. Copyright 2019 American Chemical Society.

Cluster-based nodes can be viewed as tiny islands comprising crystallographically well-defined fragments of conventional metal-oxide supports.[101] Metal ions attached by grafting to conventional metal-oxide supports typically are effectively retained, especially when used as catalysts for gas-phase reactions. Nevertheless, the grafted ions also typically are mobile, and therefore can consolidate/sinter – in turn, altering their behaviour as catalysts. Organic linkers have proven remarkably effective at preventing migration of metal ions from one node to another.[102-103] Thus, sintering of grafted metal ions as metal-oxides or -sulfides generally is absent in MOFs, or tends to be limited to consolidation of a small number of isolated ions on a single node. (In contrast, and as discussed later, zero-valent metal atoms and clusters tend to be mobile across organic linkers/spacers and minimally adhesive to metal-oxide nodes,[104] resulting in formation of metal(0) nanoparticles containing tens, hundreds, or thousands of metal atoms.) In this subsection, examples of MOF-enabled metal-ion or oxy-metal-cluster isolation and subsequent stabilization against either condensed-phase leaching or gas-phase sintering will be discussed.

Figure 9. Low-resolution difference-electron-density (DED) image of CoAIM-MSIM-NU-1000 showing deposition location of M (M= Ni(II), Zn(II), Al(III), Ti(IV) or Mo(VI)) and Co(II) ions in NU-1000. (a) Co(II) ions are sited on top of Ni(II)/Al(III)/Ti(IV) ions; (b) Co(II) and Mo (VI) ions are sited on different locations on the node (blue, Co; pink, Mo); (c) Co(II) ions are sited on both Zr_6 nodes and Zn(II) ions. Adapted with permission from ref. 100. Copyright 2017 American Chemical Society.

Abdel-Mageed, *et al.*[105] reported a UiO-66-supported (nominally $Zr_6O_4(OH)_4(BDC)_6$, **fcu** topology) single-atom Cu(II) catalyst, Cu/UiO-66, which is active and stable for CO oxidation by O_2 at temperatures up to 350 °C (**Figure 10**). The single Cu atoms were anchored to the oxygen atoms of –OH and $–OH_2$ ligands that cap the defect sites on the oxy-$Zr(IV)_6$ nodes. *Operando* spectroscopy measurements indicated that the activity of the catalyst is due to atomically dispersed, positively charged copper.

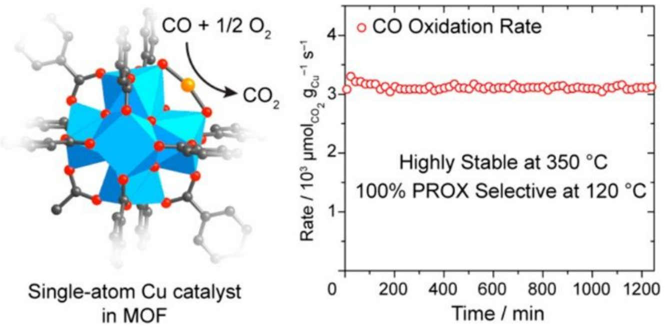

Figure 10. UiO-66-supported single-atom Cu catalyst is highly active and stable for CO oxidation at temperature up to 350 °C. Adapted with permission from ref. 105. Copyright 2019 American Chemical Society.

Li, *et al.*[102] found that AIM-synthesized tetra-Ni(II)-oxy clusters can be stabilized on Zr_6 nodes of NU-1000 (NU: Northwestern University, $Zr_6(\mu_3–O)_4(\mu_3–OH)_4(H_2O)_4(OH)_4{}^{8+}$ nodes and tetratopic 1,3,6,8-tetrakis(p-benzoate)pyrene ($TBAPy^{4-}$) linkers, **csq** topology). The cluster structure was ascertained *via* a battery of synchrotron-enabled X-ray absorption and scattering experiments, together with DFT-based computational modelling and subsequent simulation of spectroscopic signatures of candidate structures. The thermal disorder accompanying exothermic AIM reactions tends to preclude structure assessment by single-crystal X-ray diffraction measurements, although DED analyses of X-ray scattering can be effective for approximately identifying catalyst locations, as illustrated, for example, by **Figure 11**.[102, 106] Consistent with an absence of sintering, node-grafted tetra-nickel(II) clusters on NU-1000 show persistent activity and unchanging turnover frequencies (TOFs) for gas-phase ethylene hydrogenation over the course of two weeks online.[102] In contrast, ALD-nickel(II) on zirconia powder shows kinetic evidence of sintering after two hours online; see **Figure 11a**. Post-catalysis investigation reveals the formation of nanoparticles on zirconia powder, but not on/in the MOF-based support.

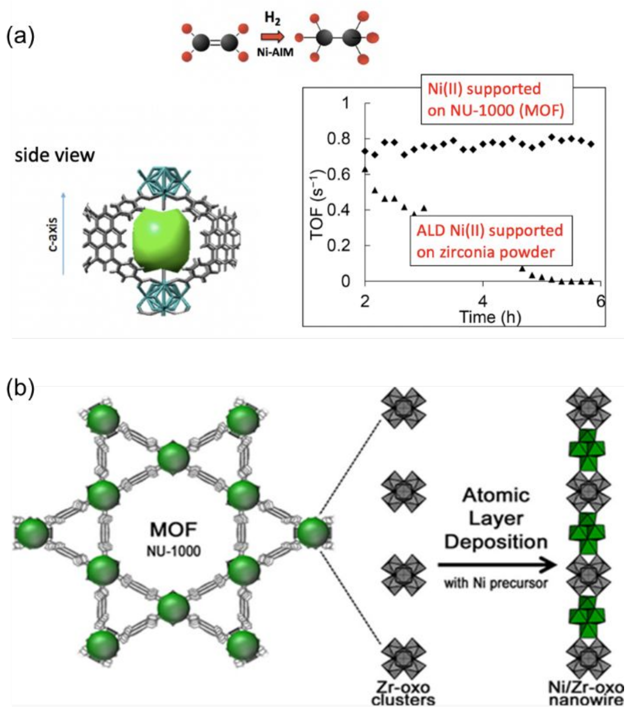

Figure 11. (a) Tetra-Ni(II)-oxy clusters on NU-1000 for ethylene conversion showing sintering resistant feature; (b) Zr-oxo/NiO_xH_y nanostrands along the MOF *c* direction. Adapted with permission from refs. 102 and 106. Copyright 2016 and 2017 American Chemical Society.

Numerous other examples exist for metal-ion isolation and subsequent stabilization against either condensed-phase leaching or gas-phase sintering.[105, 107-113] A case that merits highlighting comes from Otake and co-workers[114] who introduced vanadium ions onto the nodes of Zr-NU-1000 and Hf-MOF-808 (also called Hf-BTC, or $Hf_6(\mu_3\text{-}O)_4(\mu_3–OH)_4(BTC)_2(CH_3COO)_6$; BTC = 1,3,5-benzene tricarboxylate; topology = **spn**). Metal-oxide-supported oxy-vanadium species are effective catalysts for numerous oxidation reactions.[115] Detailed mechanistic investigations, especially, with regard to the dependence of catalyst activity on metal nuclearity, have often been complicated, however, by the propensity for initially isolated vanadium ions to migrate and sinter. Otake and co-workers employed SIM for their installation studies, so were able to obtain single-crystal X-ray structural data. These measurements established that, under dilute conditions, vanadium is installed in single-metal-ion form, with no more than one vanadium atom (ion) per node. These are conditions for precluding sintering. The X-ray measurements revealed that vanadium is sited differently on each of the two node-types examined – a somewhat surprising result, given the superficial similarities of the various nodes. Furthermore, on MOF-808 three crystallographically distinct, *i.e.*, nonequivalent, single-atom "bridging" vanadium motifs are observed, with these converging, with heating, to one type of "bridging" site (**Figure 12**). These minor structural differences translate to a three-fold rate difference for a model reaction, condensed-phase oxidation of 4-methxoylbenzyl alcohol.

Regardless of the details, the vanadium examples indicate or suggest that: a) energetically similar catalyst configurations can co-exist when MOF nodes are used as supports, b) even well-defined structures for MOF-supported catalysts can, of course, evolve, and c) in favourable cases, MOF-supported arrays of catalysts can be obtained with precise structural uniformity – valuable information for predictive and mechanistic computational modelling of catalytic behaviour.[116-120]

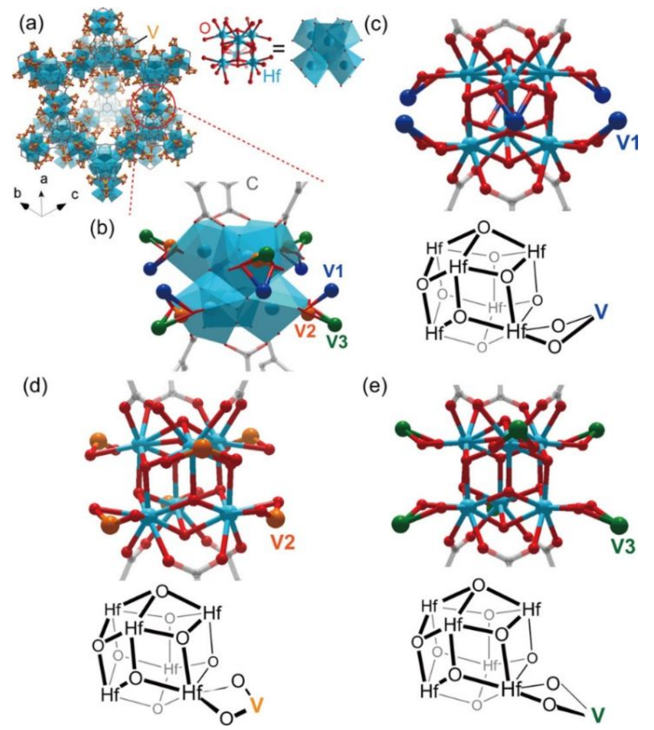

Figure 12. (a) & (b) Crystal structures of Hf-MOF-808-V collected at 100 K, where V1 (blue), V2 (red-orange), and V3(green) sites are three distinct nonequivalent single-atom "bridging" vanadium sites. (c), (d), & (e) the detailed node structures of Hf-MOF-808-V1, V2, and V3 for clarity. Heating led to conversion of structures V1 and V3 to a single site, V2. The various vanadium species feature coordination numbers larger than two, but the chemical identities of only two could be unambiguously identified. Adapted with permission from ref. 114. Copyright 2018 American Chemical Society.

Please do not adjust margins

Thompson, *et al.*[121] presented a strategy for installing heterometallic active-sites on Zr_6 nodes within NU-1000 by employing heterobimetallic coordination complexes as precursors; see **Figure 13**. The bimetallic coordination compound, $(py_3tren)AlCoMe$ (py_3tren = *N*,*N*,*N*-tris(2-(2-pyridylamino)ethyl)amine), was grafted to the node of NU-1000 *via* solvothermal deposition, with the organic ligands then being eliminated by heating in air. While the structure of the resulting dinuclear, bimetallic catalyst is not known, the approach does fix the stoichiometry and metal composition of the catalyst at the single-node level.

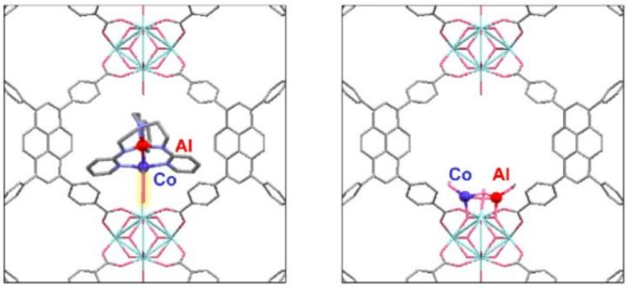

Figure 13. (left) Single, isolated Co–Al complexes were immobilized within NU-1000. (right) Heating the anchored Co–Al complex on NU-1000 leads to a Co–Al oxide cluster on NU-1000. The drawings are meant to convey plausible structures, not crystallographically confirmed structures. Adapted with permission from ref. 121. Copyright 2016 American Chemical Society.

Baek, *et al*.[122] post-synthetically modified the nodes of MOF-808 with imidazole-presenting ligands. Pairs of these ligands can subsequently coordinate and stabilize a dimeric Cu(I) species. The motivation, in part, was the similarity of imidazole and the amino acid, histidine. The latter is known to coordinate copper-based active-sites in soluble methane monooxygenase (sMMO), an enzyme that is remarkably effective for selective partial oxidation of methane to methanol.[123] Additionally, when the Baek work was published, a near-consensus view was that the active-site in sMMO featured a pair of copper ions. (Subsequently, the sMMO active-site was found to contain a single copper ion.)[124] Regardless, the study provided an impressive illustration of how pore-modification chemistry can be adapted to create artificial sites that incorporate key features of putative active-sites in metalloenzymes.

The Cu(I) sites within imidazole-modified MOF-808 were treated with N_2O to form a bis(μ-oxo) dicopper species, which could activate methane to methanol with 100% selectivity at 150 °C. Given a very low turnover number, TON (*ca.* 0.02 mol/mol_{Cu}), it is unclear whether the observed selective oxidation is catalytic. (While generally not practical for manufacturing-scale chemistry, N_2O is an attractive candidate oxidant for selected mechanistic studies because it dispenses with the chemical problem of how to deal with a second oxygen atom – a potentially complication when using O_2 or peroxide species with well-defined catalysts.)

In similar fashion to various Zr-MOFs, frameworks featuring Al(III)- or Ti(IV)-containing nodes,[112, 125] have been shown by Feng, *et al*.[126] to be suitable for grafting in stable form, *via* μ_2–OH groups, potentially catalytic Co and Fe ions. Most recently, this group, led by Lin,[110] demonstrated that either a single Cu^{2+} or a $Cu_2(\mu_2\text{–}OH)_2$ unit could be grafted to the otherwise hollow centre of the octa-nuclear, ring-shaped node of MIL-125-Ti (**Figure 14**), where both mono-cuprate and di-cuprate forms are capable of binding and activating dioxygen.

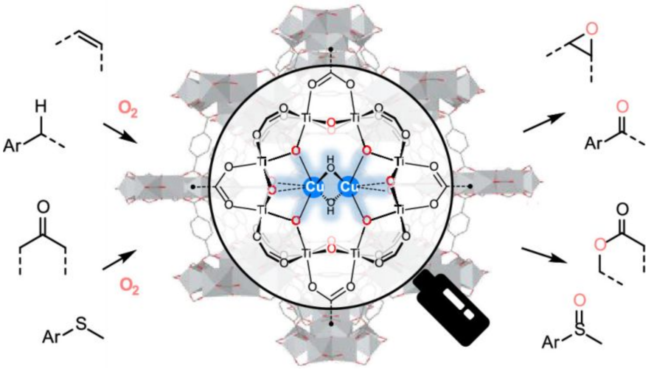

Figure 14. $Cu_2(\mu_2\text{–}OH)_2$ unit grafted to the hollow centre of Ti_8 node in MIL-125-Ti are capable of binding and activating dioxygen. Adapted with permission from ref. 110. Copyright 2021 American Chemical Society.

2.1.3 Isolated Molecular Catalysts Grafted to MOF Nodes

Directly grafting catalytic inorganic or organometallic complexes to MOF nodes tends to yield benefits typical of heterogenization of molecular catalysts, including site-isolation and simplified separation of catalysts from reaction products; indeed, there exist many examples. Of special interest, however, is the potential for unveiling (or further unveiling) structures of complexes known from heterogenization on amorphous silica, and more recently on crystalline metal-oxides, to display unusually high activity or selectivity. As it is often cited as a conceptual starting point in studies involving MOFs, the pioneering work of Basset should be noted,[127-128] along with his emphasis on gaining predictive mechanistic understanding by "enter(ing) the catalytic cycle of a given reaction by a suitable predefined Surface Organometallic Fragment."[129] Most readily grafted are molecular catalysts that feature ancillary oxo or hydroxo ligands that can be shared with nodes, or that present pendant carboxylates, phosphonates, or similar species that have affinity for metal-oxy nodes (or other functionalities for non-oxy nodes).[130-131]

By way of illustration (**Figure 15**), De Vos, *et al*.[132] grafted thioether-containing carboxylate ligands to the node of Zr-MOF-808. Specifically, tetrahydrothiophene-2,5-dicarboxylic acid (**L1**) was grafted at a density of ~2 per node. In principle, MOF-808 can accommodate up to five nonstructural carboxylate ligands. Following **L1** metalation with Pd(II), the catalytic activity for the oxidative alkenylation of an arene was studied. The MOF-808-**L1**-Pd(II) catalyst eventually degrades, yielding Pd(0) nanoparticles, as evidenced by Pd-Pd interactions in extended X-Ray absorption fine structure (EXAFS) measurements and as seen in high-angle annular dark-field scanning transmission electron microscopy (HAADF-STEM) images.

While examples relying upon oxy-$Zr(IV)_6$ nodes are most common,[131-135] examples based on oxy-$Ti(III)_2Ti(VI)_6$,[112] oxy-$Hf(IV)_6$,[136] hydroxo-Al(III) (*i.e.*, Al-MIL-53 in **Figure 7**),[126] and other nodes/clusters can be found, especially in cases where the distinction between grafted molecular catalysts and grafted single-

Please do not adjust margins

metal-atom catalysts becomes blurred. Also, while node-grafted molecular catalysts typically feature transition metals, grafting with main-group $Mg(CH_3)_2$ to realize $m_3\text{-}O\text{-}Mg\text{-}CH_3$ on a hexa-Zr(IV) node, has been demonstrated by Lin and co-workers,[113] who further showed that the species is catalytically competent for hydroamination and hydroboration. The parent MOF is a nominally twelve-connected derivative of UiO-69 (*i.e.*, functionalized tetraphenyl-dicarboxylate linkers connected to $Zr_6(\mu_3\text{-}O)_4(\mu_3\text{-}OH)_4^{12-}$). In contrast to most examples, but not without precedent,[137] grafting is believed to rely upon reaction with bridging hydroxo ligands, rather than with intentionally introduced or defect-enlisted, terminal oxy ligands.

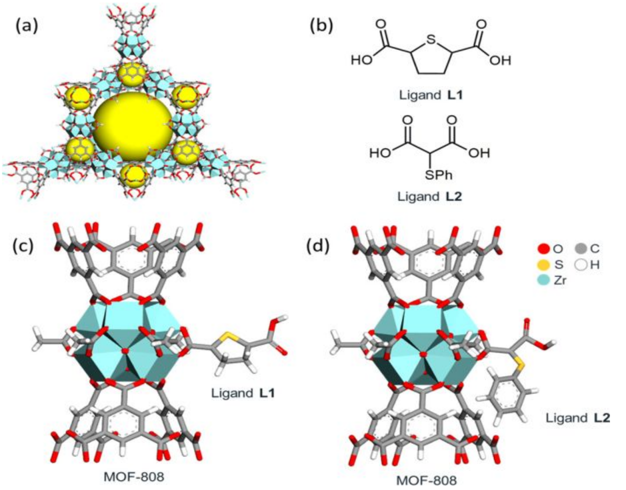

Figure 15. Structural representation of MOF-808 with its pores highlighted by yellow spheres (a), the thioether ligands L1 and L2 (b), MOF-808-L1 (c), and MOF-808-L2 (d). The Zr, O, C, H, and S atoms are represented in the structure models by turquoise, red, gray, white, and yellow sticks, respectively. Adapted with permission from ref. 132. Copyright 2020 American Chemical Society.

2.2 MOF-Linker-Based Presentation and Isolation of Catalysts

MOF chemistry has a long history of directly employing catalytically active coordination complexes as linkers for framework construction and subsequently for chemical catalysis.[138-142] The motivations include enabling catalyst separation from reaction mixtures, facilitating catalyst recycling, enhancing selectivity, enhancing catalyst stability, positioning catalysts within desirable spatially and/or chemically defined pores, and isolating catalysts from each other or from potential poisons. In this section, we will discuss post-synthetic functionalization of MOF linkers to create framework-immobilized molecular catalysts. Published examples include linkers presenting vacant bipyridine (bpy),[143-150] phenanthroline,[151-153] thiocatechol,[154] catechol,[92,155-156] porphyrin,[157-159] and other coordination-friendly functionalities.[160-163]

An inherent challenge with the post-synthetic installation approach is that the chemical moieties intended for metal-complex or isolated-metal-ion binding may already be binding components used to assemble the MOF. For example, linkers containing free-base porphyrins can recruit metal ions intended for use only in MOF nodes. A seminal discovery and realization by Cohen, *et al.*,[143] was that for ubiquitous UiO-type MOFs and related MOFs, the linker itself, provided that it is ditopic, can be exchanged and installed after the MOF is already synthesized (**Figure 16**). PSE (post-synthetic exchange) or SALE (solvent-assisted linker exchange) was known, but it had generally been assumed that because zirconium-oxygen bonds are strong, they also would be substitutionally inert. This turns out not to be the case and carboxylate-terminated, ditopic ligands can be remarkably labile. Bipyridine ligands have been incorporated extensively in numerous MOFs, both as linkers and as tethered nonstructural ligands, and then used to heterogenize numerous kinds of catalysts.[144-150, 164-166] **Figure 17** shows one example.[145]

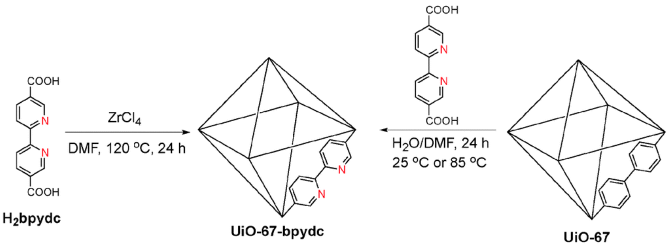

Figure 16. Synthetic scheme of incorporating bpy into the MOF, resulting in chelation sites for metalation. Adapted with permission from ref. 143. Copyright 2014 Royal Society of Chemistry.

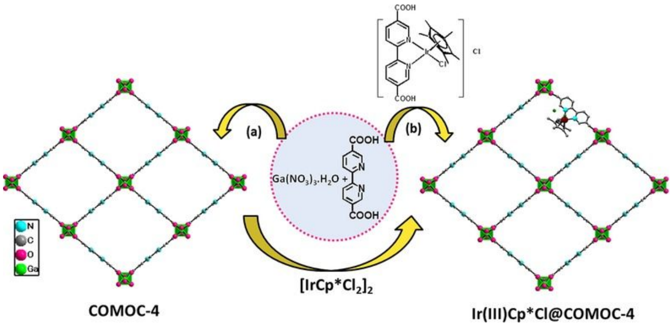

Figure 17. Incorporation of bpy into the MOF which can then be metalated with Ir precursors. Adapted with permission from ref. 145. Copyright 2016 John Wiley and Sons.

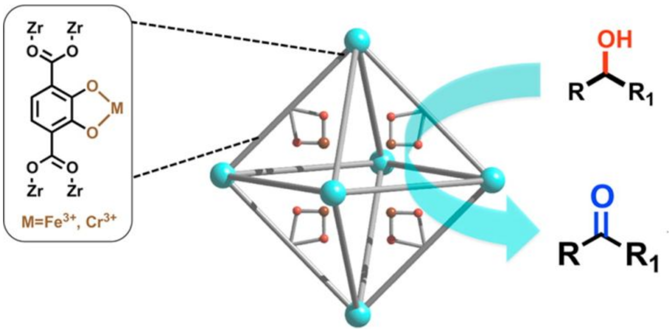

Figure 18. UiO-66 supported metal-monocatecholato species as alcohol oxidation catalysts. Adapted with permission from ref. 155. Copyright 2014 American Chemical Society.

Further work by Cohen, *et al.*[155] focused on incorporating catechols as nonstructural components of linkers – again in UiO-type MOFs. Incorporation was accomplished by combining post-synthetic deprotection (PSD) and post-synthetic exchange (PSE). **Figure 18** presents a specific example. Of perhaps broader significance, however, is that MOF-localization of the catechol functionality permits *mono*-catecholate complexes of labile metal ions to be formed, without disproportionation of these into catechol-free and multi-catechol species (as would occur with ligands and metal ions in free solution). An under-explored idea in MOF coordination chemistry is that framework-immobilization of one type of chelating ligand sets the stage for quantitative formation of bis-heteroleptic complexes, but without the potential for partial disproportionation into the corresponding homoleptic complexes.

Figure 19 presents an example of chemical orthogonality for bifunctional linkers/ligands. Briefly, when deprotonated the three carboxylates of H_3**P1** react with Zr(IV), but the phosphine functionality does not. Thus, the phosphine remains available for post-synthetic binding of suitable catalysts. Lin, *et al.*[167] pointed out that in homogeneous solution environments, that catalytically competent, monophosphine-iridium (or rhodium) complexes can disproportionate into less functional or nonfunctional diphosphine and phosphine-free coordination complexes. Isolation and immobilization of monophosphine-presenting ligands, as in the MOF Zr-P1 (**Figure 19**), precludes and prevents undesirable disproportionation.[142]

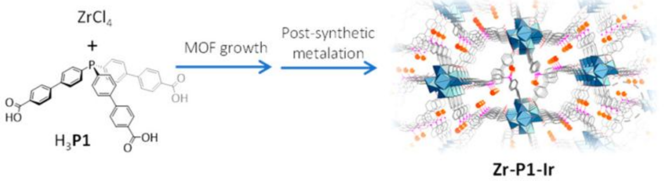

Figure 19. Monophosphine-presenting linker used for carboxylate-based formation of a Zr-MOF, and then treated with iridium (or rhodium) to make catalysts that resist coordinative disproportionation. Adapted with permission from ref. 167. Copyright 2019 American Chemical Society.

Dincă, *et al.*[168] have explored the *de novo* installation of catalytic or pre-catalytic metallo-ligands into MOFs. **Figure 20** provides an example; 1,1′,1′′-methanetriyltris(3,5-dimethyl-1*H*-pyrazole-4-carboxylic acid) (TpmC*) was used as the linker, which formed a MOF in the presence of $ZrOCl_2$ and copper(I)iodide with benzoic acid as the modulator. C_{3v} symmetry needed to be maintained in the linker in order to preserve the integrity of the MOF and thus Cu(I) was used to lock the geometry. Once the MOF was obtained, it could be demetalated using a post-synthetic acid treatment. Following demetallation, the material could be metalated with the precursor of choice, in this case $[Cu^I(CH_3CN)_4]PF_6$, a known olefin cyclopropanation catalyst.[169]

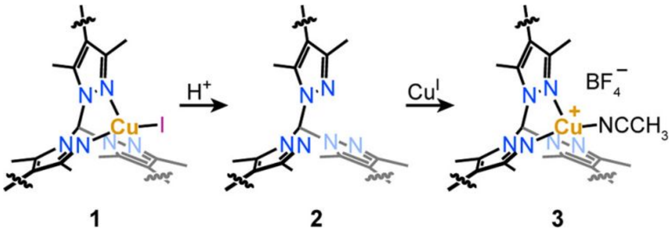

Figure 20. Formation of scorpionate sites within the MOF using Cu(I) to lock the geometry. This can then be demetallated and remetalated. Adapted with permission from ref. 168. Copyright 2018 American Chemical Society.

2.3 MOF-Pore-Based Presentation and Isolation of Catalysts

2.3.1 Polyoxometalates

Polyoxometalates (POMs) consist of high-valent metal atoms connected with other surrounding metal ions *via* oxygens. POMs can be regarded as isolated metal oxide clusters, for which size, charge, acidity, oxidation-state, and composition can, at least in principle, be easily tuned. Due to their high solubility in polar solvents, it can be challenging to reuse POMs as catalysts. Heterogenization of soluble POMs on various supports can increase their stability and make catalyst recycling feasible. In this subsection, we will discuss how MOFs have been enlisted to support POMs and to provide reactant accessibility.[170-175]

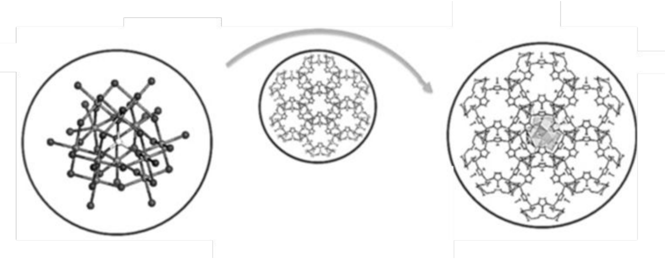

Figure 21. Keggin POM $[CoW_{12}O_{40}]^{6-}$encapsulation in ZIF-8. Adapted with permission from ref. 177. Copyright 2018 John Wiley and Sons.

Steric encapsulation of POMs relies on size matching between the MOF cavity and POM, where the MOF pore is big enough to accommodate a POM, but the apertures/windows are small enough to prevent the POM from leaving.[176] To this end, Mukhopadhyay, *et al.*[177] prepared a composite by growing ZIF-8 around the pre-formed POM (**Figure 21**). POMs were sited inside ZIF-8 hollow cages (11.6 Å), and could not exit through 3.4 Å windows. The composite appears to be functional as a very high overpotential electrocatalyst for water oxidation to O_2 – by extrapolation, *ca.* 1.5 V of overpotential at a benchmark current density of 10 mA/cm^2. The high kinetic overpotential is not altogether surprising, as the composite is likely difficult to infiltrate with electrolyte, thereby restricting catalytic activity to POMs sited in the outermost pores of the ZIF crystallites. (ZIF = zeolitic imidazolate framework, and denotes an imidazolate-linker-containing MOF that features a known zeolite topology.[178] These have sometimes been termed Z-MOFs[179] or MAFs[180]. Further, the putative active-site is a cobalt ion residing at the centre of the POM, seemingly leaving it only poorly accessible to reactants (pairs of water molecules). Nevertheless, the composite clearly is persistently electrocatalytic for water oxidation to O_2 over the pH range 2 to 7.

Bromberg, *et al.*[181] obtained PTA@MIL-101(Cr) (**Figure 22**) by heating phosphotungstic acid (PTA, $H_3PW_{12}O_{40}$) in an aqueous dispersion of MIL-101(Cr) (interconnected cages featuring Cr_3 nodes with BDC^{2-} linkers). Wee, *et al.*[182] subsequently showed that PTA@MIL-101(Cr) could also be obtained by including PTA in the synthesis milieu for the MOF. PTA is reasonably size-matched to the 12 and 14 Å apertures of MIL-101 and is observed to occupy both 29 and 34 Å diameter pores. Thus, there is adequate room for subsequent incorporation of a size-dispersed range of candidate reactants for catalytic chemical transformations. PTA is well retained by the MOF, even under catalytic conditions, and Cr-MIL-101 is unusually resistant to chemical degradation.

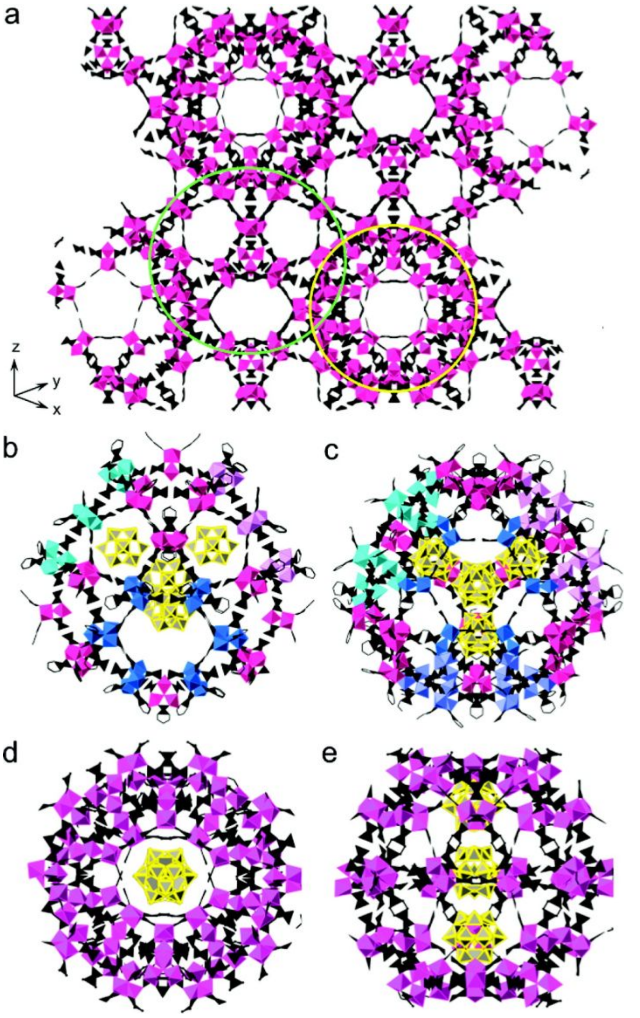

Figure 22. Crystal structure of (a) MIL-101 and proposed structures of (b–e) MIL101/PTA composites. (a) MIL-101 crystal structure with the boundary of the large cage highlighted green and that of the small cage highlighted yellow. The Cr polyhedrons are colored pink. (b, c) The PTA tetrahedron in a multi-coloured large cage of MIL-101, which corresponds to the model with ordered PTA. Views from two directions are presented, b is viewed from the same direction as in a, and c is viewed facing a six-carbon ring. Each of the four six-carbon rings is coloured differently, each aligned with a PTA molecule. (d, e) A possible configuration of three PTA molecules in a small cage of MIL101 viewed (d) from the front, which is the same direction as in a, and (e) from the top. Adapted with permission from ref. 181. Copyright 2012 American Chemical Society.

DED analysis can yield a coarse map of electron density attributed to the incorporation of guest species. By using this method, the general siting of POMs in MOF can be determined. Buru, *et al.*[173] incorporated PTA into NU-1000 *via* an aqueous impregnation method, and DED analysis revealed that the POMs were exclusively located inside the MOF's small triangular channels. Interestingly, further study showed that the location of the POM in NU-1000 depends on the activation conditions (*i.e.*, removal of synthesis solvent). The POM resided in the mesopores when supercritical CO_2 was used to evacuate the pores, whereas it migrated to the micropores when heated to 120 °C under dynamic vacuum (**Figure 23**).[170, 172] Siting in the hexagonal mesopore can be considered a kinetically determined location, while the trigonal micropore is the thermodynamically favoured location. Interconnecting the meso- and micro-pores are smaller pores that can distort sufficiently to permit the observed POM migration.

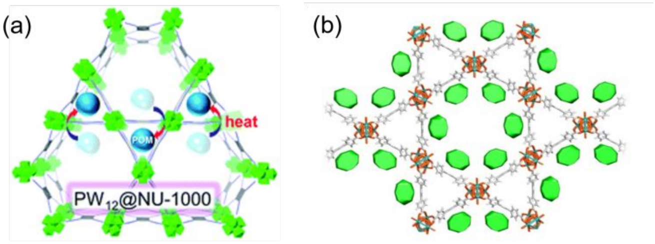

Figure 23. (a) POM migration from mesopores to micropores when heating to 120 °C under dynamic vacuum; (b) DED analysis of PW_{12}@NU-1000 after supercritical CO_2 treatment showing siting of POMs in the hexagonal mesopores. Color code: Teal=Zr, red=O, light gray=C, white=H. Adapted with permission from ref. 172. Copyright 2018 Royal Society of Chemistry.

2.3.2 Molecular Catalysts

In this subsection, we will discuss the most four common approaches to noncovalent encapsulation and presentation of molecular catalysts or co-catalysts by MOF pores: a) ion-exchange of a charged catalyst into a framework of fixed complementary charge, b) transient removal of a linker, typically with restoration after molecular-guest incorporation, c) ship-in-a-bottle construction of a pore-filling metal complex or other guest from components that enter the pore *via* apertures that are narrower than the pore itself, and d) simple size-matching of host and guest, together with London dispersion, hydrogen-bonding, pi-pi stacking, or other van der Waals interactions.[183-188] Note that the first and second approaches at least nominally require the presence of solvent, although the amount can be almost vanishingly small if incorporation relies upon mechanochemistry.[189-191]

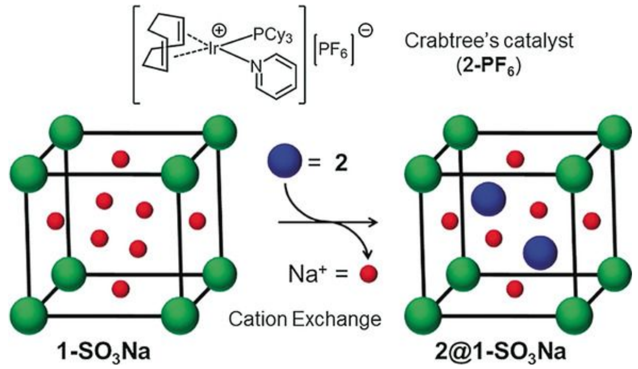

Figure 24. Anionic MOF architecture in which cationic Na^+ ions are exchanged with a cationic analogue of Crabtree's catalyst in order to encapsulate it in the cavity. Of note, MIL-101(Cr) does not exhibit a cubic topology but is depicted as cubic for visual clarity. Adapted with permission from ref. 183. Copyright 2018 John Wiley and Sons.

An example of case (a) is Weller, Rosseinsky, and co-workers' conversion of the well-known MOF, MIL-101(Cr) to anionic form (as a sodium salt) by appending sulfonate groups to BDC^{2-} linkers, followed by partial exchange (~7%) of $Ir(COD)(PCy_3)(py)^+$ ("Crabtree's catalyst"; COD = 1,5-cyclooctadiene; PCy_3 = tri-cyclohexyl-phosphine)[192] for Na^+ (**Figure 24**).[183] The hypothetical maximum catalyst loading, based on steric constraints, is estimated to correspond to exchange of just 9% of the sulfonate-paired sodium cations. While iridium-complex incorporation is nominally noncovalent, *i.e.* solely electrostatic, the authors found evidence for a weak bonding interaction between the iridium catalyst and a linker-pendant sulfonate. Related work featuring catalytic cationic rhodium complexes has been described by Genna and co-workers.[193-194]

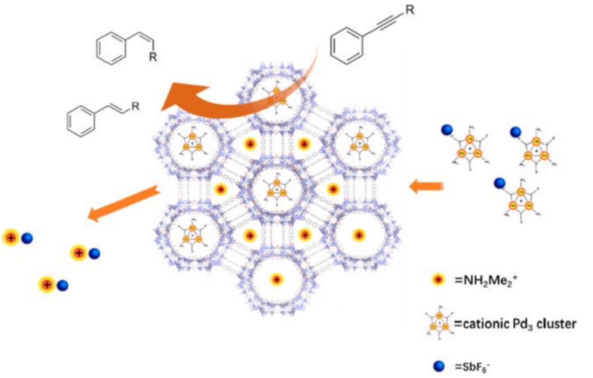

Figure 25. Illustrative scheme of the encapsulation of palladium cluster within bio-MOF 100 for heterogeneous chemo-selective semireduction of internal alkynes. Adapted with permission from ref. 187. Copyright 2019 American Chemical Society.

Peters and co-workers[98] showed that crystal violet, a cationic organic dye, could by ion-exchanged into the channels of NU-1000 and then used to photochemically sensitize the catalytic reduction of water to molecular hydrogen by node-supported nickel-sulfide clusters. Because Zr(IV)-bound aqua, hydroxo, and oxo ligands are weak Brønsted acids and/or bases,[195-196] both the magnitude and sign of the framework charge can vary with pH, thereby modulating ion-exchange behaviour. Pang, *et al.*[185] showed that ion-exchange-based uptake of Ru(2,2'-bipyridine)$_3^{2+}$, a potential photocatalyst, could be engendered by post-synthetically installing within related mesoporous Zr-MOFs, auxiliary linkers featuring anionic (sulfonate) substituents. Ren and co-workers[187] showed that a cationic and catalytic tri-nuclear palladium complex can be incorporated in bio-MOF-100,[197] a mesoporous anionic framework that relies upon strong adeninate-Zn(II) coordination to attain stability (**Figure 25**).

An example of case (b) is illustrated in **Figure 26**; Li and co-workers took advantage of the known substitutional lability (toward oxygen donors, including solvents) of ditopic, carboxylate based linkers in UiO-66 to open a large enough window to encapsulate an organometallic catalyst, (^{tBu}PNP)Ru(CO)HCl (^{tBu}PNP = 2,6-bis((di-*tert*-butyl-phosphino)methyl)pyridine), within octahedral pores of the framework (**Figure 26**). Replacing a hydroxylic solvent with a nonhydroxylic one, shuts off linker lability and locks the molecular guest within the porous MOF.[198-199]

An example of case (c) is illustrated in **Figure 27** by Pardo, Ferrando-Soria, and co-workers.[186, 200] A complex set of MOFs featuring ~2 nm wide, square, 1D channels was prepared. Discrete supramolecular squares featuring either 8 or 16 Pd(II) atoms at vertices were then allowed to self-assemble, either in solution or in templated form, in MOF channels. Importantly, siting the squares within square-channelled MOFs substantially enhanced their stability, especially as active catalysts. The templated siting also allowed for dissociation of some of the square's metal-ligand bonds, but without corresponding fragmentation and loss of the square.

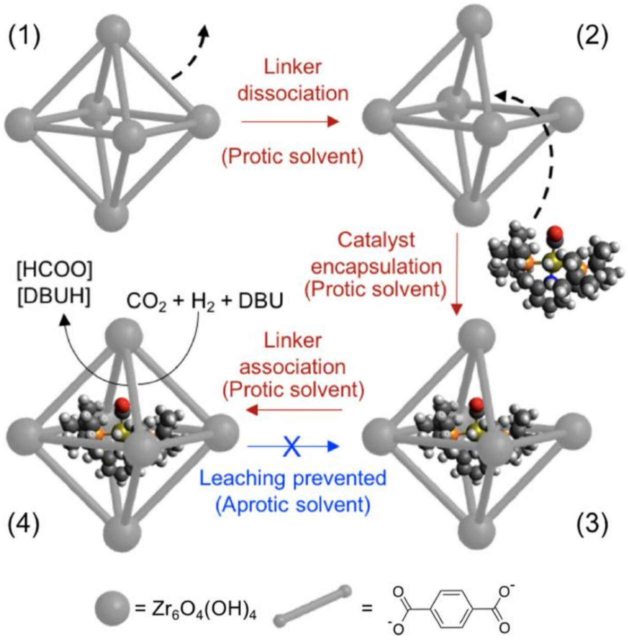

Figure 26. Scheme representing aperture opening method for molecular catalyst encapsulation within MOF UiO-66. Adapted with permission from ref. 198. Copyright 2018 American Chemical Society.

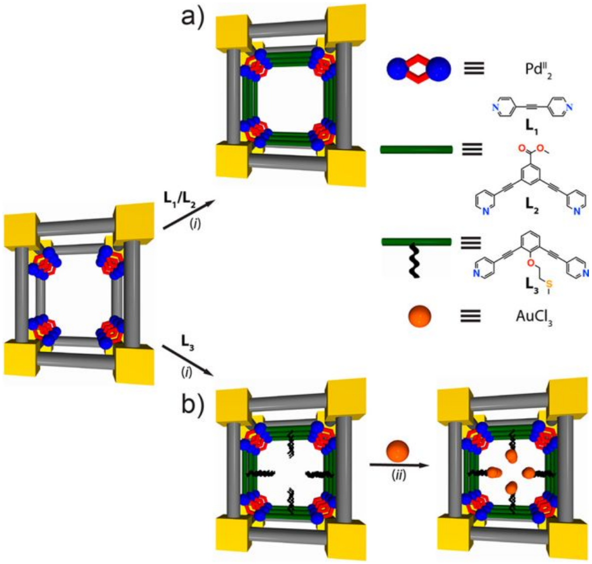

Figure 27. Template-directed strategy, involving the use of post-synthetic methodologies for the stepwise sequential synthesis of original homo- (a) and heterobimetallic (b) mechanically bonded, catalytically active SCCs within the confined space of MOF channels (SCCs@MOFs). (i) Incorporation of desired organic ligand with suitable encoded structural and coordination information and (ii) post-assembly metalation of pre-formed SCCs@MOFs. Adapted with permission from ref. 186. Copyright 2019 American Chemical Society.

NH_2-MIL-125(Ti) is a visible-region photo-active MOF that, in principle, can be coupled to molecular catalysts to accomplish light-to-chemical energy conversion. In practice, the coupling idea is challenging to implement because apertures, as well as pores, are comparatively small (widths of 6 and 12 Å, respectively). For example, cobaloximes are modest-sized catalysts for hydrogen evolution that, nonetheless, cannot pass through NH_2-MIL-125's apertures. Nasalevich and co-workers[201] showed, however, that a catalytic cobaloxime complex could be incorporated by first infiltrating the MOF pores with a flexible free-ligand and then providing cobalt ions for the ligand to wrap in pseudo-macrocycle fashion. This "ship in a bottle" assembly strategy – case (c) strategy – yields site-isolated, permanently pore-confined, but fully functional molecular catalysts, positioned immediately proximal to two photo-active octa-titanium/oxy structures and only slightly displaced from four others; see **Figure 28**.

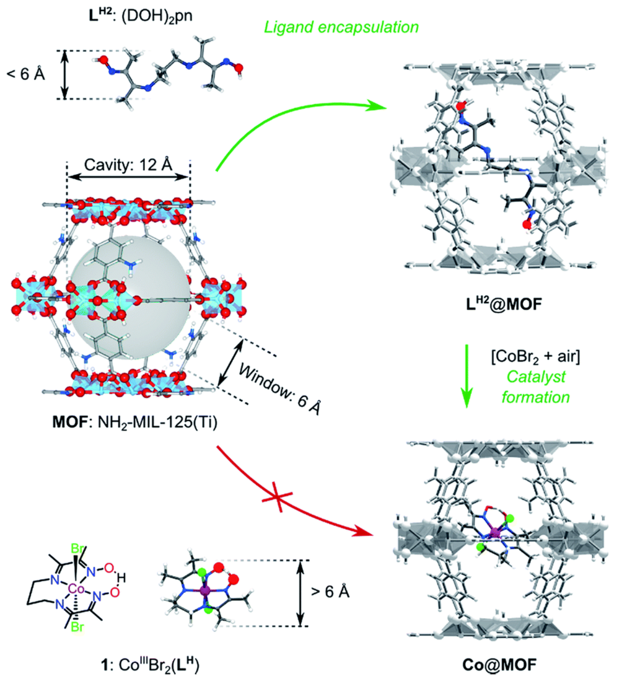

Figure 28. 'Ship-in-a-bottle' synthetic strategy for assembling of cobaloxime complex in NH_2-MIL-125(Ti). Adapted with permission from ref. 201. Copyright 2015 Royal Society of Chemistry.

An example of case (d) is illustrated in **Figure 29**.[202] MIL-101-NH_2(Al) is characterized by interconnected cages having internal diameters of ~29 and ~34 Å and aperture widths of ~12 and ~16 Å. Molecular catalysts for CO_2 reduction (derivatives of cp*Rh(2,2'-bipyridine)$^{1+}$; cp* is pentamethylcyclopentadiene) and molecular light-absorbers/ photosensitizers (derivatives of Ru(2,2'-bipyridine)$_3^{2+}$) are capable of passing through the 16 Å and selectively entering the larger cage. As many as three molecules can occupy a 34 Å cage and, indeed, a combination of two photosensitizers and one catalyst per cage appears to be optimal in terms of catalytic efficiency. Presumably, the cage-enforced proximity of these species maximizes the opportunity to transfer reducing equivalents (electrons) from the photo-excited sensitizers to the reduction catalyst. Finally, here are a couple of design features of note. MIL-101 and its derivatives are typically synthesized with chromium or iron ions, rather than Al(III). In principle, both Cr(III) and Fe(IIII) are capable of functioning as redox quenchers for highly energetic photo-excited states of molecular chromophores. To the extent that quenching occurs, energy that instead could have been used for desirable charge transfer from the excited chromophore to the rhodium catalyst is lost. Al(III), in contrast, is both colourless and redox-inert, and therefore incapable of engaging in unwanted quenching of photo-excited species by energy transfer or charge transfer.

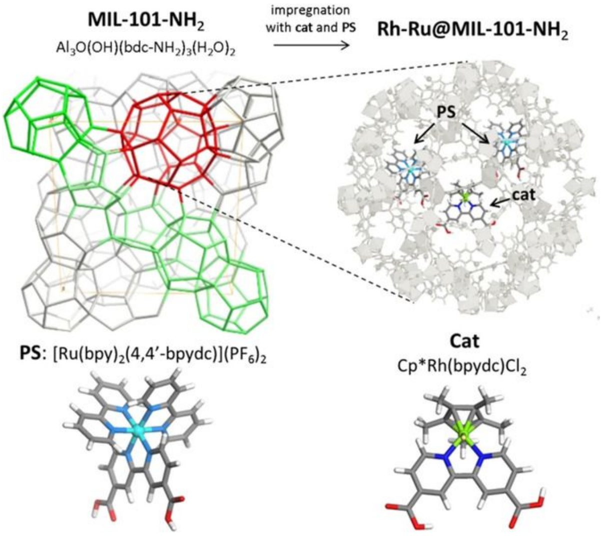

Figure 29. Schematic representation of co-immobilized photosystem in MIL-101-NH_2(Al). The host topology has small (green) and large (red) cages. Shown at the bottom are enlarged structures of photosensitizer (PS) $[Ru(bpy)_2(4,4'\text{-}bpydc)](PF_6)_2$, and catalyst (Cat) $[Cp^*Rh(4,4'\text{-}bpydc)Cl_2]$ (O: red; N: blue; Ru: cyan; Rh: green; C: gray; H: white). Adapted with permission from ref. 202. Copyright 2018 John Wiley and Sons.

2.3.3 Enzymes

The stabilization of catalytic species inside the cavities of a MOF culminates in the immobilization of enzymes through encapsulation.[203] Relatively few other periodically structured porous hosts or supports can accommodate the intermediate size range that is characteristic of enzymes – typically 3-7 nm;[204] SBA-15 and MCM-41 type silicates and aluminosilicates are non-MOF examples.[205-206] The 3 to 7 nm size is greater than what is needed for materials optimized to handle conventional molecules, but smaller than what is needed for materials geared toward interference-based optical sensing applications. Thus far, the broadest benefit of size-matched MOF encapsulation of enzymes has proven to be physical inhibition of denaturation, even when the driving force for denaturation is thermal, chemical (*e.g.*, urea-triggered unfolding), or dehydration.[207] The practical consequences are that storage times can be extended, turnover numbers can be boosted, and harsher external-solution environments can be tolerated. By fully enshrouding an enzyme with polarizable organic linkers, cumulative van der Waals forces, including London dispersion forces, serve in many cases to prevent leeching of enzymes. Nevertheless, the interactions are not so strong that they facilitate enzyme inactivation or prevent enzyme diffusion. The latter is important for boosting enzyme loading. At the same time, the periodic nature of appropriately size-matched MOF pores can prevent enzyme agglomeration and eliminate the need for stabilizing solution-phase surfactants. The comparatively soft nature of most MOFs, together with locally imparted freedom of motion based on secondary apertures and/or linker or substituent torsional motion, appears to permit adjustment of enzyme conformations, so as to favour catalytic activity.

In an early example of enzyme immobilization, Ma, *et al.*[208] loaded microperoxidase-11 (MP-11) (**Figure 30a**) into the mesopores of a terbium-based framework, TbmesoMOF, $Tb(BTC)(H_2O)1.5\cdot(DMF)$ (**Figure 30b and c**) and subsequently showed that the enzyme@MOF composite compared favourably with an enzyme@silica composite in terms of reaction rate, conversion, and recyclability. They attributed the enzyme@MOF behaviour, in part, to high stability for the composite; the heme group of the enzyme orient itself towards the conjugated benzene rings of the framework linkers, presumably to boost π···π interactions,[209] contributing to stabilizing the enzyme and preventing it from exiting or denaturing. Consequently, much attention has been given to increasing favourable enzyme/MOF interactions[210] and sensitizing enzyme responses to external stimuli, with the one goal being controlled delivery of potentially medically efficacious payloads, either enzymes or polypeptide-based hormones (*e.g.*, insulin), within the human body.[211-214] While protein engineering may allow for direct enhancement of an enzyme's catalytic activity, the nature of the support in which the enzyme is confined strongly influences reactivity. Returning to the microperoxidase MP-11 study, the choice of TbmesoMOF underscores two important aspects of MOF chemistry that have been routinely experimentally realizable only over the past several years – the first being hydrolytic stability and the second being synthetic access to mechanically robust MOFs that offer both large pores and large apertures (*i.e.*, large on an abiotic molecule scale).

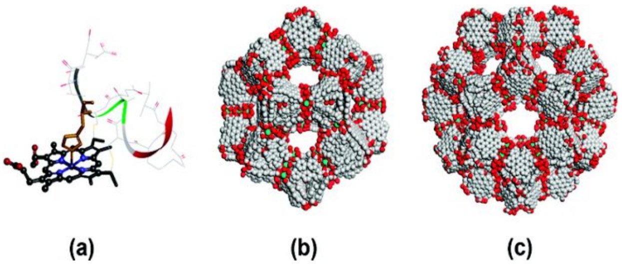

Figure 30. (a) Structure of MP-11, (b) and (c) views of the cage structure of TbmesoMOF. Adapted with permission from ref. 208. Copyright 2011 American Chemical Society.

Zr-MOFs are also often suitable for enzyme immobilization, in part due to their typically hierarchical pore structures, which allow for the simultaneous transport of substrates, and encapsulation of enzymes.[215-218] Provided that unwanted polymorphs can be avoided, isoreticular synthesis of Zr-MOFs is notably facile, although access to elongated organic linkers can be synthetically taxing. The isoreticular approach permits pore-size matching to specific enzymes; see **Figure 31**. Demonstrated applications include carbon dioxide reduction[218] and chemical warfare agent degradation.[219] For both applications, hierarchical porosity is desirable, such that enzymes are constrained to mesopores, leaving micropores available for molecular transport and interconnecting orthogonal pores available for molecular access to enzymes.[218-219]

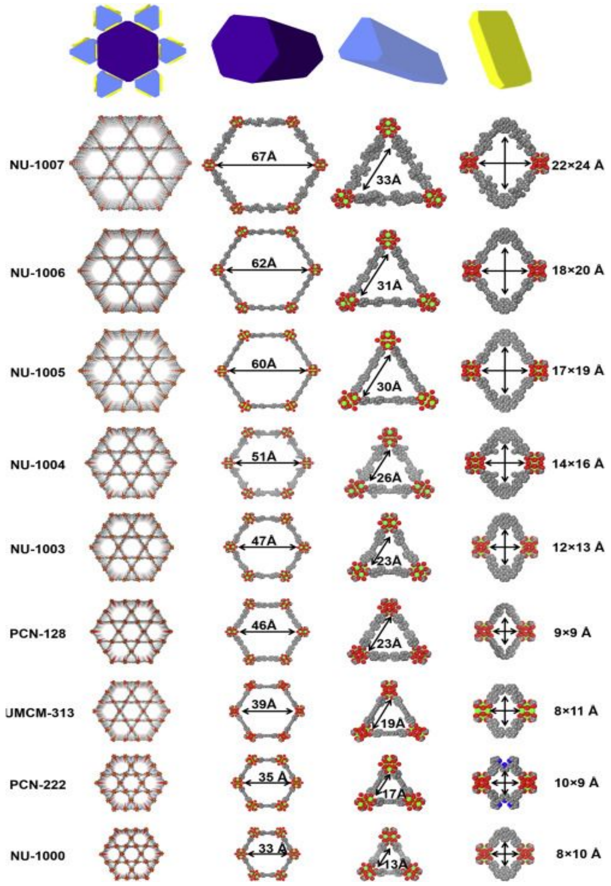

Figure 31. Diagram illustrating the isoreticular **csq** zirconium MOFs showing packing diagram, hexagonal pores, triangular pores, and windows between hexagonal and triangular pores. Adapted with permission from ref. 216. Copyright 2018 Elsevier.

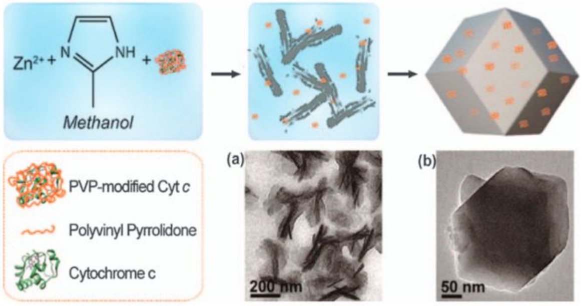

Figure 32. Schematic illustrating the synthetic process by which cyt-*c* is encapsulated within ZIF with use of polyvinyl pyrrolidone to facilitate growth. Adapted with permission from ref. 220. Copyright 2014 American Chemical Society.

As an alternative to encapsulation, Liu *et al.*[220] demonstrated that one may efficiently grow a ZIF-8 support around the enzyme cytochrome-*c* (Cyt-*c*) in a one-pot synthesis (**Figure 32**). Perhaps surprisingly, given their small apertures, ZIFs are a well-studied support for enzymes.[210, 214, 221-224] The benefits of the tightly-fitting ZIF are two-fold: the proximity of the enzyme to its container facilitates interactions that prevent enzyme leaching, and at high enough loadings, where mixtures of enzymes yield hetero-clusters, ZIF-encapsulation locks-in short separation distances between enzymes of differing identity – for example, sets of enzymes that can carry out successive stages of cascade reactions.[224-225] As noted by Ge, *et al.*,[225] close proximity of cascade actors can enable chemical intermediates to reach their destination and react before decaying.

For diffusive transport, the required time increases as the square of the distance travelled. As a simplified example, in the absence of adsorption to the framework, a small, solution-phase substrate could travel 1 nm in perhaps 1 ns, but would need 1 microsecond to move 30 nm. Consequently, minimizing the distance between enzymes, via clustering, followed by encapsulation, reduces the amount of time reactive intermediates must persist.

2.3.4 Encapsulated and Enshrouded Metal Nanoparticles

In early studies of MOF-based catalysis, including our own,[140] contrived reactant size disparities were occasionally introduced in order to gauge whether catalysis was occurring only on the catalytic MOF exterior, or also within. Of much more interest here is the notion that a uniformly porous MOF, encapsulating or enshrouding a catalyst, can function as a gatekeeper for reactant access to the catalyst. In this subsection, we will focus on approaches for preparing MOF confined NPs.

Here and elsewhere, we reserve “encapsulate” for guest siting in a single pore and “enshroud” for guest siting that requires more than a single pore. MOF apertures place limits on the combination of reactant size and shape that can permeate the framework. Navigable sizes of apertures, channels, and pores are defined by MOF topology, linker size and shape, and node dimensions. For MOFs that can catenate,[226] they are further defined by degree of catenation. Void sizes can be altered by selective pore-filling, post-synthetic modification, or even photo-driven isomerization of tethered guest molecules.[227] Notably, for highly defective versions of UiO-type MOFs,[88] effective aperture and pore sizes can be larger than those of defect-free or low-defect-density versions.[228] Aperture sizes can nominally be assessed from structures derived from single-crystal X-ray diffraction (SCXRD) data. For many MIL-type MOFs, however, frameworks are flexible enough to admit guest molecules that are too large to permeate the MOF if it were inflexible.[229-232] Similarly, aperture-defining ditopic linkers in ZIF-8 and related materials are akin to gates or hinges and can collectively swing to admit molecular permeants that substantially exceed static, crystallographically defined pore-widths.[233-234] Nevertheless, MOFs offering apertures of this kind typically still display sharp permeant size cut-offs.[8]

Enshrouding/encapsulating catalytic metal nanoparticles within MOFs provides a means of displaying particles to both solution- and gas-phase molecules, typically with a pre-determined maximum molecule size and sometimes with a predetermined orientation with respect to the embedded catalyst. The MOF may also serve to select and preconcentrate potential reactants – for example, CO_2 or water from the vapor phase, or small organic molecules from a condensed aqueous phase. Depending on the reaction milieu, frameworks can be effective for preventing particle sintering, agglomeration and/or precipitation. Arguably underappreciated is that nanoparticles can often be MOF-embedded such that their surfaces are free, or largely free, of capping ligands. In contrast, in the absence of an enshrouding MOF, capping ligands may be necessary to arrest particle growth, prevent particle agglomeration, or otherwise stabilize the particle, yet their presence may complicate the use of nanoparticles as catalysts.

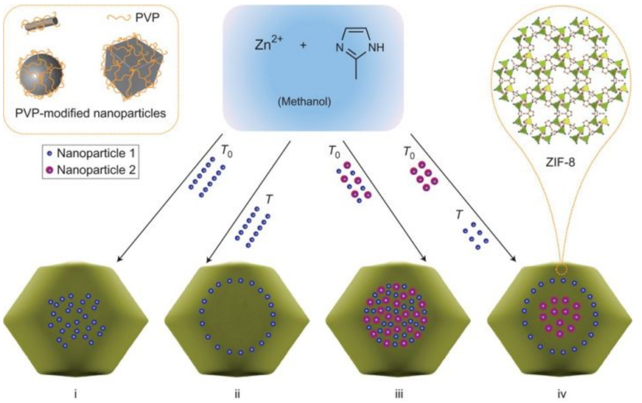

Figure 31. Scheme of the controlled encapsulation of metal NPs inside ZIF-8 crystals. Adapted with permission from ref. 235. Copyright 2012 Springer Nature.

Two broad approaches to NP@MOF formation exist, each with advantages and disadvantages. Frameworks can be assembled around pre-existing particles, or particles can be grown within pre-existing MOFs. Representative of the first approach is a scheme devised by Lu, *et al.* and illustrated in **Figure 33**.[235] Notably, the scheme starts with the stabilization of suspensions of NPs with polyvinylpyrrolidone (PVP). This step makes nanoparticles as different as silver metal, CdTe quantum dots, and ferrous-ferric oxide (magnetite), amenable to encapsulation *via* the same set of experimental conditions (for a given MOF). Additionally, at least for the MOFs examined, the MOF growth process itself removes all but trace amounts of PVP, as evidenced by ^1H NMR spectra of digested samples. With regard to limitations, the most obvious is that ultrasmall metal NPs are difficult to enshroud. A second is that size dispersity for the enshrouded particles is only as narrow as the dispersity of the starting colloidal suspension. Both issues are pertinent to the potential dependence of NP functional behaviour, including catalytic behaviour, on particle size.

Jiang, *et al.*[236] used a microwave method to generate MOF and NP species simultaneously. From the synthesis they recovered a composite consisting of ultrafine Au NPs encapsulated within MOF-199 (also known as HKUST-1: $[Cu_3(TMA)_2(H_2O)_3]_n$, TMA^{3-} is the fully deprotonated conjugate base of 1,3,5-trimesic acid, see **Figure 7**) that exhibited a TOF of ~ 700 h^{-1} for the one pot reaction of three component coupling of paraformaldehyde, phenylacetylene, and piperidine. Zeng, *et al.*[237] developed another core-shell MOF nanoreactor that contains Co_3O_4 NPs within a MOF-5 shell($Zn_4O(BDC)_3$, BDC^{2-} = 1,4-benzene dicarboxylate, **pcu** topology, see **Figure 7**) that efficiently degraded 4-chlorophenol, reaching higher conversion than bare Co_3O_4 NPs (100% conversion at 60 min. for the composite vs. 60% for bare NPs).

A second approach is to infiltrate a preformed MOF with metal cations and then chemically reduce the ions – typically, with H_2 or a solution of sodium borohydride – to zero-valent atoms. The uncharged metal atoms typically have limited chemical affinity for framework components; thus, they are mobile until they find other metal atoms with which to combine to form zero-valent clusters and NPs. In most cases, particles grow until the supply of metal atoms is depleted – ignoring in their growth the existence of MOF nodes, pore walls, etc. This behaviour is an understandable consequence of the typically, but not universally, stronger bonding within NPs relative to coordination-type linker-node bonding. Given that bonding in metals is delocalized, defining a bond strength for comparison to localized linker-node bonds is a bit complicated. Nevertheless, a rough idea of "bond strength" within a metal particle can be obtained by looking at known molar heats of sublimation of bulk metals.

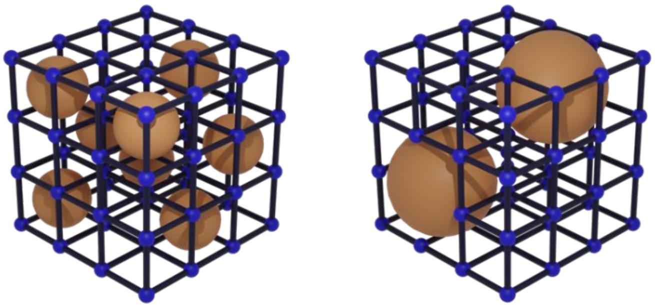

Figure 32. (left) NP siting within single cavities of a MOF (pore-confined/encapsulated); and (right) NP siting within MOF crystallite (MOF enshrouded).

The alternative to unconstrained growth is pore-templated (pore-confined) growth. **Figure 34** illustrates the difference between pore-confined and simply MOF-encapsulated nanoparticles. The former, while still randomly spatially distributed, are characterized by uniform size and uniform siting (for example, linker-contact siting versus node-contact siting). Uniformity is desirable if the goals are to understand and control catalytic behaviour. The following factors favour formation of pore-confined metal nanoparticles. First, strong and substitution-inert linker-node bonding favours confinement – as in MIL-101(Cr),[238-239] with its Cr(III)/anionic-oxygen-atom bonding. It's worth noting that bonds between Zr(IV) and negatively charged, linker-terminating oxygen atoms are likely stronger, but are much more susceptible to disruption *via* ligand substitution – so are less effective at constraining NP growth. Within the realm of Zr-MOFs, factors that can tame NP growth and favour formation of pore-templated particles are: i) polytopic linkers (as found in MOF-808 (structure see **Figure 12**),[34] DUT-49 (DUT = Dresden University of Technology) (structure see **Figure 7**),[240] and PCN-222/MOF-545/MMPF-6) (structure see **Figure 7**)[241-243] in place of ditopic linkers (as in UiO-type MOFs), ii) pre-binding of metal ions (for example, *via* node coordination sometimes termed cation-exchange, by analogy to zeolites) or by linker coordination (for example, by linker-embedded catecholates or dipyridyl sites), iii) limited loading (by one of the preceding methods) as opposed to maximal loading by pore-infiltration with metal salts, and iv) ligand retention by the liberated zero-valent metal atom. An example of case (iv) is organophosphine ligand retention by liberated and mobile Au(0) atoms.[244] Au NP formation under these conditions requires elimination of Au-P bonds from all but the outermost gold atoms. Thus, the energy gained by consolidating individual Au(0) atoms into Au nanoparticles is less than otherwise expected.

If detectable, direct observation by high-resolution transmission-electron-microscopy (HRTEM), constitutes compelling evidence that nanoparticles have formed.[245-246] Because metal NP distributions within MOFs tend to be random, and the fractions of pores occupied tend to be low, SCXRD is consequently not very instructive, nor are changes in adsorption-isotherm-derived pore-size distributions. PXRD, however, can reveal the presence and probable identity of crystalline metal NPs, based on high-angle diffraction. Also useful are: i) EXAFS data from which average coordination numbers and therefore, particle sizes can be inferred, ii) pair-distribution function(PDF) analysis of total X-ray scattering, from which the number of shells of atoms comprising the average particle can be inferred, and iii) DED maps from X-ray diffraction measurements, from which particle size, approximate shape, and general siting can be determined.

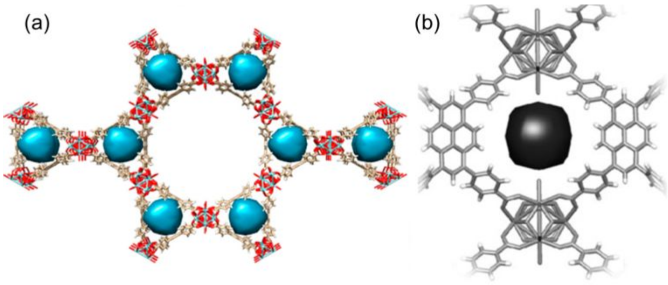

Figure 33. DED maps for (a) AuNP-NU-1000 viewed parallel to the *c*-axis; and (b) PtNP-NU-1000 viewed perpendicular to the *c*-axis. The blue and black shapes are experimental electron density data corresponding to AuNP and PtNP, respectively. Note that the DED data are diffraction-derived, so are averaged over many pores and channels, both occupied and empty. Thus, not every chemically suitable pore is occupied by a metal NP. Adapted with permission from refs. 244 and 103. Copyright 2019 American Chemical Society and 2018 John Wiley and Sons.

NU-1000 offers numerous illustrations of NP encapsulation. H_2 reduction of node-grafted Cu(II) yielded mainly mesopore-sited NPs of ~3.5 nm diameter and containing ~2,900 copper atoms, encapsulated by six organic linkers.[247] Similar NPs prepared in NU-901 are catalytic for selective partial hydrogenation of acetylene to ethylene.[248] Reduction of ligand-immobilized Au(I) yields mainly micropore-sited NPs of ~1.5 nm diameter and containing ~90 gold atoms, encapsulated by three organic linkers (**Figure 35a**).[244] Nevertheless, for both copper and gold, the size distribution is observably bimodal, at ~3.5 and ~1.5 nm, consistent with templating by both mesopores and micropores. Reduction of node-grafted Pt(IV) yields mainly NPs of ~0.8 nm diameter containing ~30 platinum atoms, with roughly 90% present in zero-valent form and 10% as Pt(IV). The Pt NPs reside in *c*-pores that interconnect meso- and micropores (**Figure 35b**).[103] Bound by a pair of oxy-Zr_6 nodes, the NPs appear to be node-grafted *via* Pt(IV)-O-Zr(IV) links. For these encapsulated (*i.e.*, single-pore-occupying) NPs, the key chemical distinction in terms of node-siting versus linker-siting appears to be the presence (or absence) of cluster ions that can accommodate oxo- or hydroxo-bridges to nodes. For enshrouded (*i.e.*, multi-pore-occupying) NPs, the most important factor may be simple geometric access to nodes whose linker connections have been partially displaced by nanoparticles themselves.

Returning to copper, Redfern and co-workers showed that NPs of a single size could be obtained by replacing NU-1000 and its **csq** topology with NU-901 or NU-907, MOFs having **scu** topology and featuring only one size and type of extended channel (1D diamond channels).[248] Reduction of node-grafted Cu(II) ions yields roughly spherical zero-valent copper NPs of uniform diameter – either ~1.5 nm based on NU-901 templating or ~0.9 based on NU-907 templating (**Figure 36**).

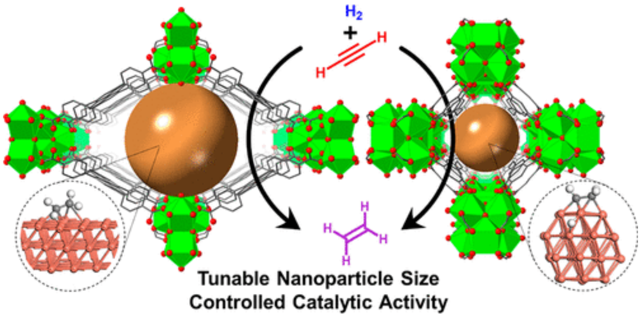

Figure 34. NU-901 and NU-907 serve as templates to control the growth of Cu nanoparticles for forming uniform particle sizes (~1.5 nm and ~0.9 nm, respectively) for catalytic semihydrogenation. Adapted with permission from refs. 248. Copyright 2020 American Chemical Society.

Yang, *et al.*[249] have described the unexpected formation of zero-valent copper nanoparticles within NU-1000, starting from node-grafted and -isolated cupric ions. Metal-ion reduction and metal(0)-NP formation occur under inert atmosphere when samples are heated to ~ 90°C, *i.e.* a temperature typical for MOF "activation" – meaning thermal removal of physisorbed or very weakly chemisorbed synthesis-solvent and/or lab-atmosphere-derived water. The overlooked metal-ion reductant turned out to be node-ligated formate that is adventitiously introduced is a decomposition product of water-containing dimethylformamide, a standard synthesis solvent.[250] Formate is a thermodynamically potent two-electron donor, whose activity, at ambient temperature, is largely suppressed by Zr-node-ligation. Its ^{1}H NMR and diffuse reflectance infrared Fourier transform spectroscopy (DRIFTS) signatures are both simple and small – and, therefore, easy to miss. In Yang's study, a quantitative correspondence was found between the number of formate ions oxidatively degraded and the number of Cu^{2+} ions reduced to Cu(0). Although we are unaware of other reports, it is likely that remnant synthesis modulators such as acetate and benzoate can similarly function as two-electron reductants when heated, and that other easily reducible metal ions/complexes such as Au(III), Pd(II), and Pt(II) can, when attached to MOF nodes, similarly be converted to zero-valent metal atoms and then NPs *via* thermally assisted oxidation of remnant modulators or nonstructural ligands.

Qiu, *et al.*[251] have described an innovative approach to MOF-pore-limited formation of metal NPs, based on encapsulated metal–organic polyhedrons (MOPs) as precursors. Briefly, the sizeable sphere-like pores of an unusually stable MOF, MIL-101(Cr), were infiltrated with molecular polyhedra featuring Pd(II) vertices (**Figure 37**). Temperature-controlled heating under a reducing atmosphere selectively pyrolyzes the MOP, leaving within the intact pores of MIL-101(Cr), dehydrogenated & oligomerized C_xN_y fragments and zero-valent Pd clusters of average size ~0.8 nm. Ying, *et al.*[104] have reported on a conceptually related idea involving pore infiltration by metal-cation-binding dendrimers, and subsequent heating in a reducing atmosphere to form small node-supported copper, palladium, and platinum. While the obtained clusters are not of uniform size, the approaches constitute progress toward forming and stabilizing small, zero-valent, metal clusters of well-defined and uniform size and shape in catalytically functional form within MOFs. This problem has turned out to be considerably more difficult to solve than obtaining and stabilizing uniformly sized MOF-supported metal-oxy and metal-sulfido clusters of uniform size. The difficulty clearly stems from the difficulty in enforcing strong size-stabilizing interactions between MOFs and metallic clusters versus MOFs and metal-ion-containing clusters. Under-explored for MOFs is the notion of intentionally creating persistent oxygen vacancies on redox-active nodes and exploiting the vacancies to covalently anchor zero-valent metal atoms.

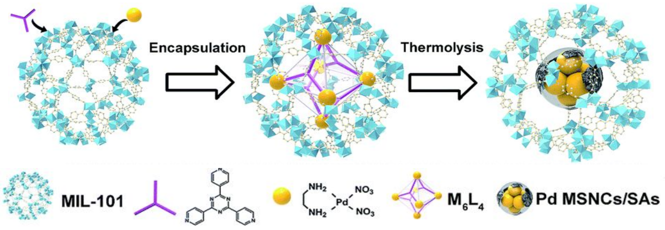

Figure 35. Synthetic scheme for the creation of Pd/C-N⊂MIL-101 through the use of a metal–organic polyhedron as the NP precursor. Adapted with permission from ref. 251. Copyright 2018 Royal Society of Chemistry.

Using the stable Zr-based MOF, UiO-66-$(OH)_2$, Luo, *et al.*[252] developed an oxidative linker cleaving technique that allows for the synthesis of single-crystals with core-shell properties. Using either HNO_3 or strongly oxidizing reactive-oxygen-species (ROS), core-shell or multi core-shell structures with embedded Pd NPs could be generated from pre-synthesized MOF crystals (**Figure 38**). This provides the opportunity for installing multiple Pd NPs in individual core-shell environments within the single-crystal MOF for enhanced thermal stability of the nanoparticles. To test their catalytic activity and potential size-selectivity, Pd@UiO-66-$(OH)_2$ materials were etched and prepared, and then exposed alkene substrates and H_2. Cyclohexene can be 97% hydrogenated while a slightly larger candidate substrate, cyclooctene, fully resists hydrogenation, presumably because it cannot physically access the MOF-enshrouded Pd NPs. Additional experiments demonstrated that the enshrouded NPs resist agglomeration, even when heated.

Figure 36. Schematic illustration of the oxidative linker cleaving process used to install Pd NPs in a multiple core-shell fashion. Adapted with permission from ref. 252. Copyright 2019 American Chemical Society.

Cure, *et al.*[253] installed Au NPs in thiol-modified MOFs *via* photoreduction of a Au(III) precursor. The presence of a thiol group in the linker was found to be important in preventing the migration of NPs to the MOF external surface, a theme also seen in a study by

Abedi, *et al.*[254] for the encapsulation of Pd NPs in Zr-MOF DUT-67 ($Zr_6O_6(OH)_2(tdc)_4(CH_3COO)_2$, tdc = thiophene dicarboxylate, see **Figure 7**), and by Su, *et al.*[255] for the generation of NPs within the pores of a related pair Zr-MOFs featuring redox-active tetrathiafulvalene linkers, see **Figure 7**, *i.e.* $[Zr_6(TTFTB)_2O_8(OH_2)_8]$ and $[Zr_6(Me\text{-}TTFTB)_{1.5}O_4(OH)_4(C_6H_5COO)_6]$ where TTFTB is tetrathiafulvalene tetrabenzoate, and Me-TTFTB is tetrathiafulvalene tetramethylbenzoate.

Closely related to reactant discrimination based on size and shape, but somewhat under-explored in the context of MOF-based chemical catalysis, is reactant discrimination based on charge, hydrophobicity, or other properties. ZIF-8, for example, is permeable to CO_2, ethanol (liquid and vapor), O_2, and other small molecules, but is effective in excluding water in both liquid and, to a large extent, vapor form; these differences have been exploited for chemical sensing,[256] so ought to be extendable to chemical catalysis. More complex is behaviour displayed by NU-1000, when node-functionalized with redox-active ferrocene.[257-258] In thin-film form, this material displays electrochemical-potential-dependent permselectivity for solution anions and charge-exclusion (“Donnan exclusion”) of cations.[257]

3. Tuning Catalytic Activity and Selectivity

3.1 Encapsulating and Enshrouding NP Catalysts to Define Reactant Accessibility and Engender Size-, Shape-, and Regio-Selectivity

In this subsection, examples of aperture-based steric control of reactant access to enshrouded catalysts, mainly by using ZIF-8 and related zeolitic imidazolate frameworks,[259-260] or by using MOFs comprising the UiO series.[261] Many examples of both kinds of frameworks are straightforward to synthesize in high yield. Furthermore, they tend to be water stable and reasonably thermally stable. Additionally, ZIF-8, in particular, is easy to synthesize in supported-thin-film form.[262-265]

In an early study, Lu, *et al.*[235] looked at ZIF-8-encapsulated platinum NPs as catalysts for olefin hydrogenation by H_2. Platinum is an indiscriminate hydrogenation catalyst, but Pt@ZIF-8 is both size selective and regioselective. ZIF-8 offers ~ 3.4 Å apertures that can open to about 5.8 Å.[233-234] As illustrated in **Figure 39** (not to scale), these apertures admit 1-hexene, but block *cis*-cyclooctene – behaviour that translates into selective catalytic hydrogenation of the linear compound by the enshrouded platinum NPs. Note that the essentially complete selectivity for the linear reactant implies that catalyst-accessible cracks and pinholes are absent, as even a small number of such defects would permit rapid and indiscriminate transport of olefins to the catalyst.

Returning to **Figure 39**, evaluation of *trans*-2-hexene revealed that this compound also permeates ZIF-8. But, the 2-hexene isomer is immune to subsequent catalytic hydrogenation. Further work showed that only the terminal C=C bond of 1,3-hexadiene is hydrogenated by Pt@ZIF-8.[266] The observed regioselectivity implies close contact between platinum NP surfaces and ZIF apertures. The synthesis and catalytic hydrogenation activity of Pd@ZIF-8 hollow nanospheres have also been reported.[267-269] Rate-limiting diffusion through thin ZIF-8 shells is faster than through solid ZIF-8, resulting in enhanced catalytic activity. Selectivity based on molecular sieving is retained, but regioselectivity is sacrificed.

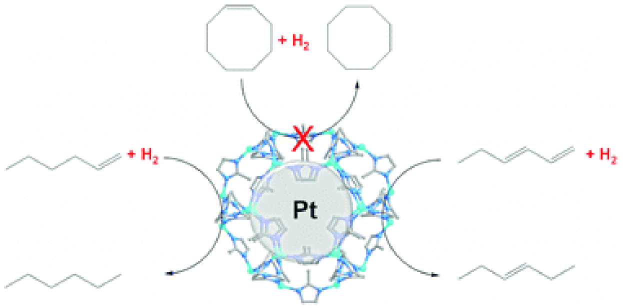

Figure 37. ZIF-8 apertures admit 1-hexene, but block cis-cyclooctene – behaviour that translates into selective catalytic hydrogenation of the linear compound. Adapted with permission from ref. 266. Copyright 2015 Royal Society of Chemistry.

Stephenson, *et al.* showed that SALE (solvent-assisted linker exchange)[270-271] with ZIF-8, replacing ~ 85% of the methyl-imidazolate linkers with methyl-free imidazolate, opened apertures enough to allow permeation of *cis*-cyclooctene and therefore, hydrogenation by enshrouded nanoparticulate Pt.[272] The SALE-treated assembly, however, effectively discriminated against a slightly larger candidate substrate, β-pinene. It is worth noting that ZIF-8 and the modified compound, denoted as SALEM-2 (SALEM: solvent-assisted linker exchanged material), offer essentially identical cavity dimensions; only the width of the small apertures leading into the compounds and connecting cavities within the MOF are altered. Related catalytic size/shape selectivity has been reported for Pt@UiO-66,[273-274] as well as for bimetallic-nanoparticle-containing systems, such as PtCo@UiO-66, PtCu@HKUST-1 (HKUST-1 structure see **Figure 7**) and PdPt@UiO-66.[275-277]

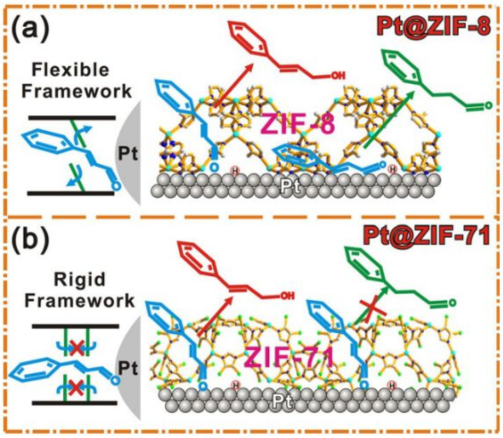

Figure 38. Schematic illustration of CAL adsorption onto the Pt surface inside (a) flexible ZIF-8, and (b) rigid ZIF-71. Adapted with permission from ref. 278. Copyright 2017 John Wiley and Sons.

Regioselectivity can also be modulated by tuning the structural rigidity of frameworks. Chen, *et al.*[278] compared the activity and selectivity for cinnamaldehyde (CAL) hydrogenation to cinnamyl alcohol on Pt nanoparticles enshrouded by ZIF-71 and by ZIF-8 (see **Figure 40**). ZIF-8 features a sodalite structure with 11.6 Å cavities and 3.4 Å pore apertures that can open to ~5.5 Å.[279] ZIF-71 is made from

Zn^{2+} nodes and 4,5-dichloroimidizolate, organized to yield an **rho** topology, see **Figure 7**. It features larger 16.8 Å pores, but more rigid apertures (4.8 Å). The more rigid apertures of ZIF-71 lead to higher regioselectivity, and discrimination against the over-hydrogenated product.

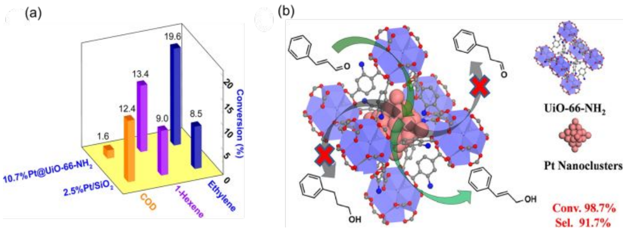

Figure 39. (a) Reactivity of Pt@UiO-66-NH$_2$ and Pt/SiO$_2$ in the hydrogenation of ethylene, 1-hexene, and 1,3-cyclooctadiene; (b) regioselective cinnamaldehyde hydrogenation of Pt@UiO-66-NH$_2$. Adapted with permission from ref. 280. Copyright 2014 American Chemical Society.

Guo, *et al.*[280] synthesized and evaluated Pt@UiO-66-NH$_2$ as a hydrogenation catalyst (The amino substituent serves to favourably slow and delimit nanoparticle growth by binding to single-platinum-ion precursors.). Consistent with a *ca.* 6 Å aperture size, Pt@UiO-66-NH$_2$ is active for ethylene hydrogenation, but blocks 1,3-cyclooctadiene (6.7 × 6.2 × 4.2 Å). As shown in **Figure 41**, the enshrouded catalyst is also regioselective – in this case for hydrogenation of a terminal C=O, with little activity toward an interior C=C. Control experiments, with Pt NPs supported on the exterior of the MOF yielded only marginal regioselectivity.

Zheng, *et al.*[281] examined Pd-NP@UiO-66-NH$_2$ as a reusable catalyst for hydrogenation. With candidate olefin substrates, 1-hexene, styrene, and terphenylethylene, Pd-NP@UiO-66 yields conversions of 100%, 98%, and 0%, respectively, indicating that terphenylethylene is unable to access the enshrouded catalyst. Size selectivity for olefin hydrogenation is similarly observed for PtCo NPs enshrouded by UiO-66; catalytic hydrogenation is quantitative for 1-hexene, but < 1% for terphenylethylene.[282]

3.2 MOF-Based Support and/or Interfacial Effects

3.2.1 Metal NP Catalysts

In this subsection, we will discuss examples of metal-support interactions between MOF SBUs and enshrouded metal NPs, and their impact on catalysis *via* charge transfer, increased interfacial contact, and stabilization of reaction intermediates.

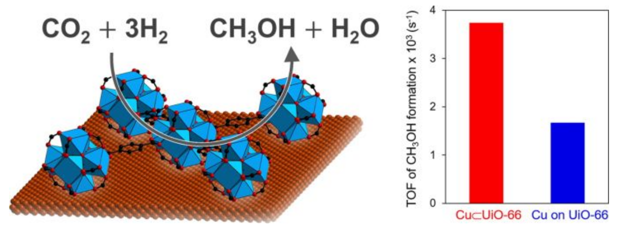

Figure 40. (left) Illustration of CO$_2$ hydrogenation reaction occurring over copper nanocrystals encapsulated in UiO-66; (right) Comparison of TOF of methanol formation between Cu encapsulated in UiO-66 and Cu on UiO-66. Adapted with permission from Ref. 283. Copyright 2016 American Chemical Society.

Rungtaweevoranit, *et al.*[283] reported that by mixing pre-synthesized 18 nm Cu NPs with MOF precursors, Cu NPs were successfully enshrouded within Zr-based UiO-66. This material, denoted as Cu⊂UiO-66, exhibited 100% selectivity for CO$_2$ hydrogenation to methanol, along with higher activity than Cu@MIL-101(Cr), Cu@ZIF-8, Cu/ZrO$_2$, Cu/Al$_2$O$_3$, and the benchmark catalyst Cu/ZnO/Al$_2$O$_3$. Strong electronic interactions between Cu and the Zr SBU were verified by X-ray photoelectron spectroscopy (XPS), where the binding energy of Zr shifted lower after Cu NP encapsulation – a shift that was absent for Cu/ZrO$_2$, possibly due to insufficient interfacial contact. The importance of the interfacial interaction was further evidenced from a control experiment. Instead of encapsulation, Cu NPs were directly mixed with UiO-66 and the obtained mixture, Cu on UiO-66, exhibited a much lower yield of methanol than did Cu⊂UiO-66 (**Figure 42**). This experiment highlights the role of exposed MOF nodes as highly dispersed meta-oxides potentially capable of engendering strong metal-support interactions of catalytic significance. Evidence for charge transfer between Cu and exposed nodes in UiO-66 has been reported by Kobayashi, *et al.*[284] They further demonstrated that by functionalizing the organic linker, the degree of charge transfer can be tuned and the corresponding catalytic activity can be modulated.

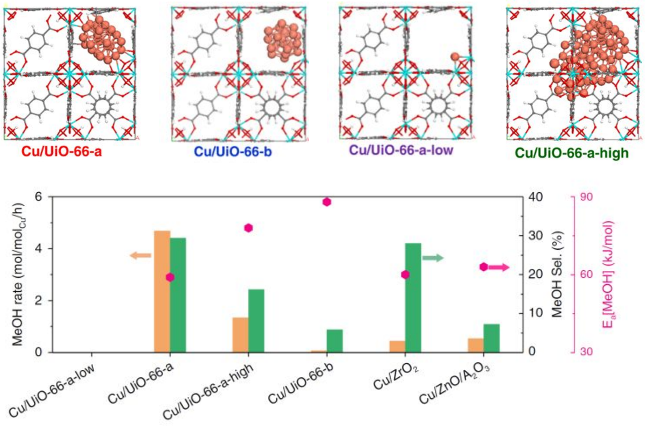

Figure 41. (Top) Proposed structural models of Cu/UiO-66; (Bottom) The effect of Cu-Zirconia interfacial sites in Cu/UiO-66 on its catalytic behaviour in CO$_2$ hydrogenation to methanol. Adapted with permission from Ref. 285. Copyright 2020 Springer Nature.

The mechanistic significance of the interfacial contact between Cu NPs and exposed zirconia-like MOF-nodes in boosting the catalytic activity and selectivity for CO$_2$ hydrogenation has been studied in detail by Zhu, *et al.*[285] Using dissolved Cu(OAc)$_2$ or Cu(NO$_3$)$_2$ as a metal NP precursor, a closely related pair of materials, having similar Cu loadings (1.4 and 1.8 wt%), was synthesized through SIM-like “ion exchange” (Cu^{2+} and 2H$^+$ exchange on hydroxo-presenting nodes); the materials were denoted Cu/UiO-66-a and Cu/UiO-66-b, respectively. Despite similar loadings, the fraction of Cu-O-Zr interfacial sites present following H$_2$ reduction of Cu^{2+} at 200°C was found to differ drastically for the two forms. From XAS measurements, they were 0.34 and 0.10 for Cu/UiO-66-a and Cu/UiO-66-b, respectively. Also examined was the dependence of catalytic activity on loading of Cu(OAc)$_2$-sourced copper. The authors conclude that in the low-loading limit, Cu is present mainly as single (cationic) atoms attached to the node, while in the high-loading limit copper is present mainly as nanoparticle-consolidated, zero-valent atoms (see the proposed structures in **Figure 43**). Differences in catalytic activity across the various versions of Cu/UiO-66 spanned nearly two orders of magnitude. From extensive experimental measurements together with DFT calculations, the authors conclude that: a) strong adsorption and concentration of CO_2 at the aforementioned interfacial sites are essential for high catalytic activity, and b) proximal metallic copper serves to dissociate molecular H_2 into reactive H atoms.

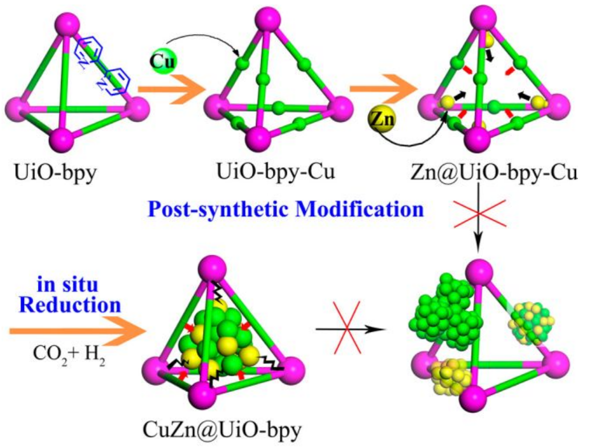

Figure 42. Synthetic scheme for confinement of ultrasmall Cu/ZnOx nanoparticles in UiO-bpy. Adapted with permission from Ref. 286. Copyright 2017 American Chemical Society.

An, *et al.*[286] substantially boosted interfacial contact area between MOF nodes and metal NPs through *in-situ* generation of small Cu/ZnO_x NPs confined by the pores of the framework of UiO-bpy (**Figure 44**). Using the material's bipyridine linker for metalation with Cu(II), together with a binding-site-presenting Zr_6-oxo, hydroxo node for subsequent Zn installation, Cu and Zn species can be immobilized in close proximity and form alloys upon reduction, with pore-defined particle sizes below 1 nm. (Note that even in a perfectly twelve-connected UiO-type MOF, the M_6 node presents four potentially reactive bridging-hydroxo sites for Zn(II) binding.) XPS, H_2 temperature-programmed desorption (TPD), and CO_2 TPD all pointed to a strong metal-support interaction between Cu/ZnO_x and the MOF SBUs, including both the bpy linker and Zr node. A high degree of mixing between Cu and ZnO_x facilitates the formation of low-average-valence-state Zn under CO_2 hydrogenation conditions, and affords 100% selectivity for methanol and higher activity than obtained with traditional Cu/ZnO/Al_2O_3 catalysts.

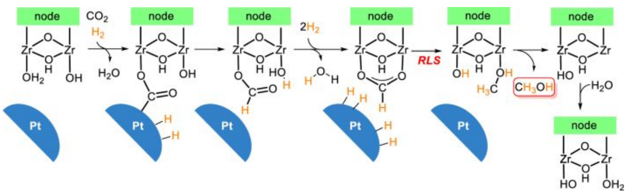

Figure 43. Proposed mechanism of methanol production at the interface of Pt NPs and Zr node of the MOF. Adapted with permission from ref. 289. Copyright 2020 American Chemical Society.

A series of studies by Gutterød and co-workers[287] revealed that Pt@UiO-67 is catalytically competent for H_2 based reduction of CO_2, with the initial report describing formation of CO and the classic Sabatier reaction product, methane. Subsequent mechanistic[288] and structural studies,[289] including studies of the influence of missing-linker defects, permitted the reduction to be optimized for methanol production. The researchers found that the interfacial sites where Pt NPs and Zr nodes interact thus serve as the meeting point for formate produced at the node from zirconia-sorbed CO_2 and H atoms formed by dissociation of H_2 by Pt (**Figure 45**). Thus, a key feature of the composite material is its ability to confine and connect these complementary catalytic components.

3.2.2 Clusters and Single-Atom Catalysts

MOF nodes, especially those consisting of metal-ion/oxy clusters, can be viewed as structurally well-defined nanoscopic analogues of conventional metal-oxide supports for heterogeneous catalysts. Support electronic effects, Lewis acid effects, and ligation effects from installed molecular modifiers will be discussed here.

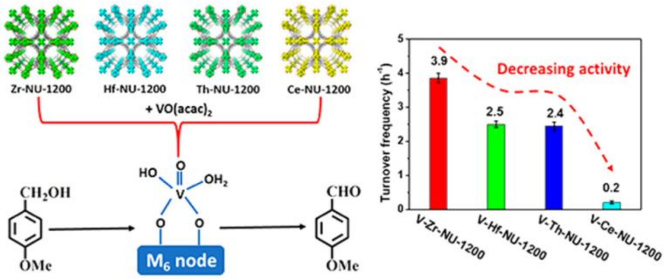

Figure 44. Vanadium catalyst supported on an isostructural series of transition metal, lanthanide, and actinide-based MOFs. Reaction scheme for alcohol oxidation and trend in TOF versus node composition. Adapted with permission from Ref. 290. Copyright 2019 American Chemical Society.

Wang, *et al.*[290] systematically studied the influence of MOF SBUs on the catalytic activity of supported V(V) species using four isostructural versions of NU-1200 (hexa-Zr(IV)-, Hf(IV)-, Th(IV)-, and Ce(IV)-oxy nodes, see **Figure 7**). Using SIM, they installed single V(V) ions on nodes and evaluated catalytic activity for methoxybenzyl alcohol oxidation (**Figure 46**). They found that the catalytic activity decreases by *ca.* 1.6-fold from Zr(IV) to Hf(IV)/Th(IV) and by *ca.* 20-fold from Zr(IV) to Ce – effects that were attributed to regulating the electronic properties of supported V species based on differences in electronegativity for node metal ions. The outsized effect of cerium evidently is due to partial reduction during vanadium instillation such that the nodes comprise a mixture of oxy-linked Ce(III) and Ce(IV) ions.

Related support-imparted differences have been seen for Ni(II)-catalysed hydrogenation of ethylene.[291] In addition to electronic modulation achieved by varying metal(IV) composition of nodes, the binding motif of supported Ni(II) species was observed, *via* SCXRD, to differ for a Zr-based MOF versus a Hf-based MOF, despite apparently identical node proton configurations.

Changes in catalyst speciation as function of metal-in-composition of isostructural node-based supports was also reported for catalytic copper(II). He, *et al.*[109] deposited Cu(II) on nodes of MOF-808, with either hexa-Ce(IV)-oxy or hexa-Zr(IV)-oxy nodes (**Figure 47**). Composition assessment together with EXAFS-based structural analysis revealed that both materials take up ~3 copper ions per node. On Ce-MOF-808 as a support, the installed ions are configured exclusively as mononuclear Cu(II) species. In contrast, Zr-MOF-808 supports Cu species with higher nuclearities. The compositional and structural differences translate into differences in activity of supported Cu(II) as an oxidation catalyst. The rates of cyclohexane oxidation and CO oxidation are greater by factors of 4 and 20, respectively, for Cu on Ce-MOF-808 versus Cu on Zr-MOF-808. For conventional ceria, partial conversion of Ce(IV) to Ce(III) is typically accompanied by oxygen loss and formation of lattice oxygen vacancies that can activate O_2. To our knowledge, however, similar redox-driven formation of oxygen vacancies has not been reported for cerium-based nodes in MOFs, suggesting that other factors (perhaps differences in catalyst nuclearity) are responsible for the enhanced activity of Cu(II) when supported on Ce-MOF-808.

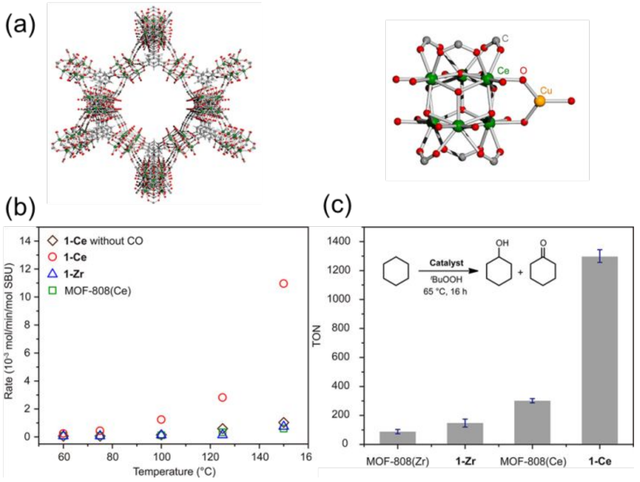

Figure 45. (a) structural illustration of pristine MOF-808 and Ce-based node after Cu deposition; (b) CO oxidation and (c) cyclohexane oxidation reactivity of 1-Zr, 1-Ce and control materials. Adapted with permission from Ref. 109. Copyright 2020 American Chemical Society.

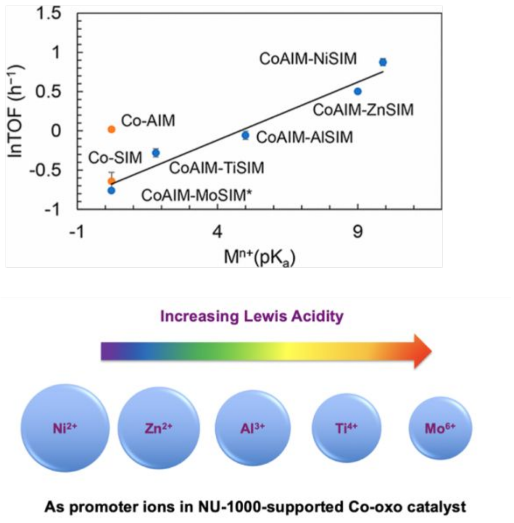

Figure 46. Plot depicting the trend between the pK_a of the promoter ion and the catalytic activity of the NU-1000-supported catalysts. Adapted with permission from Ref. 100. Copyright 2017 American Chemical Society.

Li, *et al*.[292] installed Co(II) on nodes of NU-1000 *via* both AIM and SIM to achieve selective oxidative dehydrogenation of propane under 230 °C and 2 bar – comparatively mild conditions for this reaction. Capitalizing on this reactivity, the same researchers in follow-up work installed metallic promotor ions spanning a range of Lewis acidity (M = Ni(II) < Zn(II) < Al(III) < Ti(IV) < Mo(VI)) on NU-1000, prior to Co(II) AIM, see **Figure 48**.[100] The isolated failure has been ascribed to the inability of node-grafted Mo(VI) to present hydroxo or aqua ligands for reaction with the vapor-phase AIM/ALD precursor for oxy-Co(II); instead Mo(VI) presents only unreactive oxo ligands and the cobalt-containing precursor binds directly to the hexa-zirconium node, presumably *via* reaction with residual μ_3-OH ligands. As shown in **Figure 48**, the catalytic activity of supported cobalt for oxidative dehydrogenation varies inversely with the Lewis acidity of the pre-installed promotor, *i.e.* Ni(II) > Zn(II) > Al(III) > Ti(IV) > Mo(VI). Earlier DFT modeling[292] suggested that an oxyl species, Co(III)–O•, abstracts a hydrogen in the rate-determining step. Presumably, the Lewis acidity of the promoter fine-tunes the electron spin density on the oxyl radical.

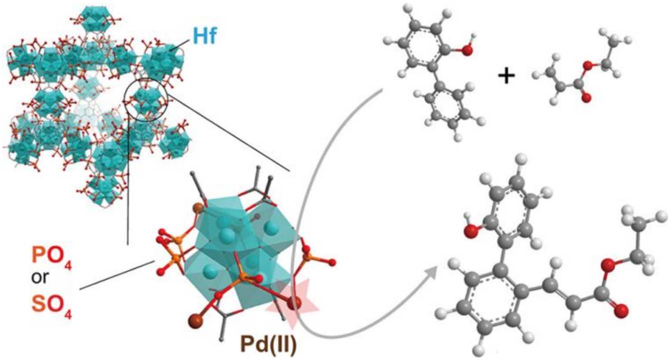

Figure 47. Phosphate and sulfate functionalized MOF-808 stabilized the Pd(II) sites for the oxidative Heck reaction. Adapted with permission from ref. 299. Copyright 2019 American Chemical Society.

The ease of functionalization of MOF nodes provides additional opportunities to mimic and revisit traditional catalytic systems using well-defined templates. Following work by Yaghi, Somorjai, Howarth, and others,[293-298] Otake, *et al.*[299] synthesized sulfated and phosphated versions of Hf-MOF-808 and then used them to support isolated Pd(II) ions. Recall that the protonated form of a sulfated metal-oxide is highly Brønsted acidic – perhaps even super-acidic, *i.e.* more acidic than concentrated sulfuric acid. A SCXRD-derived structure of Pd@Hf-MOF-808-PO_4 revealed two distinct Pd(II) sites – one binding to the chelating oxygen between PO_4^{3-} and the node, and the other directly binding to a phosphate oxygen (**Figure 49**). Compared to the pristine Hf-node, the modified node proved capable of stabilizing Pd(II) against reduction and aggregation into Pd(0) NPs, as evidenced by XPS after H_2 treatment.

Used as a model reaction for catalyst evaluation was an oxidative Heck reaction, where catalysis entails a Pd(II)/Pd(0) redox cycle and, therefore, an opportunity for neutral-metal-atom migration and unwanted formation of zero-valent palladium nanoparticles. Functionalization leads to an increase in the initial turnover frequency (TOF) for the Pd-catalysed Heck reaction by ~5-fold with sulfate and ~15-fold with phosphate, compared to simple Pd@Hf-MOF-808. Consistent with experimental data, DFT calculations showed that one important effect of oxy-anion functionalization of Hf_6 is to stabilize Pd(0) against migration and eventual agglomeration into unwanted Pd NPs.

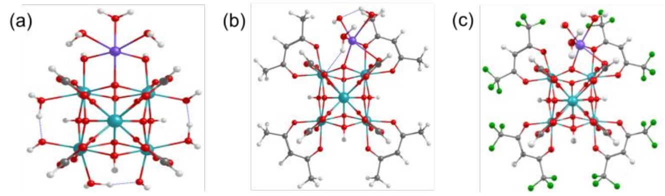

Figure 48. The Zr_6 node structures of (a) Ni-NU-1000; (b) Ni-Acac-AIM-NU-1000; (c) Ni-Facac-AIM-NU-1000. Color: C, grey; H, white; O, red; F, green; Ni, purple; Zr, cyan. For clarity, linkers are truncated and shown as formate groups. The indicated Ni ion is derived from computations. Adapted with permission from ref. 300. Copyright 2018 American Chemical Society.

Liu, *et al.*[300] reported on the vapor-phase installation of molecular modifiers, hexafluoroacetylacetonate ($Facac^-$) or acetylacetonate ($Acac^-$), in chelating fashion, as established by SCXRD, on each of four accessible Zr(IV) ions on the Zr_6 node of NU-1000. The binding increases the node's effective connectivity from eight to twelve, leaving only spatially isolated μ_3-OH node sites available for reaction with, and attachment of, candidate metal catalysts. They then installed Ni(II), a known catalyst for ethylene polymerization that, in the absence of node modifiers, forms as a node-linking tetranuclear metal-oxy cluster (see **Figure 50a**). The catalysts featuring (f)acac^{1-} modified nodes proved ineffective for oligomerization, but highly selective for butene formation, *i.e.* ethylene dimerization. DFT calculations indicated that, in the presence of mononuclear oxy-Ni(II), the installed (f)acac^{1-} species shift from strictly node-coordination to binding of both the node and added nickel, see **Figure 50b and c**. The calculations further showed that the coordinative presence of the molecular modifiers preferentially increases the activation energy for ethylene addition to C_4, thereby suppressing chain propagation and favouring the release of 1-butene as the main product.

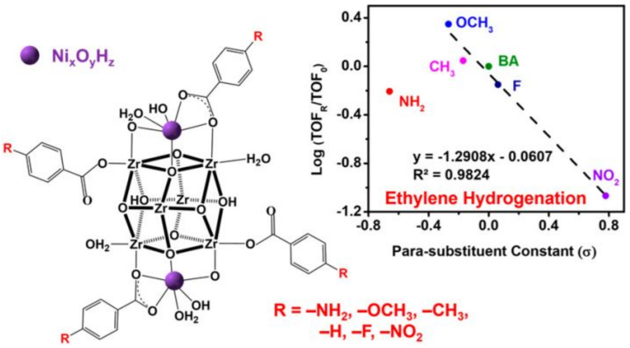

Figure 49. Structural representation of Ni-AIM-NU-1000 catalysts modified with para-substituted benzoate ligands (left), and corresponding plot of log(TOF) vs. electron-donating/withdrawing character demonstrating effect of nonstructural ligands on reactivity (right). Adapted with permission from Ref. 301. Copyright 2019 American Chemical Society.

A superficially similar strategy for node modification, but based on *para*-substituted benzoate modifiers, has been described and applied to ethylene hydrogenation by Ni-NU-1000.[301] The authors' goal initially was to modulate the electronic properties in a fashion similar to that illustrated in **Figure 50** for metal-ion-based promoters, but now indirectly *via* ligation of support metals (Zr(IV) sites) with organic species of varying electronic donating or withdrawing character, as measured, for example, by Hamett's empirical "para-σ" parameter. As shown in **Figure 51**, a linear correlation between log(TOF) and the electron donating/withdrawing character of substituted benzoate can be drawn – seemingly supporting the notion of indirect modulation of catalyst activity via organic ligation of surrounding metal ions in the inorganic support. However, SCXRD measurements unexpectedly revealed that substituted benzoates bind to the node via a single carboxylate oxygen,[244, 301] leaving a second oxygen atom potentially available for binding directly to the catalytic nickel ion. DFT calculations indicate that this direct interaction between catalytic nickel and the benzoate-based node-ligand/catalyst-promoter, rather than indirect, support-mediated, electronic tuning, is primarily responsible for the rate-tuning illustrated in **Figure 51**. So, it remains to be seen whether indirect tuning of catalytic activity *via* nonstructural-ligand-modulation of support electronic properties can contribute significantly.

3.3 Cavity and Framework Enhanced or Enabled Catalytic Activity and Selectivity

3.3.1 Activity

$[IPrAu(III)(biphenyl)]^+$ (where IPr = 1,3-bis(2,6-diisopropylphenyl)imidazole-2-ylidene) is an effective homogeneous catalyst for cycloisomerization of enyne species. The catalyst is susceptible, however, to decomposition and deactivation *via* reductive elimination of biphenyl to yield biphenylene and a noncatalytic gold(I) complex. Toste, Yaghi, and their co-workers[302] reasoned, however, that if the biphenyl ligand of the catalyst was carboxylate-functionalized and then used as a linker in a sufficiently rigid MOF, formation of biphenylene would be impossible, and reductive-elimination-based decomposition of the now-heterogenized catalyst could be inhibited or altogether eliminated. As illustrated in **Figure 52**, they succeeded in integrating a pre-catalyst with the zinc-node containing framework, IRMOF-10 and the two-fold catenated, zirconium-node containing framework, bio-MOF-100. Chloride ligand removal creates a potential active-site on gold(III), and indeed, the MOF-immobilized, chloride-free version of the complex is both catalytically competent and immune to deactivation by reductive elimination of biphenyl and conversion to biphenylene. Pointing to the potential for generalization, they termed the strategy "architectural stabilization."

fac-$Re^I(CO)_3$(2,2'-bpy)X and *fac*-$Mn^I(CO)_3$(2,2'-bpy)X are well-known pre-catalysts that upon reduction and loss of a halide ligand (X^-), can catalyse the two-electron reduction of CO_2 to CO.[303] Typically the mechanism entails dimerization of radical •$Mn(CO)_3$(2,2'-bpy) or •$Re(CO)_3$(2,2'-bpy) species *via* metal-metal bond formation, with the CO_2-binding form of the catalyst being obtained only upon further reduction and concomitant severing of the metal-metal bond.[304-305] Fei and co-workers[149] showed that the manganese pre-catalyst can be heterogenized by first including carboxylate-terminated 2,2'-bipyridine in place of a fraction of carboxylate-terminated biphenyl linkers in UiO-67 (see **Figure 16**, left side) and then reacting with $Mn(CO)_5Br$. Wang and co-workers[306] described a similar outcome for a rhenium pre-catalyst, but with a pre-assembled carboxylate-functionalized version of the rhenium compound being directly doped into UiO-67 at the MOF synthesis stage. When MOF-immobilized, neither catalyst has the ability to dimerize and, consequently, catalysis of CO_2 reduction to CO follows a different pathway, involving reduction of both a single metal centre and a ligated polypyridine – a supposition confirmed experimentally by Fei, *et al.*

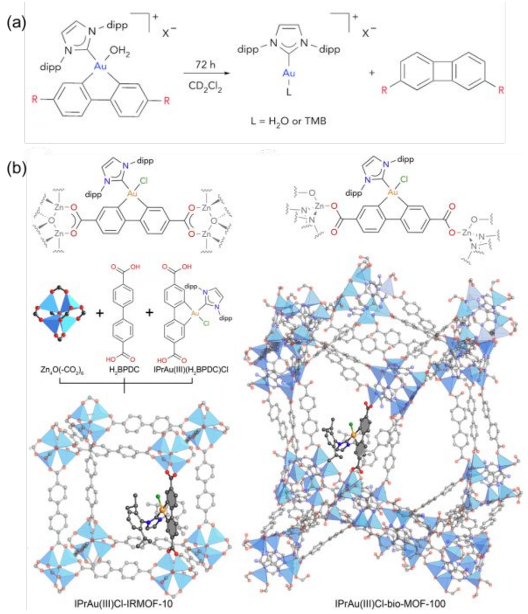

Figure 50. (a) Synthesis of active Au(III) complex; (b) Crystallography-supported representations of the cycloisomerization pre-catalyst, IPrAu(III)(BPDC)Cl, integrated with biphenyl-containing, porous frameworks, IRMOF-10 and bio-MOF-100. Adapted with permission from ref. 302. Copyright 2020 Cell Press.

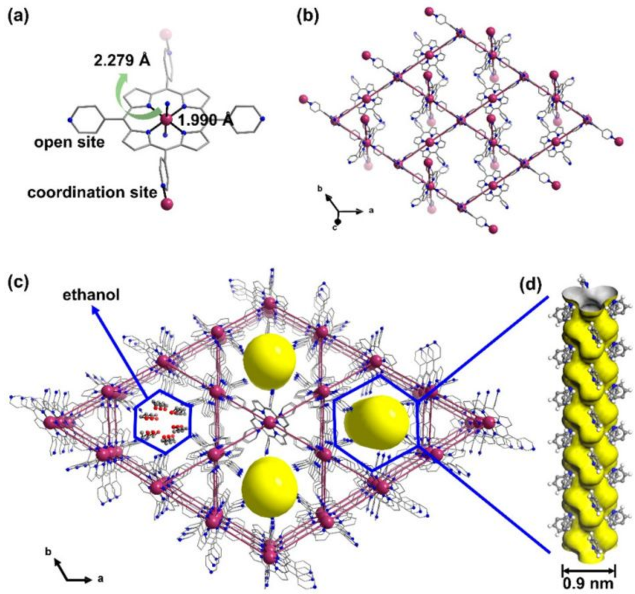

Figure 51. Building blocks of KLASCC-1 and the molecular architecture showing the inside channels and pyridyl units. Adapted with permission from ref. 184. Copyright 2020 American Chemical Society.

Cao, *et al.*[184] examined a porphyrin-based MOF called KLASCC-1 (KLASCC-1 = Key Laboratory of Applied Surface and Colloid Chemistry-1; see **Figure 53**). Note that cobalt(II)tetrakis(4-pyridyl)porphyrin functions as both linker and node. KLASCC-1 presents an unusual microenvironment: hexagonal channels present nitrogen-exposed porphyrin-pendant pyridyls in a high spatial density. Under mildly basic conditions (carbonate buffer), the MOF is competent for acid-catalysed (pyridinium-catalysed) hydrolysis of various orthoformates ($HC(OR)_3$ species) to formate and alcohols. The catalysis is substrate size-selective, consistent with a 9 Å channel width. Replacing channel pyridyls with inert phenyls yields, as expected, no catalytic activity. The rigid, size-selective pyridyl channel environment is an example of a catalysis microenvironment that would be challenging to emulate other than within a MOF structure or a supramolecular coordination complex.

In principle, and by analogy to protein environments proximal to active-sites in metalloenzymes, MOF linkers can define and/or modulate the chemical environment proximal to active-sites for abiotic catalysis. Choi, *et al.*[307] reported a systematic tuning of the product distribution from methylcyclopentane (MCP) conversion catalysed by Pt NPs embedded in nanocrystalline UiO-66 (**Figure 54**). Sulfonic acid (S) and ammonium (N), were chosen as strong and weak acidic functionalities, respectively, for the organic linkers and then incorporated into UiO-66 separately or together, in the presence of Pt NPs. The obtained materials, denoted as Pt⊂nUiO-66-S and Pt⊂nUiO-66-N, showed strikingly different selectivity in the gas-phase conversion of MCP. While the former material exclusively favours C_6-cyclic, the latter material decreases the selectivity for C_6-cyclic products to <50% while increasing the acyclic isomer selectivity to 39%.

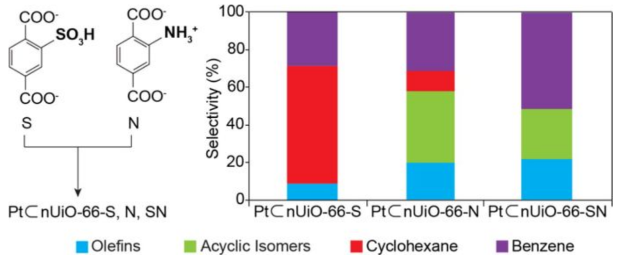

Figure 52. Acid group modified linker structures (left) and corresponding product selectivity for methylcyclopentane conversion with Pt NP composite catalysts. Adapted with permission from Ref. 307. Copyright 2015 American Chemical Society.

The interaction between functionalized linker and nanoparticle-based active-sites has been studied spectroscopically and theoretically by Li, *et al.*[308] using Pd@UiO-66-X (X = H, NH_2, OMe) as a model catalyst series, with the aerobic reaction between benzaldehyde and ethylene glycol as the test reaction (**Figure 55**). As shown in the figure, the product distribution, after 10 h, is essentially completely shifted from the acetal to the ester when the linker substituent is either changed from $-NH_2$ to −OMe or simply replaced with –H. To be more specific, while Pd@UiO-66-NH_2 effectively facilitates the formation of benzaldehyde ethylene acetal (94% selectivity), Pd@UiO-66-H and -OMe show high selectivity (90% and 97%, respectively) for the oxidation product, 2-hydroxyethyl benzoic acid. A closer inspection of the reaction kinetics reveals that at the 1 h mark, *all* versions of the catalyst yield the cyclic acetal as the predominant product; only later is the ester obtained. DRIFTS revealed that Pd NPs in Pd@UiO-66-NH_2 present an electron-enriched surface, presumably due to electron-donation by $-NH_2$ groups at the MOF/NP interface. Consistent with this interpretation, solution addition of aniline (amino benzene) leads to complete inhibition of ester formation for all three catalysts as well as for Pd/C. DFT calculations showed that proximal $-NH_2$ groups increase the chemical potential of Pd and diminish its ability to catalyse aerobic oxidation of the intermediate obtained in step **i** in **Figure 55a**.

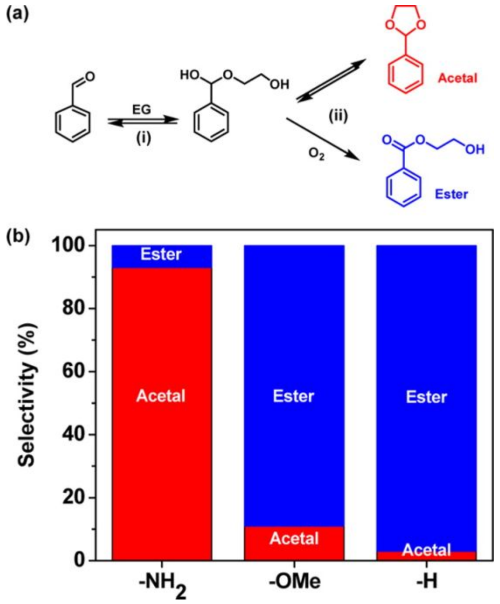

Figure 53. (a) Aerobic reaction between benzaldehyde and ethylene glycol. (b) Product distribution using Pd@UiO-66-X (X = H, NH_2, OMe). Reaction conditions: benzaldehyde (0.1 mmol), ethylene glycol (1.5 mL), Pd/substrate 1/100, 1 atm O_2, 90 °C, 10 h. Adapted with permission from Ref. 308. Copyright 2016 American Chemical Society.

Hexa-zirconium(IV), -halfnium(IV), and -cerium(IV) MOFs featuring displaceable node-sited aqua ligands are remarkably effective catalysts for hydrolytic degradation and detoxification of G-type nerve agents, as well as much-less-toxic chemical simulants.[309] Catalysis entails agent or simulant binding to a highly Lewis acidic site, such as Zr(IV), that can render a remote P-F bond (agent) or P-nitrophenoxide bond (simulant) susceptible to attack by aqueous hydroxide, a potent nucleophile.[196, 310] Missing-linker-defective UiO-66 is among the catalysts. Katz, *et al.*[311] found that simple functionalization of linkers with amino groups boosts by 20-fold the rate of hydrolysis of the simulant, 4-nitrophenyl phosphonate (DMNP), despite the absence of direct participation of pendant -NH_2 in the catalytic reaction. Comparisons to other UiO-66 derivatives seemingly ruled out, as an explanation, an inductive electronic influence upon the Lewis acidity of Zr(IV). Shown in **Figure 56** are members of a series of amino-functionalized linkers used to construct derivatives of Zr-MOFs UiO-66, UiO-67 and NU-1000, with the goal of understanding the origin of enhancement observed by Islamoglu and co-workers.[312] From the studies, only amino groups proximal to the catalyst active-site favourably influence hydrolysis. DFT calculations pointed to tuning of the immediate solvation environment of the catalyst-bound reactant as the origin of the enhancement.

Halogen-functionalization has also been reported to accelerate the rate of hydrolysis of a phosphorus-based chemical warfare simulant – another example of the pore-wall-defined environment beyond the active-site influencing catalytic activity. Briefly, Kalaj, *et al.*[313] synthesized a series of UiO-66-X MOFs (X = F, Cl, Br, I) for catalysis of DMNP hydrolysis and found that UiO-66-I elicited a significantly faster rate compared to the parent UiO-66. DFT calculations indicated that noncovalent interactions between the linker iodine atom and the methoxy group of DMNP renders the phosphorous atom more electrophilic and the phosphorous-oxygen (nitrophenoxide) bond more susceptible to rate-determining water (or hydroxide) attack. As an aside, for catalyst-enabled (Lewis acid enabled) hydrolytic detoxification, the nitrophenoxide leaving group in nerve-agent simulants is a remarkably good kinetic predictor of the behaviour of the phosphorous-attached fluoride ion found in actual G-type nerve agents.[314-318]

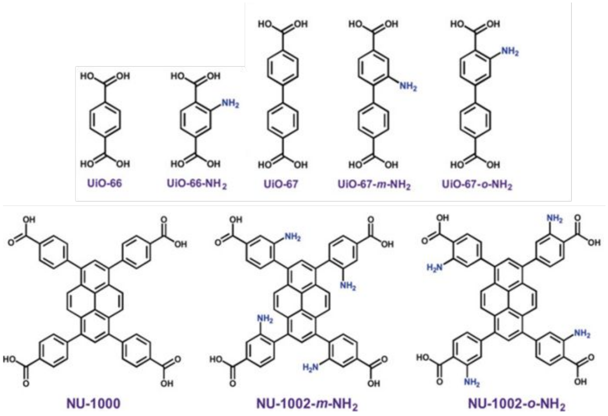

Figure 54. Amino-functionalized organic linkers of UiO-66/67 and NU-1000. Adapted with permission from Ref. 312. Copyright 2018 John Wiley and Sons.

MOF-integrated, redox-active, metal-oxy species, including nodes, grafted clusters, and POMs, are often catalytically effective for oxidation reactions, but less useful for catalysing reduction reactions. In view of the role of mononuclear, binuclear and/or cluster-based metal-sulfur species as electron carriers and as cofactors for enzyme-catalysed reduction of protons to molecular hydrogen, and N_2 reduction to ammonia, replacing or converting the above metal-oxy species with or to metal-sulfur (sulfide, disulfide, thiolate, sulfhydryl) species could render many of these species functional for MOF-integrated reductive catalysis.[98-99,319-324] Summarized in **Figure 57** are examples based on grafting single-metal-atom $Mo(SH)_2$ units to an open site on an eight-connected MOF. Grafting is accomplished with an oxo and a hydroxo ligand, leaving Mo(IV) with distorted tetrahedral coordination as evidenced by SCXRD and by a prominent pre-edge peak in the molybdenum XANES spectrum. The catalyst is competent for hydrogen evolution from aqueous acid when supplied with electrons either electrochemically[99, 322] or photochemically.[321] Note that the coordination number and coordination geometry for these

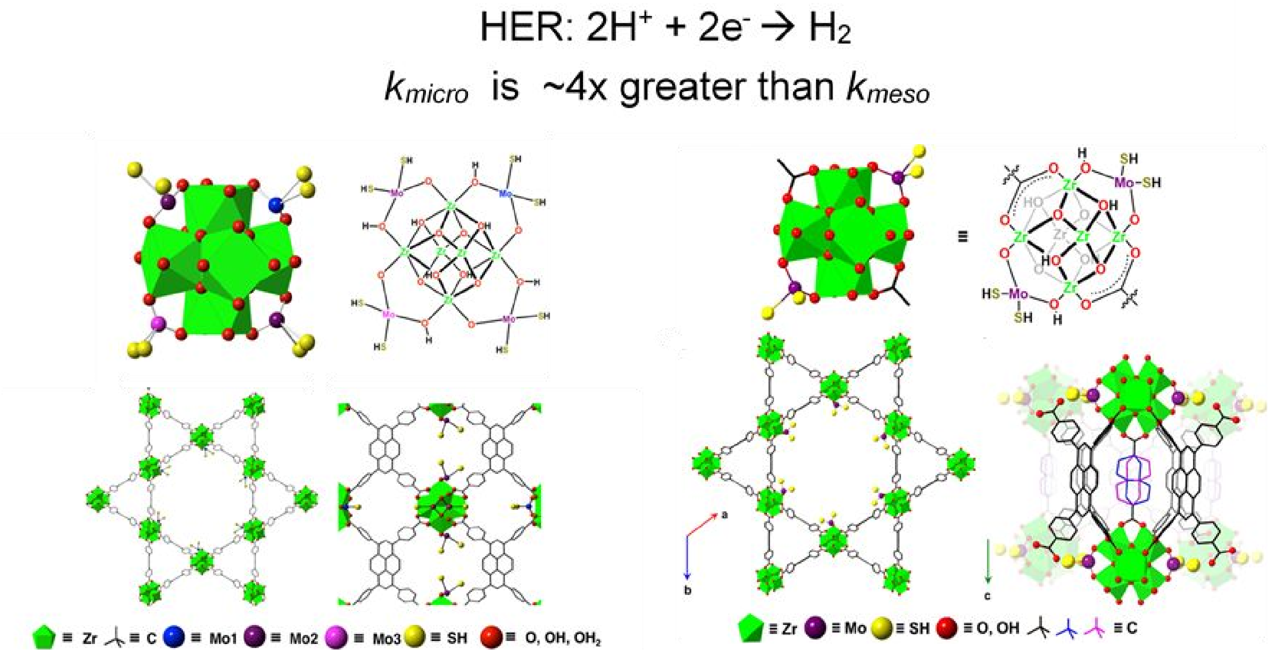

Figure 55. (left) The MoS_x-anchored Zr_6 node of the representative structure of MoS_x-SIM showing all the crystallographically distinct MoS_2 units (Mo1–Mo3) and the framework viewed along the c-axis and a-axis; (right) Crystallographic structure of MoS_2-SIM-NDC-SALI, where Zr_6 node with monometallic $Mo(SH)_2$ units allocated solely within the mesopore due to the NDC installation occupying c pores. Adapted with permission from refs. 99 and 322. Copyright 2018 American Chemical Society and 2020 John Wiley and Sons.

single-metal-atom sites differ from the nominally octahedral coordination environment of bulk molybdenum disulfide, a 2D layered material whose sulfur-rich edge sites (terminal sites) are known to be extraordinarily effective as electrocatalysts for HER (hydrogen evolution reaction). MoS_2-SIM-NU-1000 (**Figure 57 left**) is active for evolution of molecular hydrogen from aqueous acid.[99] When *c* pores are occupied/blocked by naphthalene dicarboxylate(NDC^{2-}), the single-metal-ion catalyst is directed into a water-filled, hexagon-shaped mesopore (**Figure 57 right**). Significantly, Noh, *et al.*[322] found that the mesopore-sited and *c*-pore-sited catalysts have indistinguishable local structures, but the latter is *ca.* four times more active. The remarkable difference was attributed to differing water structuring/ordering in the small versus large pores; unfortunately, the catalyst-proximal water structure could not be experimentally elucidated.

Linker-based light-absorption and photoredox behaviour offers a basis for driving oxidation or reduction reactions mediated by MOF-encapsulated enzymes. An example combination is NU-1006, a Zr-MOF featuring a pyrene-containing linker (chromophore) and **csq**-derived hexagonal channels of sufficient width (62 Å; see **Figure 58**), to encapsulate formate dehydrogenase. Together with a channel-anchored co-catalyst, a mobile redox mediator (NAD^+/NADH), and a sacrificial reagent for regeneration of the chromophore (linker) after electron transfer, formate-dehydrogenase@NU-1006 can be made to run in reverse and reduce CO_2 to formate.[325-326] Closely related conceptually is a study by Zhou and co-workers[52] of photo-excitation of porphyrin linkers in PCN-601, followed by electron-transfer to Ni(II)-containing nodes and then CO_2 reduction by the nodes; see **Figure 6** above.

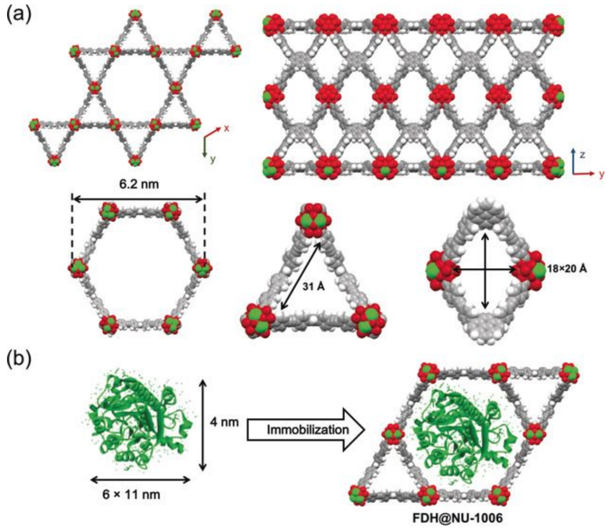

Figure 56. Crystal structure of MOF NU-1006 suggesting that hexagonal channels are wide enough to encapsulate formate dehydrogenase. The illustration for FDH@NU-1006 is an idealized representation based on separate crystal structures for the enzyme and MOF, rather than for FDH@NU-1006 itself. Adapted with permission from refs. 325. Copyright 2019 John Wiley and Sons.

3.3.2 Selectivity

In an important early study, Uemura, *et al.*[327] looked at pillared paddlewheel MOFs, specifically, $M_2(1,4\text{-BDC})_2(\text{ted})$ (ted (also called DABCO) = triethylenediamine, M = Cu^{2+} or Zn^{2+}), as potential templates for selective linear polymerization of *para-* or *meta*-divinylbenzene (DVB). These MOFs offer 7.8 x 7.8 Å 1D channels (along with channels that are too small to accommodate DVB). The larger channels were loaded to saturation with either *p*-DVB or *m*-DVB, and then exposed to AIBN (2,2'-azobis(isobutyronitrile)) as a radical initiator. Thus, in the absence of a template or other control, one would anticipate formation of random, polydisperse, and substantially cross-linked polymers. Instead, with the Zn(II) version of the MOF, both *m*-DVB and *p*-DVB reacted (albeit slowly) to yield linear polymers that retained one unreacted vinyl substituent per benzene. Polymer release was accomplished by intentionally sacrificing (*i.e.*, chemically degrading) the MOF.

The Cu(II) version of the MOF is essentially identical structurally to the Zn(II) version, but features somewhat stronger bonding between linkers and nodes. The Cu(II) is similarly effective for templating the radical-initiated, linear polymerization of *m*-DVB (where again, the MOF itself is not the catalyst), but *p*-DVB resists polymerization. The authors note polymerization requires direct contact between neighbouring vinyl groups and point out that closely channel-packed *p*-DVB, with molecular dimensions of 4.3 x 8.2 Å, does not quite achieve the needed proximity if the channel is rigid – presumably the case for $Cu_2(1,4\text{-}BDC)_2$(ted). With the zinc congener, however, channels can flex if comparatively weak node-linker bonds are reversibly broken. Overall, the study illustrates the remarkable chemical subtlety differentiating an effective reaction template from an ineffective one. Numerous follow-up studies,[328] including several since 2016 have built on and extended the templating idea.[329-332]

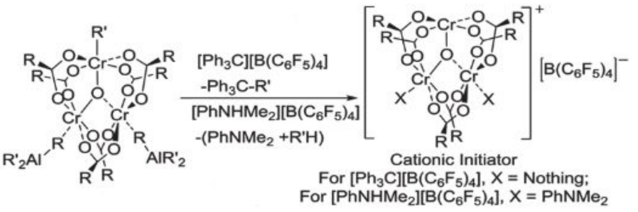

Figure 57. The generation of cationic initiator in the MIL-100(Cr)/101(Cr) /activator/AlR'3 systems. Adapted with permission from ref. 333. Copyright 2018 John Wiley and Sons.

Chromium versions of MOF MIL-100 and MIL-101, together with borate as an activator and $AlMe_3$ as a co-catalyst, were used by Gao, *et al.*[333] to engender product selectivity in isoprene polymerization. Both the product size and product shape can be tuned when reaction intermediates are confined in MOFs. MIL-100(Cr), possessing cages as large as 29 Å, is constructed from Cr_3-containing nodes and BTC linkers. MIL-101(Cr) also forms an interconnected-cage structure featuring Cr_3-containing nodes, but now with BDC linkers. The largest cage size is 34 Å. The methyl group on $AlMe_3$ first coordinates to sites on Cr that have been obtained activating the MOF at 200°C, and then removed by the borate activator. When borate **A,** $[Ph_3C][B(C_6F_5)_4]$, was used as the activator for the polymerization of isoprene, both MIL-100(Cr) and MIL-101(Cr) yielded totally cyclized polyisoprene (PIP) with low molecular weights and narrow molecular weight distributions. In contrast, when borate **B**, $[PhMe_2NH][B(C_6F_5)_4]$, was used as the activator, both MOFs yielded linear *cis*-1,4-polyisoprene (*cis*-1,4-PIP) as the main product. The differences in selectivity were attributed to the coordination capability of one of the byproducts within the limited pore space of the MIL compounds. As shown in the proposed initiator generation scheme (**Figure 59**), the byproduct Ph_3CMe from formation of the cationic initiator does not bind to chromium. In contrast, the byproduct $PhNMe_2$ generated from **B**, does bind to the Cr centre (via the nitrogen lone pair), thereby partially filling the MOF cavity. In the absence of byproduct binding (case **A**) the pore volume is sufficient for catalysis via a cyclization pathway entailing β-H elimination of the allyl carbocation. In the presence of byproduct binding (case **B**), cyclization is sterically suppressed, catalysis occurs mainly via simple chain transfer, and the dominant product is linear *cis*-1,4-PIP.

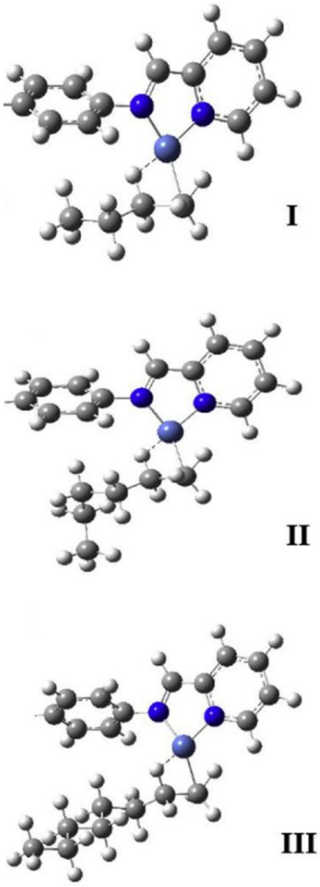

Figure 60. DFT-optimized structures of the reaction intermediates that generate 1-butene, 1-hexene and 1-octene. Light blue = Ni, dark blue = N. Adapted with permission from ref. 334. Copyright 2020 Elsevier.

Chen, *et al.*[334] reported that Ni-ion grafting to the linkers of MIL-125(Ti) (Ni-MIL-125(Ti)) yields an ethylene oligomerization catalyst that is selective for C_6 products. This work presents a chemically interesting departure from the general observation that late transition-metal catalysts yield oligomers with broad distributions with respect to both size and degree of branching, as these catalysts typically make use of a Cossee-type mechanism that leads to the formation of both α-olefins and branched by-products. DFT calculations pointed to a major role for pore confinement in Ni-MIL-125 in controlling the length of the carbon chain. **Figure 60** shows the optimized structures of intermediates believed to give rise, *via* β-H elimination, to C_4, C_6, and C_8 oligomers. The calculated volumes of candidate intermediates **I**, **II**, and **III** are *ca.* 0.71 cm^3/g, 0.73 cm^3/g, and 0.76 cm^3/g, respectively. The calculated volume of intermediate

III slightly exceeds the pore volume of Ni-MIL-125(Ti) (*ca.* 0.75 cm^3/g). The resulting steric constraint evidently imposes a sufficiently large energy penalty that little intermediate **III** and, therefore, little C_8 product can be formed.

Figure 58. Molecular mechanics-optimized configuration of reaction intermediates residing on the porphyrin pairs of (a) PCN-222, (b) NU-902, and (c) MOF 525. Adapted with permission from refs. 335. Copyright 2016 American Chemical Society.

Deria, *et al.*[335] employed a series of Zr-based (porphinato)-Zn MOFs – NU-902 (**scu**), MOF-525 (**ftw**), and PCN-222 (**csq**) – as catalysts for acyl transfer from N-acetylimidazole (NAI) to each of three pyridylcarbinol (PC) regioisomers (2-PC, 3-PC, and 4-PC). The catalytically salient effects of the Zn(II) centres are: a) to pre-concentrate reactants via axial coordination of reactant nitrogens, b) to activate NAI, in a Lewis-acid sense, to release its acyl component, and c) to orient the various planar reactants normal to the plane defined by a Zn(II)-porphyrin linker. Effect "a" appears to be the greatest contributor to acceleration of the reactions, although "b" also clearly contributes. Effect "c" is responsible for selectivity, with the extent of selectivity depending on the relative spatial orientations of reactant-binding pairs of porphyrins. The orientations, in turn, are defined by the corresponding topologies, such that the resulting alignment or misalignment of various reactant pairs differs as a function of MOF topology. **Figure 61** presents molecular-mechanics-optimized structures of transition states for porphyrin-oriented NAI/3-PC pairs in each of the MOF-topology-defined reaction cavities.

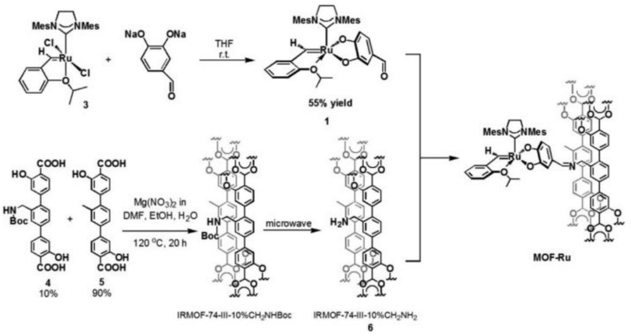

Figure 59. Illustration of the convergent synthesis of Ru-based molecular catalyst and mixed-linker MOF IRMOF-74-III. Adapted with permission from ref. 336. Copyright 2016 American Chemical Society.

Yuan, *et al.*[336] reported a synthesis of IRMOF-74-III(Mg) that is convergent with structurally well-defined channel-tethering of a preformed molecular Ru catalyst *via* covalent bond formation between the amine-functionalized organic linker and aldehyde-modified Ru catecholate catalyst (**Figure 62**). IRMOF-74-III is a linker-expanded version of MOF-74.[337] It is isoreticular with MOF-74, see **Figure 7,** so it offers the same **etb** topology and similarly presents 1D hexagonal channels. The as-synthesized, catalyst-containing material is active for self-metathesis and ring-closing metathesis of terminal olefins. As one might anticipate, the channel-integrated catalyst displays substrate-size-selectivity that is absent outside the MOF.

An example from Huxley, *et al.*,[338] while stoichiometric rather than catalytic, illustrates how the size of the substrates and the distance between the spatially isolated reactive sites inside the pores can dictate the regioselectivity of products. A Mn(II)-based MOF, $[Mn_3(\mathbf{L})_2(\mathbf{L'})]$ ($H_2\mathbf{L}$ = bis(4-(4-carboxyphenyl)1*H*-3,5-dimethylpyrazolyl)methane, **L'** = uncoordinated bis(3,5-dimethylpyrazol-1-yl)methane), was functionalized with azide moieties, $Mn(I)(CO)_3N_3$. Through SCXRD, it was found that the azide groups were located 13 Å apart (**Figure 63a**). This material was next used for size-selective transformation of dialkynes into alkyne-functionalized triazoles. A series of linear dialkynes of increasing carbon numbers, *DA1-3*, were made, with lengths of 10.7, 13.1, and 15.6 Å. As anticipated, high regioselectivity was realized for the shortest *DA1*, as only one terminal alkyne group can approach the azides at once. On the other hand, the lengths of *DA2* and *DA3* approached and even exceeded the distance between neighbouring azides (**Figure 63b**). Consequently, both terminal alkyne groups sufficiently proximal with the separate azides to generate a mixture of bis- and monotriazole products. One could imagine similar strategies for other regioselective transformations.

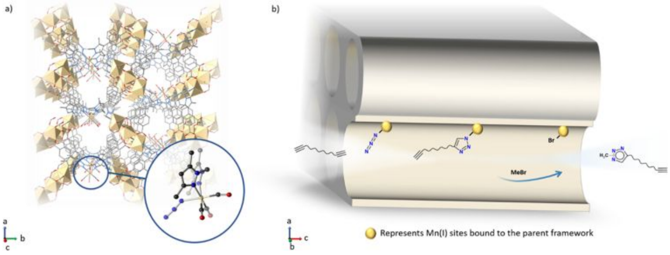

Figure 60. (a) Representation of the azide reactive sites connected with the added Mn(I) centre in Mn(II)-based MOF along the c-axis. (C, dark gray; N, blue; O, red; Mn, beige; H atoms omitted for clarity); (b) Graphical depiction of the site-isolation strategy, showing the introduction of the dialkyne, its "click" conversion using the separated Mn(I) sites, and then alkylation with MeBr to produce the desired N-methyl alkynyl triazole along the 1D channels. Adapted with permission from ref. 338. Copyright 2018 American Chemical Society.

Unexpected product formation and selectivity have been observed in confined MOF systems for other reasons. With hydroformylation of 1-hexene as a probe reaction, Bauer, *et al.*[339] showed that a 0.23 mol_{Co}% solution of a homogeneous catalyst, $Co_2(CO)_8$, complex can achieve a selectivity of 50% towards branched products for hydroformylation at 40% conversion. However, by preferentially adsorbing the $Co_2(CO)_8$ complex to the interior of MixUMCM-1-NH_2 $[Zn_4I(btb)_{4/3}(bdc)_x(abdc)_{1-x}$, btb = 4,4',4'',-benzene-1,3,5-trisbenzoate; bdc = 1,4-benzenedicarboxylate; abdc = 2-amino-1,4-benzenedicarboxylate, UMCM = University of Michigan Crystalline Material] (**Figure 64**), the selectivity towards branched products can be increased to 75% at similar conversion (36%). Based on Monte Carlo simulations, the enhanced selectivity for branched products with Co@MOF as the catalyst was ascribed, in part, to adsorption/partition driven increases in the local concentration of olefin in micropores, relative to the olefin concentration near the free catalyst in homogeneous solution. The increases, when combined with the right pore environment, can favourably alter the kinetics of the reaction. Using empirically determined kinetic laws for the hydroformylation of propene, rates of formation of the branched and of the linear products were calculated and qualitatively compared. A strong positive correlation was found between the calculated changes in the ratio of relative rates of formation and the observed selectivity toward branched aldehydes, lending credibility to the notion that greatly increased substrate concentration in the vicinity of the MOF-supported cobalt active-site accounts for the selectivity enhancement. The study further suggested that in the absence of the adsorption-based boost in local concentration of substrate, similar alteration of selectivity would be impossible to accomplish and would, therefore, be unattainable in a homogeneous solution.

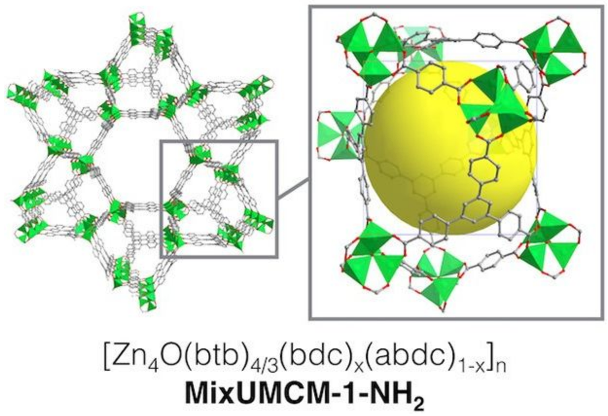

Figure 61. Structure and molecular formula of MixUMCM-1-NH$_2$. Adapted with permission from ref. 339. Copyright 2020 Springer Nature.

The effect of closely surrounding node-attached catalyst mononuclear metal catalyst active-sites (single cobalt ions) by MOF linkers was studied by Manna, *et al.*,[340] specifically for C-H bond activation reactions (borylation reactions). As shown in **Figure 65**, the catalyst is attached to the node of nominally twelve-connected UiO-68 *via* a bridging oxo, rather than *via* terminal oxy ligands at missing-linker-type defect sites (*cf.* **Figure 10** and copper-ion siting on UiO-66). Additionally, the cobalt ion is weakly ligated by a pair of node-connected carboxylate oxygens (linker terminus atoms). Notably, UiO-68 is inherently more stable than UiO-67, and can be prepared with a lower density of defect sites than typically achievable with either UiO-66 or UiO-67.[341] Thus, cobalt attachment via node bridging-ligands can serve effectively to render site-access selective for minimally sterically demanding substrates. Indeed, the researchers documented selectivity for substrates presenting *sp^3* benzylic C-H bonds rather than aryl C-H bonds.

Xiao, *et al.*[342] demonstrated how the selectivity of catalytic cyclohexane oxidation can be altered by tuning the interaction between the functional groups on the organic linkers and the reactants. In this work, the linker of Fe$_2$(dotpdc) (H$_4$dotpdc = 4,4″-dihydroxy-[1,1′:4′,1″-terphenyl]-3,3″-dicarboxylic acid) was modified with four functional groups of increasing bulkiness and hydrophobicity (H < F < CH$_3$ < *t*Bu). It was found that the aldehyde:ketone (A:K) ratio increased from 2.8:1 to 8.4:1, with an increase in TON from 4 to 19, as the functional group became bulkier and more hydrophobic. This observation was further investigated with cyclohexane isotherms at 298, 308, and 318 K, where the isosteric heats of adsorption (Q$_{st}$) were calculated for the four materials. The absolute Q$_{st}$ values trend with the A:K selectivity precisely, suggesting that the more hydrophobic moieties induce

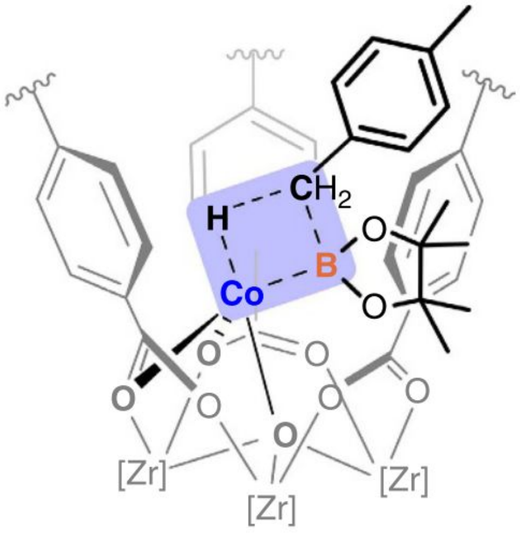

Figure 62. Model of the proposed active-site structure during chemoselective borylation of a methyl substituent of p-xylene. Notice that cobalt is anchored primarily by coordination of a bridging oxo ligand of the node of UiO-68 and secondarily via weak coordination to node-connected carboxylate oxygen atoms from a pair of linkers. For a contrasting mode of single-metal-ion immobilization on a UiO-type MOF, see **Figure 10**. Differences in density of missing linker defects – low for UiO-68 and high for for UiO-66 – may account for the differences in mode of immobilization. Adapted with permission from ref. 340. Copyright 2016 Springer Nature.

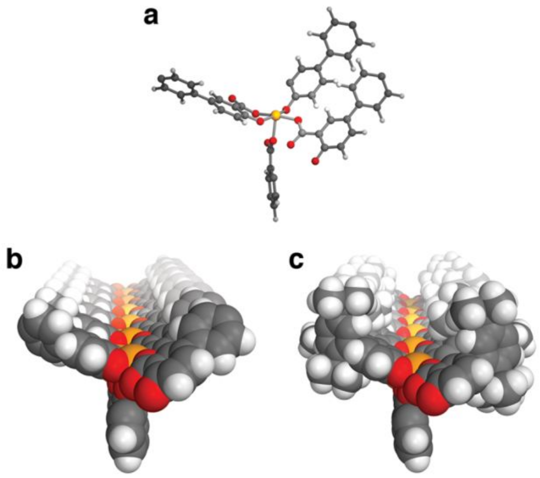

Figure 63. (a) Local structure of the iron (II) centres in Fe$_2$(dotpdc). (b) Space-filling model of Fe$_2$(dotpdc) as viewed along the channel axis. (c) Space-filling model of the iron (II) centres of Fe$_2$(dotpdc^{tBu}) as viewed along the channel axis. White, gray, red, and orange spheres represent H, C, O, and Fe, respectively. Adapted with permission from ref. 342. Copyright 2016 American Chemical Society.

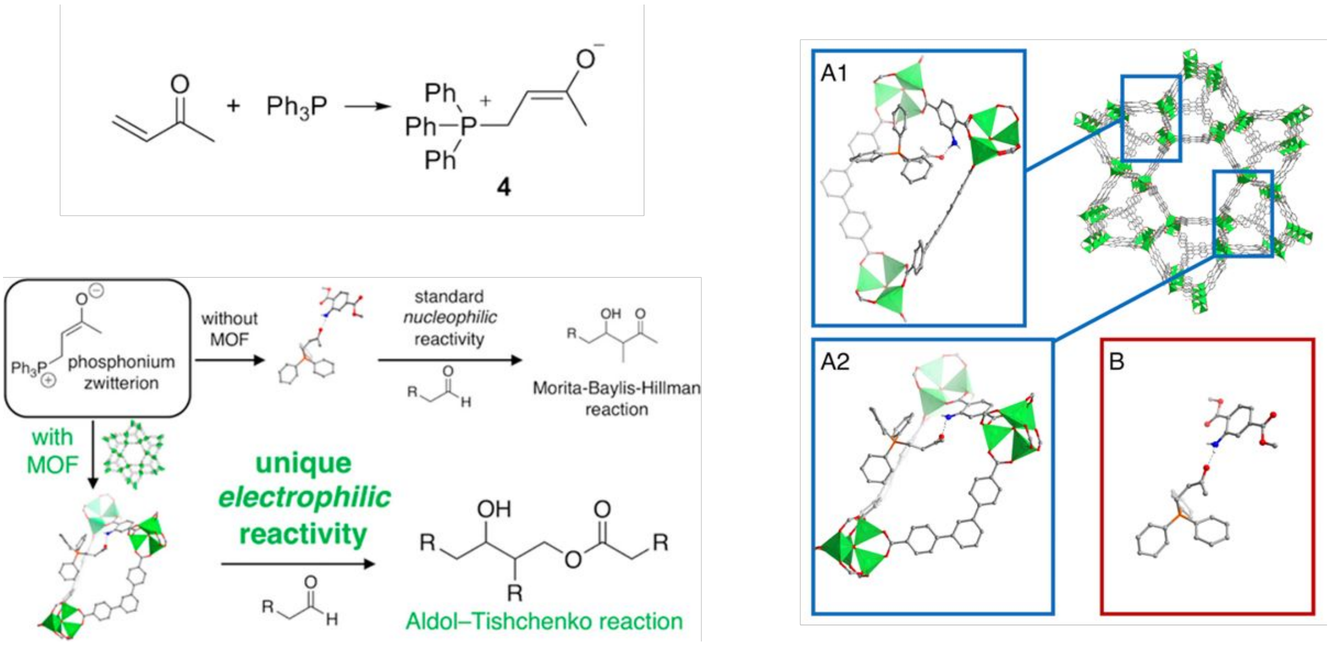

Figure 67. (left) Formation of (3-oxo-2-butenyl)triphenylphosphonium 4 as catalytic active species, and the overall reaction pathways catalysed by zwitterion with and without MOF confinement; (right) Two possible configurations of the zwitterion 4 inside MixUMCM-NH$_2$: 4 being trapped inside the narrow channel (A1) and 4 pointing from the broad channel and into an aperture connecting the channels (A2). Configuration B represents the dimethyl aminoterephthalate system in solution. Adapted with permission from ref. 343. Copyright 2017 American Chemical Society.

more favourable interactions between the pore wall and cyclohexane molecules. Structural modeling illustrated that the changes in extent of cyclohexane adsorption originate from an increase in dihedral angles between the central phenylene unit and its neighbouring rings as the functional group becomes larger (**Figure 66**). In Fe$_2$(dotpdc), adjacent organic linkers create a relatively flat pore surface. As the steric bulk of the functional group increases, the dihedral angles also increase, providing additional van der Waals interactions for cyclohexane binding. Hydrophobic moieties on the channel walls may also induce favourable interactions that funnels the cyclohexane molecules towards the Fe centre. As a result, the local concentration of cyclohexane relative to cyclohexanol is increased, evidently accounting for the observed increases in catalytic conversion and selectivity.

Bauer, *et al.*[343] reported on beneficial interactions between framework linkers and catalyst components (phenyl groups) peripheral to active-sites. Phosphonium zwitterions were deposited onto the amine moieties of MixUMCM-1-NH$_2$ [Zn$_4$I(btb)$_{4/3}$(bdc)$_x$(abdc)$_{1-x}$] (btb = 4, 4’, 4’’,-benzene-1,3,5-trisbenzoate; bdc = 1,4-benzenedicarboxylate; abdc = 2-amino-1,4-benzenedicarboxylate). Phosphonium zwitterions are generally nucleophilic and can catalyse C-C bond-forming reactions such as Michael addition and the Morita-Baylis-Hillman (MBH) reaction. However, when zwitterion **4** [(3-oxo-2-butneyl) triphyenylposhonium] (**Figure 67 left**) was incorporated in MixUMCM-1-NH$_2$, it catalysed electrophilic Aldol-Tishchenko (AT) reactions – catalytic transformations that usually are inaccessible via phosphonium zwitterions. The nature of MOF-guest interactions was investigated via classical molecular dynamics (MD) simulations. Two preferred catalyst sites (**Figure 67** right), **A1** and **A2**, were found. For **A1**, the zwitterion resides in a narrow channel; see **Figure 67**. For **A2**, it resides mainly in a large channel, but with the phosphorous atom residing in an aperture that connects to the narrow channel; see **Figure 67**. The **A2** configuration, imposed by the framework, appears to be responsible for the formation of the AT product. Briefly, strong interactions between zwitterion phenyl groups and the surrounding walls were found. These interactions distort the tetrahedral configuration of the phosphonium moiety, thereby rendering the phosphorous centre more susceptible to electrophilic attack.

Zhang *et al.*[344] exploited cavity-imparted steric limitations within an iridium(III)-functionalized version of UiO-67 to accomplish mono-functionalization of methane using B$_2$Pin$_2$ (bis(pinacolato)diboron). The classic problem with selective activation/functionalization of methane (for example, to form methanol, rather than formaldehyde, formic acid, or CO$_2$) is that the first C-H bond is the most difficult (energetically) to activate. With subsequent C-H bonds being energetically easier to activate, it is challenging to halt functionalization after activating just one C-H bond. UiO-67 features 8 Å apertures and an octahedral cavity of volume 1,100 Å^3 (1.1 nm^3) (as well as a tetrahedral cavity that is too small to participate in the catalytic reaction), see **Figure 68**. In the absence of cavity-confinement of reactants, both mono- and di-borylation of methane are readily feasible, with the doubly-functionalized product being thermodynamically favoured. By requiring methane and B$_2$Pin$_2$ to permeate UiO-67 in order to encounter the iridium catalyst, and by employing dodecane as a solvent to intercept a portion of the activated co-reactant, chemoselectivity for the desired mono-borylated product can be made to exceeds 99%. Computational studies by Truhlar and co-workers further revealed that the overwhelming preference for mono-borylation can be largely understood in terms of how local confinement preferentially attenuates the rate of transport of mono-borylated methane relative to CH_4. Related findings regarding selective mono-borylation, based on Zr-P1-Ir (see **Figure 19** above) have been described by Lin, *et al.*[167]

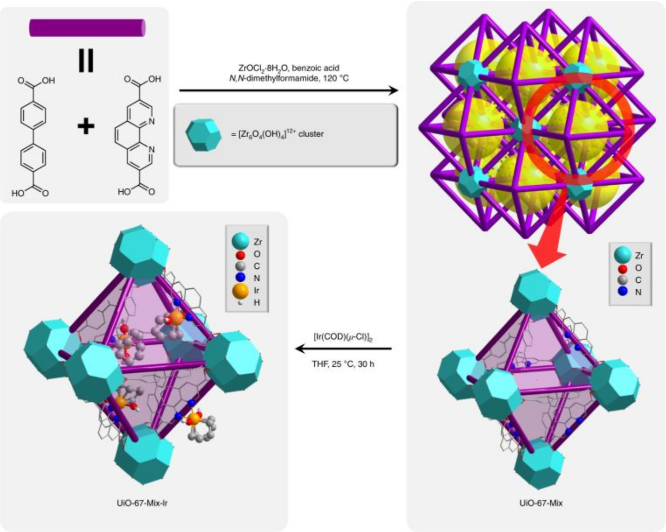

Figure 64. Preparation of UiO-67-Mix-Ir through a mixed-linker synthesis of UiO-67-Mix and the subsequent metalation with an $[Ir(COD)(\mu\text{-}Cl)]_2$ metal precursor. The purple rods and turquoise truncated octahedra represent the linkers and nodes, respectively. The large yellow spheres are a visual indication of the octahedral cavities in UiO-67-Mix. Color: orange, Ir; turquoise, Zr; grey, C; blue, N; red, O, and light-grey, H. Adapted with permission from ref. 344. Copyright 2018 Springer Nature.

Ahn and co-workers[345] showed that tungsten-based polyoxometalate units, sited within the triangular channels of NU-1000 can define a reaction space of roughly 1 nm^3 that is accessible to ortho-xylene as a substrate and that presents highly Lewis acidic protons. The acidity is sufficient to catalyse conversion to other xylene isomers. Much more striking is the conversion of pairs of ortho-xylene molecules to toluene and 1,2,4-trimethylbenzene, a process that requires pairs of catalytic POMs in close proximity, but still sufficiently spaced to allow formation of a diphenylmethane-containing intermediate.

High regioselectivity can also be achieved in MOF catalysts with suitable aperture sizes. For instance, Fan *et al.*[80] synthesized a pentanuclear Co(II)-based MOF $[[Co_5(pmbcd)_2(\mu_3\text{-}OH)_2(H_2O)_4(DMF)_2]\cdot 4DMF]_n$ (H_4pmbdc = 9,9′-(1,4-phenylenebis(methylene))bis(9*H*-carbazole-3,6-dicarboxylic acid) with high regioselectivity for C-H bond oxidation of arylalkanes. In combination with the spatial confinement created by the 8 × 10 Å channels, the well-isolated Lewis acidic sites in this MOF selectively oxidize the most electron-deficient carbon in arylalkanes without over-oxidation, generating mono-ketones as the sole products. In comparison, the homogeneous $CoCl_2$ catalyst with similar Co content could not efficiently catalyse the reaction. CuNPs@NU-901 and CuNPs@NU-907 display differing selectivities for acetylene semi-hydrogenation,[248] where the differences, according to DFT modelling, are related to differences in particle/cluster size and differences in the extents to which various crystal facets are presented.

3.3.3 Enantioselectivity

MOF chirality, combined with pore confinement, can be used to achieve enantioselectivity for heterogeneous catalysis.[346] One strategy is to force the substrate to adopt a preferred conformation within a ligand-defined chiral cavity, in order to access the catalyst active site, a metal centre. Xuan *et al.*[347] adopted such strategy by synthesizing a Ti(salan)-based chiral MOF **1** (**Figure 69**), where Ti(salan) (Ti**L**) comprises a central titanium ion, coordinated by three additional titanium ions, each of which is ligated by a chiral salan ligand that, in turn, is functionalized with a pair of pyridines. Thus, Ti**L** comprises an outward-directed hexadentate MOF building-block. In the MOF environment, each pyridine binds a cadmium ion. These ions, in turn, are chelated by carboxylates from BPDC linkers, as illustrated in **Figure 69**. ("Salan" is the partially oxidized form of the more familiar "salen" ligand architecture.)

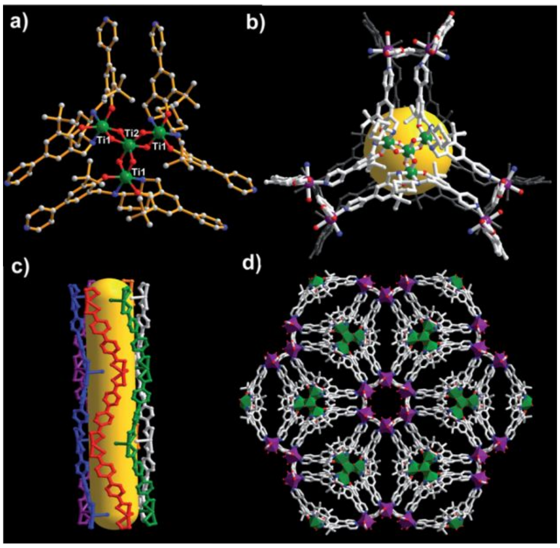

Figure 65. (a) Structural representation of the Ti-cluster in MOF 1. (b) The mesoporous cage encapsulated by two Ti-cluster units. (c) Parallel association of six 1D chains constructed by Cd2+and BPDC. (d) Structure of the MOF viewed along the c-axis. Green = Ti, purple = Cd, blue = N, red = O, gray = C. Adapted with permission from ref. 347. Copyright 2013 Royal Society of Chemistry.

The chemical role of titanium is to facilitate oxygen delivery from hydrogen peroxide. The target reactions are enantioselective oxidations of asymmetric thioethers to yield chiral sulfoxides. The authors observe similar conversions and chemoselectivity for sulfoxide, based on the homogeneous catalyst, Ti**L**, and the MOF version, designated **1.** Enantioselectivities, expressed as ee%, however, are much larger with **1** as the catalyst. Extensive work with metallosalens has shown that chiral salen ligand flexibility is key to achieving high enantiomeric excess in oxidation reactions (for example, conversion of styrene to an asymmetric epoxide). MOF-based immobilization of metallosalens as linkers typically translate to slightly lower enantioselectivities, presumably due to constrained salen-backbone flexibility. Within MOF **1**, however, substrate molecules encounter narrow reaction-pores, each of which is defined by multiple chiral salan ligands that collectively enforce a specific asymmetric substrate conformation.

A simpler strategy, dating back at least to work by Kim *et al.* in 2009,[348] is to decorate MOF pores postsynthetically with chiral functionalities, such as L-proline, oligipeptides, L-tartaric acid, etc.[349-352] While the following example is not appreciably catalytic, **Figure 70** illustrates the idea, in idealized form, for MOF-74-Zn and proline.

A related strategy is to grow, within the MOF pores, chiral polymer chains containing catalytic active sites. The polymer/MOF composite, MIL-101-PP1, was made by impregnating an L-proline-containing vinyl monomer, followed by an *in situ* copolymerization of the monomers and the deprotection of *N*-Boc groups.[353] Immobilization in this way leaves the catalyst active sites (chromium centres) unencumbered by coordinated L-proline. The authors argue that it also allows for favourable movement of prolines in response to substrate presence. MIL-101-PP1 showed enantioselectivity (92% ee) and diastereoselectivity (*anti:syn* = 12:1) for asymmetric aldol reaction superior to both the homogeneous polymer chains (*anti*:*syn* = 1.1:1) and the conventional L-proline-containing cross-linked polystyrene resin CPP1 (41% ee, *anti* : *syn* = 3:1).

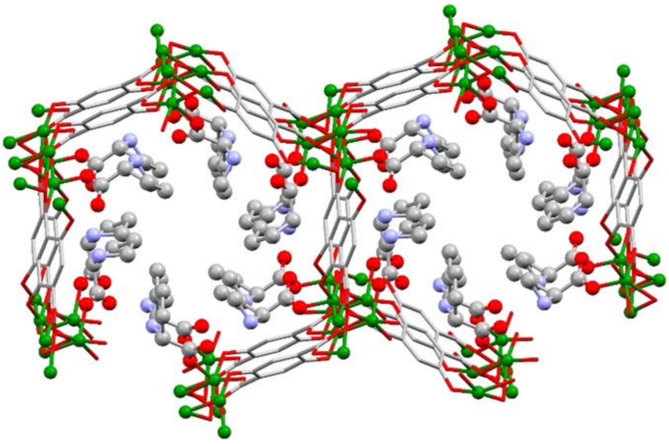

Figure 66. The cell of Zn-MOF-74 fully loaded with proline coordinated in a monodentate manner viewed along the c-axis. Adapted with permission from ref. 352. Copyright 2020 John Wiley and Sons.

4. MOF-Defined Transport Effects Relevant to Catalytic Activity and Selectivity

Molecular transport through MOF pores, whether empty or solvent-filled, typically is diffusive and typically is slower than transport through a corresponding liquid solution or simple gas-phase environment – clear manifestations of nanoscale confinement.[354-355] It is not uncommon for diffusive transport rather than the kinetics of chemical transformations to become the rate-limiting step for MOF-based catalytic reactions. Under these conditions, any mechanistic information one might hope to gain from chemical reaction orders is masked by transport-control of the overall catalytic reaction. Similarly, information about activation energies (based on the temperature dependence of rates of the catalytic chemical reactions) is lost when diffusive molecular-transport is rate-limiting.

Diffusion times increase as the square of the distance traversed. A diagnostic signature of diffusion control, therefore, is a systematic decrease of the overall rate of catalysis with increasing MOF crystallite size (and vice versa). **Figure 71** provides a striking example.[356] The reaction is the Lewis-acid-catalysed hydrolysis of a nerve agent simulant by NU-1000 (PCN-222 and MOF-545 were also examined).

Apart from reducing crystallite dimensions, there are other strategies to enhance diffusive transport through MOFs and potentially boost overall rates of chemical catalysis. First, mesopores are generally better than micropores. Ignoring, for the moment, attractive interactions between diffusing reactants and pore walls, and limiting ourselves to low reactant concentrations, we can expect transport for gas molecules to be governed by Knudson diffusion (reactant collisions with MOF walls) and transport times to vary inversely with pore diameter.[357] For reactants moving through solvent-filled channels, Brownian diffusion (reactant collisions with solvent molecules) is likely to dominate, resulting in transport times that decrease as the square of the pore diameter, greatly favouring mesopores.[358] We also can anticipate shorter transport times if we replace linear diffusion (*i.e.*, 1D diffusion through channels) with radial diffusion (reasonably approximated by equivalent diffusion in the x, y, and z directions).[264, 359] Consequently, both morphology[264] and topology matter[359].

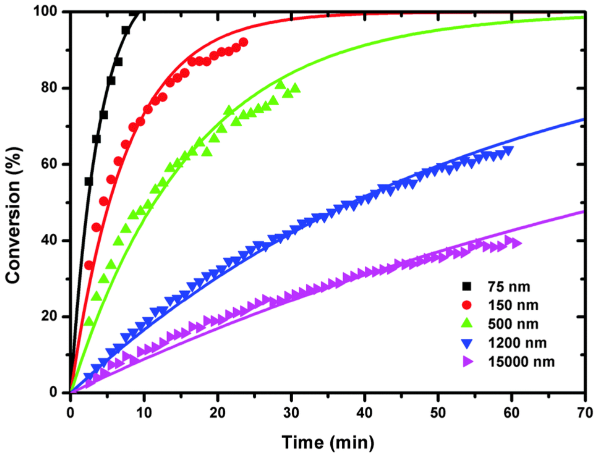

Figure 67. Rates of hydrolysis of methyl paraoxon using NU-1000 nanocrystals with mean sizes ranging from 75 nm (black), 150 nm (red), 500 nm (green), 1200 nm (blue), to 15000 nm (pink). Adapted with permission from ref. 356. Copyright 2015 Royal Society of Chemistry.

In addition, MOF linkers tend to consist of functionalized, conjugated or highly conjugated molecules, featuring significant polarizabilities and therefore significant van der Waals interactions with reactant molecules, especially larger reactants. Indeed, this behaviour has been exploited to extract selected molecules from aqueous solution *via* adsorption onto linkers.[360] Once adsorbed, transport tends to be slow, with movement achieved mainly during interludes of desorption. A curious consequence of reactant adsorption to polarizable linkers is that apparent diffusivities can increase with increase channel loading;[264, 361-362] once high-affinity adsorption sites are largely occupied, subsequently introduced reactants tend to spend greater fractions of their time in mobile, desorbed form. Other considerations are missing-linker type defects, which tend to enhance transport,[363] and crystallite permeation barriers, also called (external) surface resistances.[361] These can be caused, for example, by structural damage to pores at the crystallite perimeter or by partial collapse of channels at their termini.[364] Depending on its magnitude, surface resistance can replace transport diffusion as the rate-limiting step in delivering reactants to internal sites such as catalysts.[365-367]

The notion of hierarchical porosity[368] – interconnected "highways (mesopores)" and "byways (micropores)" – merits consideration. Mesopores can facilitate transport, while micropores can offer confined environments that may engender catalytic selectivity. Conversely, the potentially detrimental consequences of channel-blocking by, say, pore-templated metal nanoparticles or channel-filling enzymes (**see Sections 2.3.4 and 2.3.3**), can be circumvented by connecting to neighbouring pores or channels. Similarly, the local, molecular-scale, consequences of crystallite perimeter damage and resulting surface resistance[366-367] can be partially overcome by reactant entry into the MOF crystallite at undamaged perimeter/terminus sites, followed by cross-cutting diffusion to otherwise functional, end-damaged channels. Examples of topologies leading to hierarchical MOF porosity include **she** and **scu**. Returning to the notion of highways and byways, there is a seemingly paradoxical tendency for medium-sized molecules or condensed molecules (such as water) to seek out micropores over mesopores and, consequently, to move less rapidly through hierarchically porous structures than through strictly mesoporous ones. The tendency stems from dispersion-type interactions between MOF pore walls and guest molecules occupying pores. A guest molecule and pore will experience attractive dispersion interactions only when the only and molecule are in contact or are separated by less than several angstroms. For a molecule that is small in comparison to pore diameter these interactions are significant for only the nearest wall, while larger molecules are subject to attractive interactions from more than one surrounding wall, with the magnified interactions serving to slow the transport of the guest through the pore or channel.[354, 359]

The inherent Lewis acidity of exposed metal-ion nodes can be exploited for MOF-based catalysis of CO_2 cycloaddition reactions.[369-370] Node-binding of an epoxide reactant activates it toward ring opening, which then facilitates insertion of carbon dioxide. Ugale *et al.*[371] chose to target the synthesis of rigid frameworks with a high density of Lewis acid sites (for epoxide activation) together with pores favourable for CO_2 uptake. They synthesized a series of isostructural frameworks composed of Ni^{2+} nodes and both rigid muconate and flexible dipyridyl species as linkers, resulting in 3-fold interpenetrated (catenated) networks (see example in **Figure 72**). Note that while catenation decreases the sizes (capacities) of void spaces, the smaller spaces enable stronger van der Waals interactions with guest molecules (candidate reactants). The investigation of various epoxides as substrates revealed a size effect, with conversion of propylene oxide (1 carbon "chain") reaching 100% under conditions where an epoxide featuring a 10-carbon (linear) chain reaches only 31%. Note that propylene oxide and the 10-carbon (linear) chain epoxide, 2-decyloxirane, present to the 8.25 x 5.45 Å 1D MOF channels essentially identical 2D molecular cross-sections, and present to the Ni^{2+} nodes essentially identically chemically reactive epoxide units. The observed difference in extent of conversion is most likely attributable to channel-containment-accentuated differences in rates of diffusive transport for short versus long reactants.

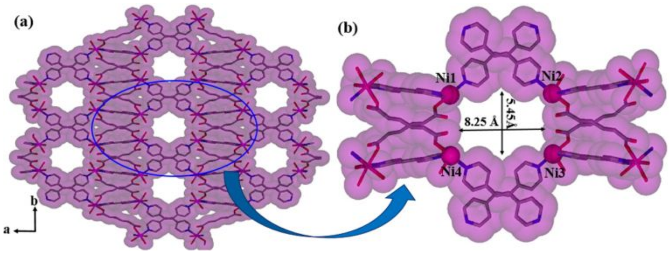

Figure 68. a) Catenated framework view of $[Ni(muco)(bpa)(2H_2O)]•2H_2O$ (bpa = 1,2-bis(4-pyridyl)ethane, muco = trans,trans-muconate) along 1D channels and b) focused view on a single channel showing the four Ni^{II} centres. Carbon (gray), nitrogen (blue), oxygen (red), nickel (magenta). Adopted with permission from ref. 371. Copyright 2016 American Chemical Society.

Note further that activity comparisons based on extent of conversion over a given time (catalysis in batch reactors) or extent of conversion for specific flow conditions (steady-state catalysis in flow reactors) will tend to underestimate intrinsic differences in catalyst efficacy if one of the reactions is run with 100% conversion. Without further information, we cannot say whether a given decrease in the rate of the rate-limiting step will suffice to drop conversion detectably below 100%. Thus, the observed *ca.* 3:1 ratio of extents of conversion for propylene oxide vs. 2-decyloxirane (**Figure 72**) could be indicative of a substantially greater than 3-fold difference in rate-limiting epoxide diffusivity.

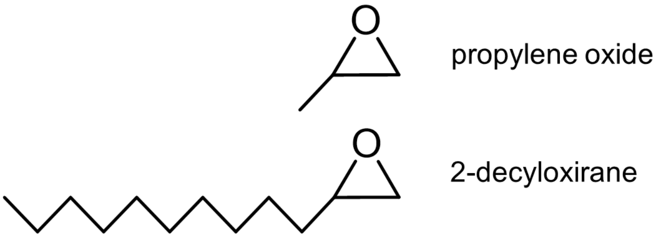

Figure 69. Small and big-size epoxides catalysed by MOF catalysts.

Li, *et al.*[372] described a similar study and similar results for a tetra-triazole-containing linker that, together with carboxylate-coordinated (paddlewheel-coordinated) pairs of Cu(II) ions, define a microporous MOF. Open Cu(II) sites (axial sites) on the node can act as active sites for epoxide-based CO_2 fixation. Changing the liquid substrate from neat propylene oxide to neat 2-decyloxirane leads to a 20-fold decrease in reaction yield, *i.e.* a decrease from 96% to 5%. Although the findings were interpreted in terms of substrate selectivity and a small vs. large size-exclusion effect, the substrates present nearly identical kinetic diameters, strongly suggesting that the observed differences are instead transport based (**Figure 73**). A 20-fold difference in molecular diffusivities could account for the observations. If correct, then the single-component reactivity

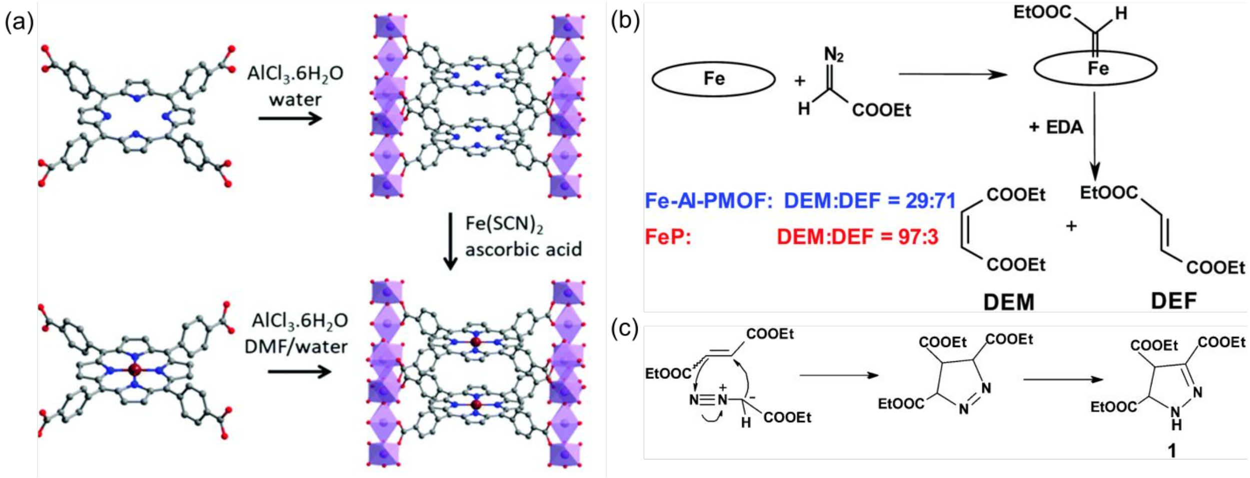

Figure 70. (a) Post synthesis metalation (PSM) and direct synthesis routes for synthesizing the Fe–Al-PMOF. Color: red, oxygen; blue, nitrogen; grey, carbon; purple, aluminum; brown, iron. (b) Formation of a carbene complex from EDA and FeP/Fe–Al-PMOFs and its further reaction with EDA to form DEM and DEF. (c) Cycloaddition of EDA to diethyl maleate and diethyl fumarate. Adapted with permission from ref. 375. Copyright 2018 Royal Society of Chemistry.

differences are unlikely to translate into selectivities of similar magnitude for mixtures of neat reactants.

Wang *et al.*[373] used an Ir(III)-porphyrin-MOF with Hf nodes, Ir-PMOF-**1**(Hf), to catalyse carbenoid insertion into an Si-H bond. (PMOF-**1** is also known as PCN-224[374]) In the absence of a coordination framework, insertion into a tertiary Si-H bond is generally favoured over other Si-H bonds due to a lower activation barrier for reaction of the former. With Ir-PMOF-**1**(Hf) as the catalyst, the reactivity is inverted, *i.e.* primary > secondary > tertiary. Competition experiments reveal that the ordering is retained when multiple candidate reactants are present. Multiple explanations are presented, but the most compelling is that MOF apertures slow transport of species featuring tertiary S-H bonds to a greater extent than those with secondary Si-H bonds, with both being slowed more than species featuring primary Si-H bonds. Thus, MOF permeation and/or intracrystalline transport, rather than carbenoid insertion, is likely the rate-limiting process. Not explored was the extent to which the ordering of activity is retained, under competitive conditions, as the reactant concentrations are increased. One might expect the ordering to reverse at high mixture concentrations, as the dispersion-based affinity of the framework for reactants should be greatest for tertiary species and smallest for primary ones. Thus, at high mixture concentrations, tertiary species may crowd-out secondary and primary ones.

Abeykoon, *et al.*[375] installed a carbene precursor, ethyl diazoacetate (EDA), onto the Fe centres of an iron-porphyrin based MOF; see **Figure 74a.** In the absence of a framework, Fe-carbene complexes can react with free EDA to form both diethyl maleate (DEM, *cis*-isomer) and diethyl fumarate (DEF, *trans*-isomer); see **Figure 74b**. The initial motivation for the MOF-based study was to demonstrate an anticipated confinement-derived selectivity for DEM over DEF. Unexpectedly observed instead was the formation and isolation primarily of, 3,4,5-triethyl-4,5-dihydro-1*H*-pyrazole-3,4,5-tricarboxylate (**1**) as the reactant product; see **Figure 74c**. Notably, this product is nearly absent from reactions catalysed by the homogeneous complex. Mechanistic studies showed that **1** is formed after the generation of DEM and DEF, *via* a 1,3-dipolar cycloaddition of the diazo moiety on EDA to the C=C bond of DEM or DEF, where the follow-on reaction is favoured by temporarily confining DEM or DEF within the MOF, such that further reactive encounters with Fe-porphyrin active-sites can occur, prior to exiting of DEM or DEF from the porous framework. Thus, the role of the framework is both to slow the transport of intermediate species and to expose the intermediates to additional active-sites ahead of product egress.

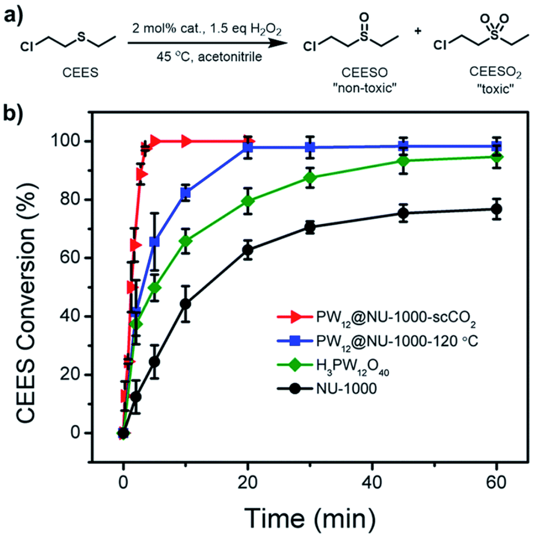

Figure 71. (a) Scheme of the reaction pathway for the oxidation of CEES to CEESO and $CEESO_2$; (b) Reaction conversion vs. time by using the catalysts of NU-1000, $H_3PW_{12}O_{40}$, PW_{12}@NU-1000-120 °C, and PW_{12}@NU-1000-scCO_2. Adopted with permission from ref. 172. Copyright 2018 Royal Society of Chemistry.

A supercritical-CO_2-treated POM@NU-1000 material catalytically engendered a faster rate (half-life of 1 min) for partial oxidation of CEES (a mustard gas simulant) by hydrogen peroxide and higher product selectivity (90 ± 5%) than did the same material activated under vacuum at 120 °C (half-life of 3 min; product selectivity of 59 ± 7%); see **Figure 75**. The salient structural difference is the siting of the POM.[172] Supercritical activation leaves the installed POM in the MOF's mesopore – a kinetic site. Heating enables the POM to transit to a micropore – a thermodynamically favoured location; see **Figure 23**. The basis for differences in catalytic activity and selectivity is unclear, but it is tempting to assign it to transport-dominated differences in site accessibility.

5. MOF-Enabled Combining of Complementary Catalysts

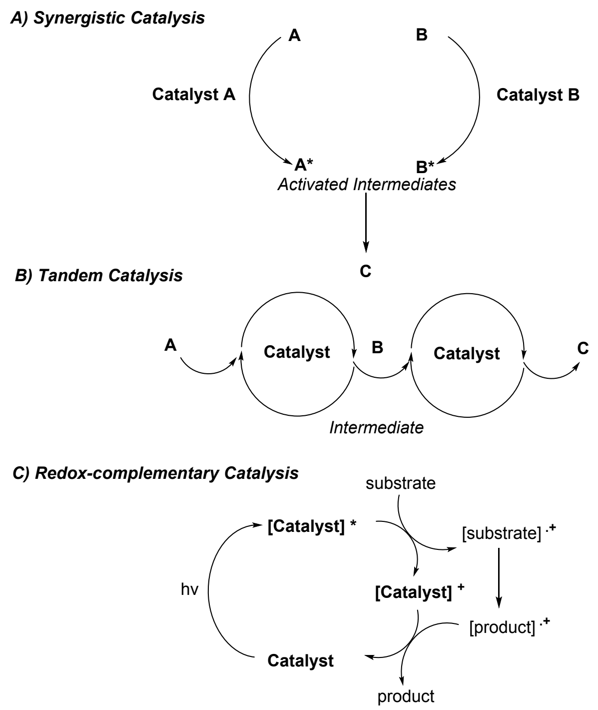

Figure 72. Synergistic catalysis, tandem catalysis, and redox-complementary catalysis.

Synergistic catalysts feature multiple active sites or reactive components that cooperatively facilitate a single chemical transformation by providing needed complementary pairs of activated reactants or chemical intermediates Scheme A in **Figure 76**).[376-377] The behaviour is synergistic if the resulting activities of catalytic components of the whole outweigh those expected if contributing entities operate independently.[378] Active-site tunability together with containment, confinement, and protective isolation within MOFs have enabled the development of such synergistic catalysts as discussed in recent reviews and work.[379-388] In this section, we will highlight work that reports unique selectivity or elucidates helpful structure-property relationships using the confinement of multiple active sites in a MOF-based synergistic catalyst.

The presence of reactive moieties on MOF structural elements (*i.e.*, node and linker) allows for anchoring additional species to tune the surface chemistry.[96, 389] Lin and Wang *et al.*[390] used a mixed-linker strategy (variant of **Figure 16**) to immobilize a Ru chromophore in UiO-67; the simultaneous addition of $[Ru^{II}(BPY)_2(H_2BPYDC)]Cl_2$ (BPY = 2,2′-bipyridine; H_2BPYDC = 2,2′-bipyridine-5,5′-dicarboxylic acid) and biphenyl-4,4′-dicarboxylic acid (H_2BPDC) in the presence of $ZrCl_4$ yields Ru-UiO-67. Given the ease of one-reduction of Cu^{II} by photo-excited tris-(2,2′-bipyridine)$_3$, and given the known effectiveness of copper as a component of catalysts for CO_2 hydrogenation, the authors successively infiltrated Ru-UiO a copper salt and then with 0.1 M NaH_2PO_4/Na_2HPO_4 to obtain $Cu^{II}(H_xPO_4)_y$@Ru-UiO; see **Figure 77**. LED-based irradiation near the absorption maximum of the ruthenium species (λ = 450 nm) served to activate the catalyst. Subsequent exposure of the catalyst to a mixture of 3:1 H_2 and CO_2 , at *ca.* 20 bar, for 24 hours at 150 °C, led initially exclusively to EtOH as a reaction product. The turnover number on a per-copper-atom basis was 15**.** Prolonged catalysis, resulting in some conversion of Cu(I) to Cu(0), was eventually accompanied by production of methanol in addition to ethanol. EtOH selectivity could be restored, however, by re-irradiating the initial activity appears to be contingent upon $Ru^{II}(BPY)_2(BPYDC)$-facilitated conversion of Cu(II) to catalytically active and chemoselective Cu(I). Restoration of chemoselectivity appears to be associated with $Ru^{II}(BPY)_2(BPYDC)$-facilitated conversion of Cu(0) back to Cu(I).

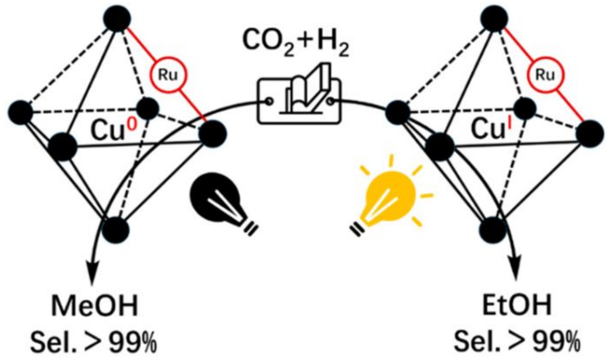

Figure 73. Synergistic catalysis systems utilizing electron transfer between $[Ru(bpy)_3]^{2+}$-based ligands and Cu species for selective CO_2 hydrogenation. Adopted with permission from ref. 390. Copyright 2020 American Chemical Society.

Remarkably, in the absence of photo-activation, copper-phosphate-containing Ru-UiO-67 is >99% selective for MeOH, rather than EtOH. Key to the altered chemoselectivity appears to be involvement of nanoparticulate Cu(0) as the catalytically active moiety, rather than a Cu(I)-phosphate complex. The authors suggest that the incorporated phosphate ligands function as bases and facilitate the generation of a formyl intermediate for EtOH synthesis. After catalysis, XPS and Auger electron spectroscopy (AES) measurements established that irradiated samples, that yield EtOH, contain Cu(I), while non-irradiated samples that catalyse methanol formation, contain Cu(0) nanoparticles.

An unusual example of synergistic effects has been reported Lee, *et al.*[391] wherein Al^{3+} isolated as the node of for MIL-53(Al) deposited on an electrode of aluminum foil, wherein the assembly functions as an electrocatalyst carbon dioxide reduction to carbon monoxide and formic acid, while suppressing H_2 – a problematic competing reaction, and one that is observable with bare aluminum foil (which itself is inactive for CO_2 reduction). The findings are puzzling, given the extraordinary thermodynamic and kinetic difficulty of reducing Al^{3+}. Coordinated benzene dicarboxylate, the linker for MIL-53, see **Figure 7**, is similar resistant to electrochemical reduction. Thus, a redox-mediated catalytic cycle seems unlikely. Ultrathin films of alumina are known to suppress electrochemical hydrogen evolution, while permitting electrons to tunnel through the oxy, hydroxy film and reach electron acceptors on the solution-side of the electrochemical interface (albeit, with significant rate attenuation compared to film-free electrodes).[392] MIL-53(Al) is known to interact with CO_2[393] and to degrade in aqueous bicarbonate.[394] It is tempting to conclude that the role of MIL-53(Al) and/or its degradation products is to bind and activate CO_2 or bicarbonate in non-redox fashion, such that the activated species occupying sites nearest the electrode interface are susceptible to direct electrochemical reduction.

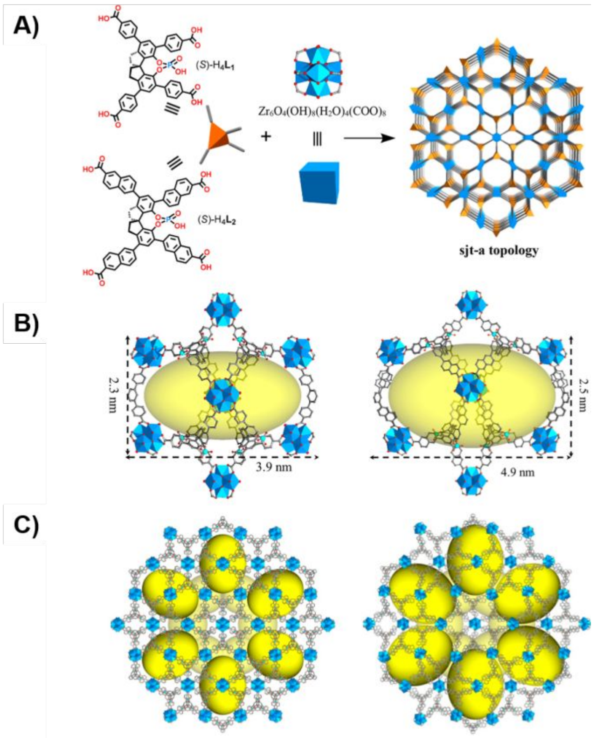

Figure 74. A) Scheme of the preparation of Spiro-1 and Spiro-2 from the Zr_6 clusters linked by H4L1 and H4L2 respectively. (B) Resulting hexagonal bipyramidal cages present in the framework. (C) 3D porous architectures in Spiro-1 (left) and Spiro-2 (right) as viewed along the c-axis. Yellow ellipsoids represent the cavities, and H atoms are omitted for clarity. Adapted with permission from Ref. 405. Copyright 2019 American Chemical Society.

Sometimes referred to as “cascade” or “domino” reactions, tandem catalysis describes a one-pot methodology in which two or more independent, successive reactions yield a final product, without purifying or isolating any intermediate products (**Scheme B in Figure 76**).[395-396] An obvious virtue of this approach is that short-lived intermediates can be captured by proximal second- or third-step catalysts and converted to desired products. While a single active-site can sometimes catalyse successive reactions,[397] often two or more active sites are required.[398] We will highlight recent work in which proximally confining or siting complementary active-sites within MOFs leads to superior, tandem catalytic activity.

Metal cation components of reactant-accessible MOF nodes are inherently Lewis acidic, as are post-synthetically grafted metal ions.[399-400] Often, thermal treatment is needed to remove charge-neutral, nonstructural ligands and expose acidic sites.[401-403] Many nodes also present, in the form of hydroxo or aqua ligands, Brønsted acid sites.[195, 404] These sites, however, are typically only moderately acidic. Much more highly acidic sites can be presented by embedding phosphate moieties, either directly on nodes or as accessible components of linkers. A compelling example has been described by Liu, *et al.*[405] Briefly, they constructed a series of MOFs using chiral, acid-phosphate-containing, linkers – specifically, (4,4′,6,6′-tetra(benzoate) and -tetra(2-naphthoate) derivatives of 1,1′-spirobiindane-7,7′-phosphoric acid) (SPINOL) – together with Zr_6 nodes, forming Sprio-1 and Sprio-2 respectively (**Figure 78**). Interestingly, the authors observed significant increases in the Brønsted acidity of the phosphoric acid on the SPINOL-based linkers after incorporation in frameworks. They attributed the increases to electron-withdrawing effects transmitted from node-based Zr(IV) ions and through the SPINOL backbone, and to elimination of solution-phase SPINOL-SPINOL hydrogen bonding. The parallel presence of accessible Lewis and Brønsted acid sites in the new MOFs was exploited for catalysis of chemical transformations two, or even three, reactions (*i.e.*, acetalization, Friedel–Crafts, iso-Pictet-Spengler, and Friedel–Crafts reactions). They further observed that framework organization and compartmentalization of catalyst active-sites translated to much higher enantioselectivivities (*i.e.*, 75 – 97%, for deacetalization–acetalization of 2-aminobenzamide with dimethyl acetals containing arylaldehydes) than obtained with linkers as homogeneous solution catalysts. Mechanistic studies showed that Zr(IV) sites (Lewis acidic sites) catalyse the deacetalization of aldehyde dimethyl acetals and cyclic acetals to aldehydes, with Bronsted-acidic phosphate moieties catalysing subsequent acetalization and reaction completion.

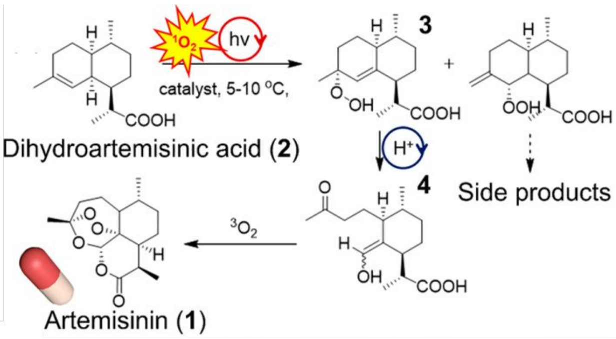

Figure 75. Scheme of tandem semisynthesis of artemisinin by PCN-222-SO_4. Adapted with permission from Ref. 406. Copyright 2019 American Chemical Society.

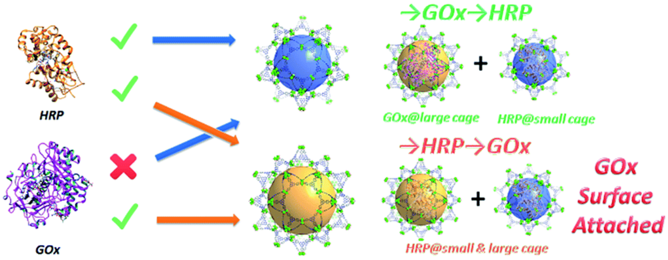

Figure 76. Schematic presentation of incorporation of two enzymatic guests (GO_x and HRP) into the largest and intermediate cages in PCN-888. Adapted with permission from Ref. 411. Copyright 2016 Royal Society of Chemistry.

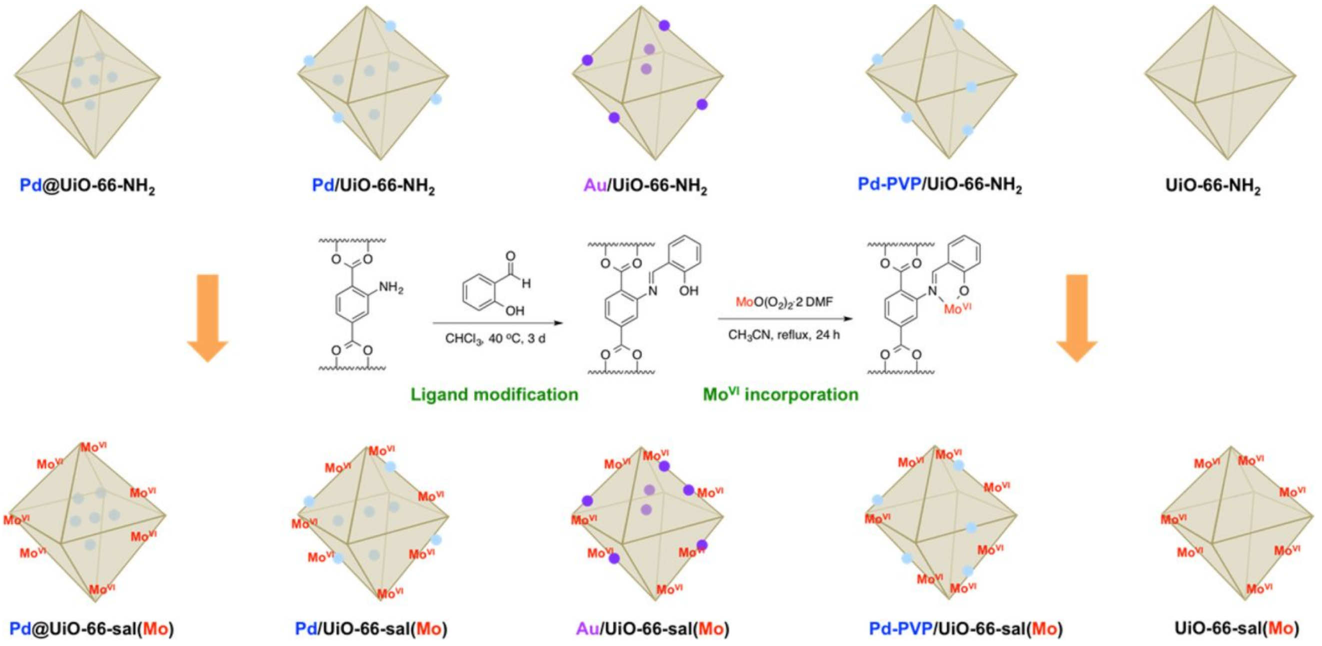

Figure 77. Visual representation and schematic of catalysts investigated for tandem alkene oxidation. Adapted with permission from Ref. 412. Copyright 2017 American Chemical Society.

Zhou *et al.*[406] used post-synthetic modifications to generate PCN-22X-SO_4 (X = 2, 3, 4), which were then deployed for the tandem semisynthesis to make artemisinin, an antimalarial drug.[407] Yaghi, Klemperer, and co-workers,[298] previously had shown for MOF-808-SO_4 that H_0 values as extreme as -14 could be obtained, *i.e.* borderline super-acidity. In the presence of the photo-active porphyrin-based linkers that generate singlet oxygen, the sulfated sites at the MOF first converted dihydroartemisinic acid to a peroxide intermediate through a $^1O_2$ ene reaction (**Figure 79**). Then, the same acidic sites catalysed a Hock cleavage and a cascading cyclization to yield the final product of artemisinin. The mesoporous PCN-222(Ni)-SO_4 achieved a nearly quantitative conversion and a product yield of 71%. Notably, sulfate-free PCN-222 can generate the peroxide intermediate but fails to facilitate the acid-catalysed reaction, highlighting the need for the dual site catalyst in the tandem reaction.

Elaboration/occupation of cavity of a catalytically functional MOF cavity with a second catalytically active moiety, such as a nanoparticle or enzymes, is another strategy for engendering tandem catalysts. Recent advances in accessing mesoporous MOFs have broadened the collection of MOFs capable directly encapsulating large guests.[408-410] For example, Zhou, *et al.*[411] synthesized PCN-888, composed of an Al trimer linked by a heptazine based tritopic ligand, which features of 6.2, 5.0, and 2.0 nm diameter cavities. Following sequential exposure to two enzymatic guests, the largest cavity accommodated one molecule of glucose oxidase (GOx) while 1 molecule of horseradish peroxidase (HRP) fit inside the intermediate cage, forming PCN-888-en as illustrated in **Figure 80**.

The smallest cage remained open to allow for possible substrate diffusion. In the presence of glucose and O_2, GOx in PCN-888-enR produces H_2O_2 which is readily consumed in the presence of HRP to convert 2,2'-azino-bis(3-ethylbenzthiazoline-6-sulfonic acid) (ABTS) to $ABTS^{\cdot +}$. The initial catalytic rate of PCN-888-en, 2.4 × 10^4 s^{-1}, is slightly less active the free enzymes in solution, for which the initial rate is 7 × 10^4 s^{-1}. Notably, however, the MOF protects the encapsulated enzymes from trypsin digestion. Moreover, the enzymes show minimal leaching from the MOFs during and after catalysis.

Nguyen, Tsung, and co-workers[412] incorporated Pd nanoparticles in UiO-66-NH_2 and then post-synthetically attached to linkers (sal)Mo^{VI} (sal = salicylaldimine) for molecular epoxidation catalysis (**Figure 81**). The metal NPs catalysed the production of H_2O_2 in the presence of H_2 and O_2 (a combination that, because of extreme explosion hazard, should be explored only under well-defined limiting conditions and with explosion-containment equipment). The generated H_2O_2 was then used by linker-immobilized Mo catalysts for epoxidation of *cis*-cyclooctene. The NP-generated H_2O_2 is apparently fairly long-lived, as the activity integrated catalyst pair is only about 45% higher than observed for a physical mixture of Pd@UiO-66-NH_2 + UiO-66-sal(Mo).

6. Conclusions and Looking Forward

It is clear that MOF-based nanoconfinement, containment of catalysts and molecular reactants, intermediates, and products can be channelled, at least at the proof-of-concept level, to do certain things remarkably well. Among them are: i) reactant size and, to a lesser extent, shape selection for encounters with catalysts, ii) stabilization of catalysts, iii) replication of known enantioselective behaviour of molecular catalysts, and iv) enhancement of catalytic activity based on reactant pre-concentration. It is more challenging to forecast where the sub-field might go next. But, we think the following might be areas of high opportunity and significance.

Understanding and controlling catalytic chemistry via the environment beyond the active site. If we omit chiral frameworks, only a handful of published studies offer atomically precise pictures of the environment immediately proximal to, but clearly beyond the catalyst active-site. From structural studies of enzymes, however, we know that the structure and composition of this environment can be exceptionally important in eliciting desired catalytic behaviour. As the environment around active-sites in enzymes typically comprises sequences of amino acids, it is conceivable that installation of oligopeptides, in controlled fashion, in MOF pores could similarly enable catalysis – especially if the reactions to be catalysed entail proton delivery or removal by weak acids or bases. Although directed mainly at problems other than catalysis, a handful of reports on controlled oligopeptide installation in MOFs (or construction of MOFs) exists.[413-417] Other obvious candidate components of environments beyond the active-site are solvent molecules and free charge-compensating ions. Confinement can constrain solvent molecules and ions sufficiently for their locations to be pinpointed.[250, 403, 418-423] One recent example reports the positions of > 40 water molecules within a MOF pore. This level of structural characterization has the potential to greatly enhance the power of predictive computational chemistry.

Understanding and controlling the evolution of catalyst active-sites. Catalysts inevitably change over time, even if only to become inactive. Although only a few examples have been published,[114] it is clear that selected catalysts can be removed from reactors mid-run and interrogated by conventional single crystal X-ray crystallography, with the resulting data offering atomically precise structural insights into the causes for changes in catalytic activity or selectivity. Similarly, one could envision characterizing the conversion of pre-catalysts to active-catalysts, or active-catalysts to expired and inactive catalysts.[247] Together with *operando* structural studies, these experiments could offer the insights needed to define and control the evolution of MOF-supported catalysts. It is worth noting that successful SCXRD studies require not only short-range structural uniformity, but also periodicity. Frameworks that support three-dimensional arrays of catalysts offer the possibility for satisfying these requirements.

Cascade catalysis with chemically incompatible catalysts. Siting complementary catalysts within nanometres of each other offers the possibility of making efficient use of chemical intermediates having sub-microsecond lifetimes, thereby opening-up new catalytic sequences for chemical transformations. An intriguing next step would be to site chemically incompatible, but catalytically complementary, moieties within angstroms of each other, with a MOF providing the degree of immobilization needed to prevent catalyst/catalyst annihilation. More generally, MOF-choreographed cascade catalysis offers the possibility of eliminating intermediate workup, isolation, and purification from many-step reactions.[424]

Pre-formed intermediate building blocks. As atomically precise MOF-supported catalysts become more functional and more complex, stepwise build-up of catalytic clusters becomes less and less viable and reliable, if the goal is complete uniformity of catalyst structures within a given framework. Pre-formed intermediate moieties – most obviously, structurally well-defined polyoxometalates, but also others – will increasingly become catalyst building blocks or precursors of choice.

Access to unprecedented catalysis mechanisms via unprecedented active-site coordination. Known MOF-based catalytic chemistry, for the most part, has mechanistic precedents in the chemistry of molecular catalysts or conventional heterogeneous catalysts. Appending catalytic metal ions or clusters to single, nonstructural ligands that offer both charge-compensation and minimal coordination, opens up, after removal of free- and ligated-solvent, the possibility of accessing stable metal ions having uniquely low coordination numbers and, therefore, a surfeit of reactant and co-reactant binding sites. It is not unreasonable to imagine coordination numbers of one, two, or three (even for ions of transition metals other than silver or gold) – akin to what can be formed transiently in the gas phase and observed by mass spectrometry. It is also not unreasonable to imagine dosing low-coordination-number metal cations with controlled numbers of auxiliary ligands, again enabling otherwise inaccessible coordination spheres to be obtained.

Finally, in selecting papers for highlighting we have necessarily omitted other clearly relevant papers, including papers by groups led by Rahul Banerjee,[425] Avelino Corma,[426-430] Zhengping Dong,[431] Mohamed Eddaoudi,[432] Roland A. Fischer,[277, 433-434], Jorge Gascon,[435-437] Stefan Kaskel,[438-439] Hiroshi Kitagawa,[440-441] Susumu Kitagawa,[442] Jeffery Long,[443] Ali Morsali,[254, 444-445] Matthew Rosseinsky,[446] Berend Smit,[447-448] Norbert Stock,[449-452] Shane G. Telfer,[453-455] Fernando Uribe-Romo,[456] and Michael Zaworotko.[457] We refer interested readers to the cited papers.

This journal is © The Royal Society of Chemistry 20xx

Table 1. Abbreviations

(d)PDF	(differential) pair distribution function
1D	1-dimensional
2D	2-dimensional
3D	3-dimensional
4,4’-bpydc	4,4’-dicarboxylate-2,2’-biyridine
ABDC	2-amino-1,4-benzenedicarboxylate
ABTS	2,2'-azino-bis(3-ethylbenzthiazoline-6-sulfonic acid)
AES	Auger electron spectroscopy
AIBN	2,2’-azobis(isobutyronitrile)
AIM	atomic layer deposition in MOFs
ALD	atomic layer deposition
AT	Aldol-Tishchenko
B_2pin_2	bis(pinacolato)diboron
BAS	Brønsted acid site
BPA	1,2-bis(4-pyridyl)ethane
BPY	2,2’-bipyridine
CAL	cinnamaldehyde
CD	cyclodextrin
CEES	2-chloroethyl ethyl sulfide
COD	1,5-cyclooctadiene
COF	covalent organic framework
COMOC	Center for Ordered Materials, Organometallics and Catalysis
Cp*	pentamethylcyclopentadiene
CpI	Clostridium pasteurianum
Cyt-c	cytochrome-c
DABCO	1, 4-diazabicyclo [2.2. 2] octane (also denoted triethylendiamine, TED, or TEDA)
DED	difference envelope density
DEF	diethyl fumarate
DEM	diethyl maleate
DFT	density functional theory
DMF	*N,N*-dimethylformamide
DMNP	dimethyl 4-nitrophenyl phosphate
DRIFTS	diffuse reflectance infrared Fourier transform spectroscopy
DUT	Dresden University of Technology
DVB	divinylbenzene
EDA	ethyl diazoacetate
EDS	energy dispersive X-ray spectroscopy
EPR	electron paramagnetic resonance
EXAFS	extended X-ray absorption fine structure
FT	Fourier transform
GOx	glucose oxidase
H_2BDC	1,4-benzenedicarobxylic acid
H_2BPDC	biphenyl-4,4’-dicarboxylic acid
H_2BPYDC	2,2′-bipyridine-5,5′-dicarboxylic acid
H_3BTB	4, 4’, 4’’-benzene-1,3,5-trisbenzoic acid
H_3BTC/H_3TMA	1,3,5-benzenetricarboxylic acid; 1,3,5-trimesic acid
H_2BTDD	bis(1*H*-1,2,3-triazolo[4,5-*b*],[4′,5′-*i*])dibenzo[1,4] dioxin
H_2TCPP	tetrakis(*p*-carboxyphenyl)porphyrin
H_4DOBPDC	4,4′-dihydroxy-[1,1′-biphenyl]-3,3′-dicarboxylic acid
H_2DOTPDC	4,4″-dihydroxy-[1,1′:4′,1″-terphenyl]-3,3″-dicarboxylic acid
H_4PMBDC	9,9’-(1,4-phenylenebis(methylene))bis(9H-carbazole-3,6-dicarboxylic acid
H_4TBAPy	1,3,6,8-tetrakis(p-benzoic acid)pyrene
H_4TPP	5,10,15,20-tetra(1H-pyrazol-4-yl)porphyrin
HAADF-STEM	high angle annular dark field - scanning transmission electron microscopy
HER	hydrogen evolution reaction
HKUST	Hong Kong University of Science and Technology
HNTM	MOF hollow nanotubes
HRP	horseradish peroxidase
HRTEM	high-resolution transmission electron microscopy
IPr	1,3-bis(2,6-diisopropylphenyl)imidazole-2-ylidene
IRMOF	Isoreticular MOF
KLASCC	Key Laboratory of Applied Surface and Colloid Chemistry
LED	light emitting diode
MBH	Morita-Baylis-Hillman
MCM	Mobil Composition of Matter
MCP	methylcyclopentane
MD	molecular dynamics

Me$_3$mpba	*N, N′*-2,4,6-trimethyl-1,3-phenylenebis(oxamate)
Me-TTFTB	tetrathiafulvalene tetramethylbenzoate
MFI	Mobil Five
MIL	Materials from Institut Lavoisier
MMPF	metal–metalloporphyrin framework
MOF	metal–organic framework
MOP	metal–organic polyhedron
MP-11	microperoxidase-11
MUCO	*trans,trans*-muconate
NADH	nicotinadmide adenine dinucleotide
NAI	*N*-acetylimidazole
NDC	2,6-naphthalene dicarboxylate
NMR	nuclear magnetic resonance
NP	nanoparticle
NU	Northwestern University
ODH	oxidative dehydrogenation
PC	pyridylcarbinol
PCBA	[6,6]-phenyl-C$_{61}$-butyric acid
PCN	porous coordination network
PCy$_3$	tri-cyclohexyl-phosphine
PIP	polyisoprene
PMOF	porphyrin MOF
POM	polyoxometalate
POMOF	POM-based MOF
PSD	post-synthetic deprotection
PSE	post-synthetic exchange
PSS	polystyrenesulfonate
PTA	phosphotungstic acid
PVP	polyvinylpyrrolidone
PXRD	powder X-ray diffraction
py3tren	*N,N,N*-tris(2-(2-pyridylamino)ethyl)amine
ROS	reactive oxygen species
SAL	salicylaldimide
SALE	solvent-assisted linker exchange
SALEM	Solvent-Assisted Linker Exchanged Material
SALI	solvent-assisted ligand incorporation
SBA	Santa Barbara Amorphous
SBU	secondary building unit
SCXRD	single-crystal X-ray diffraction
SEM	scanning electron microscopy
SIM	solvothermal installation in MOFs
sMMO	soluble methane monooxygenase
SPINOL	1,1′-spirobiindane-7,7′-phosphoric acid
STEM	scanning transmission electron microscopy
TBPB	1,1′-spirobiindane-7,7′-phosphoric acid
TBHP	*tert*-butyl hydroperoxide
^{tBu}PNP	2,6-bis((di-tert-butyl-phosphino)methyl)pyridine
TDC	thiophene dicarboxylate
TEM	transmission electron microscopy
TFA	trifluoroacetic acid
TFPM	tetrakis(4-formylphenyl)methane
TMBQ	2,3,5-trimethylbenzoquinone
TMHQ	2,3,5-trimethylhydroquinone
TOF	turnover frequency
TON	turnover number
TPD	temperature programmed desorption
TpmC*	1,1′,1′′-methanetriyltris(3,5-dimethyl-1H-pyrazole-4-carboxylic acid)
TTFTB	tetrathiafulvalene tetrabenzoate
UiO	University of Oslo
UMCM	University of Michigan Crystalline Material
UV	Ultraviolet
XANES	X-ray absorption near edge structure
XAS	X-ray absorption spectroscopy
XPS	X-ray photoelectron spectroscopy
ZIF	zeolitic imidazolate framework
ZSM	Zeolite Socony Mobil

Table 2. MOFkey and MOFid Identifiers.

MOF Name	MOFkey	MOFid
bio-MOF-100	Zn.NEQFBGHQPUXOFH.XLTORTMOVVGLEX.MOFkey-v1.UNKNOWN	Nc1ncnc2c1N=C[N]2.[O]C(=O)c1ccc(cc1)c1ccc(cc1)C(=O)[O].[Zn].[Zn]O[Zn] MOFid-v1.UNKNOWN.cat0
$[[Co_5(pmbcd)_2(\mu_3\text{-}OH)_2(H_2O)_4(DMF)_2]\cdot 4DMF]_n$	Co.OTOWENYGAXDLLK.MOFkey-v1.UNKNOWN	[Co][OH]1[Co]([OH2])[OH2][Co]21[OH2][Co]([OH]2[Co])[OH2].[O-]C(=O)c1ccc2c(c1)c1cc(ccc1n2Cc1ccc(cc1)Cn1c2ccc(cc2c2c1ccc(c2)C(=O)[O-])C(=O)[O-])C(=O)[O-] MOFid-v1.UNKNOWN.cat0
Cu-BTC / HKUST-1 / MOF-199	Cu.QMKYBPDZANOJGF.MOFkey-v1.tbo	[O-]C(=O)c1cc(cc(c1)C(=O)[O-])C(=O)[O-].[O][Cu][Cu][O] MOFid-v1.tbo.cat0
DUT-67	Zr.YCGAZNXXGKTASZ.MOFkey-v1.reo	[O]C(=O)c1ccc(s1)C(=O)[O].[O][Zr]123([O])[O]4[Zr]56[O]3[Zr]37([O]2[Zr]28[O]1[Zr]14([O]6[Zr]([O]53)([O]21)([O]78)([O])[O])([O])[O])([O])[O] MOFid-v1.reo.cat0
IRMOF-10	Zn.NEQFBGHQPUXOFH.MOFkey-v1.pcu	[O-]C(═O)c1ccc(cc1)c1ccc(cc1)C(═O)[O-].[Zn][O]([Zn])([Zn])[Zn] MOFid-v1.pcu.cat0
MFU-4	Zn.PMBZGVXPOQXANB.MOFkey-v1.pcu	Cl[Zn].N1=NC2=CC3=C([CH]C2=N1)Oc1c(O3)cc2=N[N]N=c2c1.N1=N[C]2C(=N1)C=C1C(=C2)Oc2c(O1)cc1=N[N]N=c1c2.[Zn] MOFid-v1.pcu.cat0
MIL-53(Cr)	Cr.KKEYFWRCBNTPAC.MOFkey-v1.rna	[Cr].[O-]C(═O)c1ccc(cc1)C(═O)[O-].[OH] MOFid-v1.rna.cat0
MIL-100(Cr)	Cr.QMKYBPDZANOJGF.MOFkey-v1.moo	F[Cr][O]([Cr])[Cr].F[Cr][O]([Cr]F)[Cr].[Cr][O]([Cr])[Cr].[O]C(O)c1cc(cc(c1)C(O)[O-])C(O)[O-] MOFid-v1.moo.cat0
MIL-100(Fe)	Fe.QMKYBPDZANOJGF.MOFkey-v1.moo	F[Fe][O]([Fe])[Fe].F[Fe][O]([Fe]F)[Fe].[Fe][O]([Fe])[Fe].[O]C(O)c1cc(cc(c1)C(O)[O-])C(O)[O-] MOFid-v1.moo.cat0
MIL-101(Cr)	Cr.KKEYFWRCBNTPAC.MOFkey-v1.mtn-e	F[Cr][O]([Cr])[Cr].[O-]C(O)c1ccc(cc1)C(O)[O-] MOFid-v1.mtn-e.cat0
MOF-5	Zn.KKEYFWRCBNTPAC.MOFkey-v1.pcu	[O-]C(=O)c1ccc(cc1)C(=O)[O-].[Zn][O]([Zn])([Zn])[Zn] MOFid-v1.pcu.cat0
MOF-525	Zr.ZBSKGGJJCPDFRA.MOFkey-v1.csq	[O-]C(═O)c1ccc(cc1)C1═C2C═CC3═[N]2[Fe]24(n5c1ccc5C(═C1[N]2═C(C═C1)C(═c1n4c(═C3c2ccc(cc2)C(═O)[O-])cc1)c1ccc(cc1)C(═O)[O-])c1ccc(cc1)C(═O)[O-])(Cl)Cl.[OH2][Zr]123([OH2])[O]4[Zr]56[O]3[Zr]37([O]2[Zr]28[O]1[Zr]14([O]6[Zr]([O]53)([O]21)([O]78)([OH2])[OH2])([OH2])[OH2])([OH2])[OH2] MOFid-v1.csq.cat0
MOF-74	Fe.YXUXCIBWQAOXRL.MOFkey-v1.UNKNOWN	[Fe].[O-]C(=O)C1=CC(=O)C(=CC1=O)C(=O)[O-] MOFid-v1.UNKNOWN.cat0
MOF-808/ Zr-BTC	Zr.QMKYBPDZANOJGF.MOFkey-v1.spn	O[Zr]123([OH2])[OH]4[Zr]56([O]3[Zr]37([OH]2[Zr]28([O]1[Zr]14([O]6[Zr]([OH]53)([OH]21)([O]78)([OH2])O)([OH2])(O)O)[OH2])([OH2])(O)O)[OH2].[O-]C(=O)c1cc(cc(c1)C(=O)[O-])C(=O)[O-] MOFid-v1.spn.cat0
NU-901	Zr.HVCDAMXLLUJLQZ.MOFkey-v1.scu	[O]C(=O)c1ccc(cc1)c1cc(c2ccc(cc2)C(=O)[O])c2c3c1ccc1c3c(cc2)c(cc1c1ccc(cc1)C(=O)[O])c1ccc(cc1)C(=O)[O].[O][Zr]123([O])[O]4[Zr]56[O]3[Zr]37([O]2[Zr]28[O]1[Zr]14([O]6[Zr]([O]53)([O]21)([O]78)([O])[O])([O])[O])([O])[O] MOFid-v1.scu.cat0
NU-902	Zr.HHDUMDVQUCBCEY.MOFkey-v1.scu	[O]C(=O)c1ccc(cc1)C1=C2C=CC(=N2)C(=c2ccc(=C(C3=NC(=C(c4[nH]c1cc4)c1ccc(cc1)C(=O)[O])C=C3)c1ccc(cc1)C(=O)[O])[nH]2)c1ccc(cc1)C(=O)[O].[O][Zr]123[O]4[Zr]56[O]3[Zr]37([O]2[Zr]28[O]1[Zr]14([O]6[Zr]([O]53)([O]21)([O]78)([O])[O])([O])[O])([O])[O] MOFid-v1.scu.cat0
NU-907	Zr.MXBBZODCMBYDCL.MOFkey-v1.scu	[O-]C(=O)c1cc(N=Nc2cc(cc(c2)C(=O)[O-])C(=O)[O-])cc(c1)C(=O)[O-].[O-]C(=O)c1cc([N][N]c2cc(cc(c2)C(=O)[O])C(=O)[O])cc(c1)C(=O)[O-].[O][Zr]123([O])[O]4[Zr]56[O]3[Zr]37([O]2[Zr]28[O]1[Zr]14([O]6[Zr]([O]53)([O]21)([O]78)([O])[O])([O])[O])([O])[O] MOFid-v1.scu,UNKNOWN.cat0
NU-1000	Zr.HVCDAMXLLUJLQZ.MOFkey-v1.csq	O[Zr]123([OH2])[OH]4[Zr]56[O]3[Zr]37([OH]2[Zr]28[O]1[Zr]14([O]6[Zr]([OH]53)([OH]21)([O]78)([OH2])O)([OH2])O)([OH2])O.[O]C(O)c1ccc(cc1)c1cc(c2ccc(cc2)C(O)[O])c2c3c1ccc1c3c(cc2)c(cc1c1ccc(cc1)C(O)[O-])c1ccc(cc1)C(O)[O-] MOFid-v1.csq.cat0

NU-1200	Zr.XHTGFZXVBVCVHY.MOFkey-v1.the	[O]C(=O)c1ccc(cc1)C1=[C]C(=[C]C(=[C]1)c1ccc(cc1)C(=O)[O])c1ccc(cc1)C(=O)[O].[O][Zr]123([O])[O]4[Zr]56[O]3[Zr]37([O]2[Zr]28[O]1[Zr]14([O]6[Zr]([O]53)([O]21)([O]78)([O])[O])([O])[O])([O])[O] MOFid-v1.the.cat0
PCN-222 / MOF-545 / MMPF-6	Zr.NTCAAKHGXHIESX.MOFkey-v1.csq	[O]C(=O)c1ccc(cc1)C1=C2C=CC3=[N]2[Rh]24n5c1ccc5C(=C1[N]2=C(C=C1)C(=c1n4c(=C3c2ccc(cc2)C(=O)[O])cc1)c1ccc(cc1)C(=O)[O])c1ccc(cc1)C(=O)[O].[O][Zr]123([O])[OH]4[Zr]56[OH]3[Zr]37([OH]2[Zr]28[OH]1[Zr]14([OH]6[Zr]([OH]53)([OH]21)([OH]78)([O])[O])([O])[O])([O])[O] MOFid-v1.csq.cat0
Hf-PCN-224(Ir) / Ir-PMOF-1(Hf)	Hf.AXPRUEMYFKOYJN.MOFkey-v1.she	[O]C(=O)c1ccc(cc1)C1=C2C=CC3=[N]2[Ir]24(n5c1ccc5C(=C1[N]2=C(C=C1)C(=c1n4c(=C3c2ccc(cc2)C(=O)[O])cc1)c1ccc(cc1)C(=O)[O])c1ccc(cc1)C(=O)[O])(Cl)Cl.[O][Hf]123([O])[O]4[Hf]56([O]3[Hf]37([O]2[Hf]28([O]1[Hf]14([O]6[Hf]([O]53)([O]21)([O]78)([O])[O])([O])[O])([O])[O])([O])[O])([O])[O] MOFid-v1.she.cat0
PCN-601	Ni.VGDUWKPDCXYQCV.MOFkey-v1.ftw	O1[N][C]=C([C]=N1)C1=C2[C]=[C]C3=C(C4=[C][N]ON=[C]4)C4=[N]5[Ni]6(N23)[N]2=C1[C]=[C]C2=C(C1=[C][C]=C(N61)C(=C5[C]=[C]4)C1=[C][N]ON=[C]1)C1=[C][N]ON=[C]1.[O]123[Ni]4567[Ni]89%101[Ni]1%11%122[Ni]2%1334[O]35[Ni]45%147[O]68[Ni]67%104[O]91[Ni]14%126[O]%112[Ni]%13351[O]%1474 MOFid-v1.ftw.cat0
Spiro-1	Zr.LCHFASNGLBVBRA.MOFkey-v1.sjt	[O]C(=O)c1ccc(cc1)c1cc(c2ccc(cc2)C(=O)[O])c2c3c1CCC13CCc3c1c(OP(=O)(O2)[O])c(cc3c1ccc(cc1)C(=O)[O])c1ccc(cc1)C(=O)[O].[O][Zr]123([O])[O]4[Zr]56[O]3[Zr]37([O]2[Zr]28[O]1[Zr]14([O]6[Zr]([O]53)([O]21)([O]78)([O])[O])([O])[O])([O])[O] MOFid-v1.sjt.cat0
Spiro-2	Zr.VDPICMNRZKTVLE.MOFkey-v1.sjt	[O]C(=O)c1ccc2c(c1)ccc(c2)c1cc(c2ccc3c(c2)ccc(c3)C(=O)[O])c2c3c1CCC13CCc3c1c(OP(=O)(O2)[O])c(cc3c1ccc2c(c1)ccc(c2)C(=O)[O])c1ccc2c(c1)ccc(c2)C(=O)[O].[O][Zr]123([O])[O]4[Zr]56[O]3[Zr]37([O]2[Zr]28[O]1[Zr]14([O]6[Zr]([O]53)([O]21)([O]78)([O])[O])([O])[O])([O])[O] MOFid-v1.sjt.cat0
UiO-66	Zr.KKEYFWRCBNTPAC.MOFkey-v1.fcu	[O]C(O)c1ccc(cc1)C(O)[O].[O]12[Zr]34[OH]5[Zr]62[OH]2[Zr]71[OH]4[Zr]14[O]3[Zr]35[O]6[Zr]2([O]71)[OH]43 MOFidv1.fcu.cat0
UiO-66-NH$_2$	Zr.GPNNOCMCNFXRAO.MOFkey-v1.fcu	[O]C(O)c1ccc(c(c1)N)C(O)[O].[O]12[Zr]34[OH]5[Zr]62[OH]2[Zr]71[OH]4[Zr]14[O]3[Zr]35[O]6[Zr]2([O]71)[OH]43 MOFidv1.fcu.cat0
UiO-67	Zr.NEQFBGHQPUXOFH.MOFkeyv1.fcu	[O]C(O)c1ccc(cc1)c1ccc(cc1)C(O)[O].[O]12[Zr]34[OH]5[Zr]62[OH]2[Zr]71[OH]4[Zr]14[O]3[Zr]35[O]6[Zr]2([O]71)[OH]43 MOFid-v1.fcu.cat0
UiO-67-bpy	Zr.KVQMUHHSWICEIH.MOFkey-v1.fcu	[O]C(=O)c1ccc(nc1)c1ccc(cn1)C(=O)[O].[O]12[Zr]34[O]5[Zr]62[O]2[Zr]71[O]4[Zr]14[O]3[Zr]35[O]6[Zr]2([O]71)[O]43 MOFid-v1.fcu.cat0
UiO-68-Me	Zr.CRLKWGCJXNAPTA.MOFkey-v1.fcu	[O]C(=O)c1ccc(cc1)C1=[C][C]=C([C]=[C]1)c1ccc(cc1)C(=O)[O].[O]12[Zr]34[O]5[Zr]62[O]2[Zr]71[O]4[Zr]14[O]3[Zr]35[O]6[Zr]2([O]71)[O]43 MOFid-v1.fcu.cat0
UMCM-1	Zn.KKEYFWRCBNTPAC.OBXYTXDZYVVQSQ.MOFkey-v1.UNKNOWN	[O]C(=O)c1ccc(cc1)C(=O)[O].[O]C(=O)c1ccc(cc1)C1=C[C]=CC(=C1)c1ccc(cc1)C(=O)[O-].[Zn][O]([Zn])([Zn])[Zn] MOFid-v1.UNKNOWN.cat2
Y-TATB / YmesoMOF	Y.MSFXUHUYNSYIDR.MOFkey-v1.UNKNOWN	[O]C(=O)c1ccc(cc1)C1=NC(=[N]=C([N]1)c1ccc(cc1)C(=O)[O])c1ccc(cc1)C(=O)[O-].[O][Y] MOFid-v1.UNKNOWN.cat0
ZIF-71	Zn.HGAMGVPBTDCUNC.MOFkey-v1.rho	ClC1=C(Cl)[N]C=N1.ClC1=NC=N[C]1Cl.[Zn] MOFid-v1.rho.cat0
ZIF-8	Zn.YFFQUDCLMWOYCW.MOFkey-v1.sod	CC1NCC[N]1.[Zn] MOFid-v1.sod.cat0

Note: CIFs for Fe$_2$(dotpdc), MFU-4*l*, and PCN-888 are not readily available to generate MOFids and MOFkeys. CIFs for all other MOFs discussed in this review, and not shown above in Table 2, contain disorder that significantly affects the generation of MOFids and MOFkeys, resulting in structural errors, and thus are also excluded from the table.

Author Contributions

J. L. and J. T. H. developed the scope of the review. J. L., T. A. G., Q. W., J. G. K., M. C. W., Y. Y., and Z. H. S. conducted literature searching and wrote the first draft of manuscript. J. T. H supervised, edited, polished, and refined the following versions of the review. J. M. N. provided critical review comments. All the other co-authors contributed to discussions and editing.

Conflicts of Interest

There are no conflicts to declare.

Acknowledgments

For support of our own work in the field of gas-phase MOF catalysis, we acknowledge the Inorganometallic Catalyst Design Center, an EFRC funded by the DOE, Office of Science, Basic Energy Sciences (DE-SC0012702). For work on photochemical and electrochemical catalysis we acknowledge U. S. Department of Energy (DOE), Office of Science, Basic Energy Sciences (grant DE-FG02-87ER13808). For work relevant to reactive separations we acknowledge the U. S. Department of Energy, Office of Science, Basic Energy Sciences (grant DE-FG02-08ER15967). For work on catalytic destruction of chemical threats, we acknowledge support from the Defense Threat Reduction Agency (HDTRA1-18-1-0003). Z.H.S., M.C.W., and J.G.W. acknowledge support from the National Science Foundation Graduate Research Fellowship program under Grant No. (DGE-1842165).

Notes and References

1. R. Hille, J. Hall and P. Basu, *Chem. Rev.*, 2014, **114**, 3963-4038.
2. E. M. Shepard, S. E. McGlynn, A. L. Bueling, C. S. Grady-Smith, S. J. George, M. A. Winslow, S. P. Cramer, J. W. Peters and J. B. Broderick, *Proc. Natl. Acad. Sci. U.S.A.*, 2010, **107**, 10448-10453.
3. N. Y. Chen, W. W. Kaeding and F. G. Dwyer, *J. Am. Chem. Soc.*, 1979, **101**, 6783-6784.
4. W. W. Kaeding, C. Chu, L. B. Young, B. Weinstein and S. A. Butter, *J. Catal.*, 1981, **67**, 159-174.
5. G. T. Kokotailo, S. L. Lawton, D. H. Olson and W. M. Meier, *Nature*, 1978, **272**, 437–438.
6. B. Smit, L. D. J. C. Loyens, and G. L. M. M. Verbist, *Faraday Discuss.*, 1997, **106**, 93-104.
7. S. Horike, S. Shimomura and S. Kitagawa, *Nat. Chem.*, 2009, **1**, 695-704.
8. S. Krause, N. Hosono and S. Kitagawa, *Angew. Chem. Int. Ed.*, 2020, **59**, 15325-15341.
9. M. J. Kalmutzki, N. Hanikel and O. M. Yaghi, *Sci. Adv.*, 2018, **4**, eaat9180.
10. M. Fujita, Y. J. Kwon, S. Washizu and K. Ogura, *J. Am. Chem. Soc.*, 1994, **116**, 1151-1152.
11. M. Ding, R. W. Flaig, H. L. Jiang and O. M. Yaghi, *Chem. Soc. Rev.*, 2019, **48**, 2783-2828.
12. C. Wang, B. An and W. Lin, *ACS Catal.*, 2018, **9**, 130-146.
13. A. Bavykina, N. Kolobov, I. S. Khan, J. A. Bau, A. Ramirez and J. Gascon, *Chem. Rev.*, 2020, **120**, 8468–8535.
14. M. C. Wasson, C. T. Buru, Z. Chen, T. Islamoglu and O. K. Farha, *Appl. Catal. A.*, 2019, **586**, 117214.
15. A. Dhakshinamoorthy, Z. Li and H. Garcia, *Chem. Soc. Rev.*, 2018, **47**, 8134-8172.
16. H. F. Wang, L. Chen, H. Pang, S. Kaskel and Q. Xu, *Chem. Soc. Rev.*, 2020, **49**, 1414-1448.
17. L. Zhu, X. Q. Liu, H. L. Jiang and L. B. Sun, *Chem. Rev.*, 2017, **117**, 8129-8176.
18. A. Zanon and F. Verpoort, *Coord. Chem. Rev.*, 2017, **353**, 201-222.
19. M. Babucci, A. Guntida and B. C. Gates, *Chem. Rev.*, 2020, **120**, 11956-11985.
20. V. Pascanu, G. Gonzalez Miera, A. K. Inge and B. Martin-Matute, *J. Am. Chem. Soc.*, 2019, **141**, 7223-7234.
21. S. M. J. Rogge, A. Bavykina, J. Hajek, H. Garcia, A. I. Olivos-Suarez, A. Sepulveda-Escribano, A. Vimont, G. Clet, P. Bazin, F. Kapteijn, M. Daturi, E. V. Ramos-Fernandez, I. X. F. X. Llabres, V. Van Speybroeck and J. Gascon, *Chem. Soc. Rev.*, 2017, **46**, 3134-3184.
22. T. A. Goetjen, J. Liu, Y. Wu, J. Sui, X. Zhang, J. T. Hupp and O. K. Farha, *Chem. Commun.*, 2020, **56**, 10409-10418.
23. J. Lee, O. K. Farha, J. Roberts, K. A. Scheidt, S. T. Nguyen and J. T. Hupp, *Chem. Soc. Rev.*, 2009, **38**, 1450-1459.
24. V. Mouarrawis, R. Plessius, J. I. van der Vlugt and J. N. H. Reek, *Front. Chem.*, 2018, **6**, 623.
25. A. B. Grommet, M. Feller and R. Klajn, *Nat. Nanotechnol.*, 2020, **15**, 256-271.
26. B. Mitschke, M. Turberg and B. List, *Chem*, 2020, **6**, 2515-2532.
27. L. Liu and A. Corma, *Nat. Rev. Mater.*, 2020, **6**, 244-263.
28. R. J. Young, M. T. Huxley, E. Pardo, N. R. Champness, C. J. Sumby and C. J. Doonan, *Chem. Sci.*, 2020, **11**, 4031-4050.
29. X. Zhang, P. Li, M. Krzyaniak, J. Knapp, M. R. Wasielewski and O. K. Farha, *Inorg. Chem.*, 2020, **59**, 16795-16798.
30. A. M. Wright, Z. Wu, G. Zhang, J. L. Mancuso, R. J. Comito, R. W. Day, C. H. Hendon, J. T. Miller and M. Dincă, *Chem*, 2018, **4**, 2894-2901.
31. P. Ji, T. Sawano, Z. Lin, A. Urban, D. Boures and W. Lin, *J. Am. Chem. Soc.*, 2016, **138**, 14860-14863.
32. P. Ji, X. Feng, S. S. Veroneau, Y. Song and W. Lin, *J. Am. Chem. Soc.*, 2017, **139**, 15600-15603.
33. P. Ji, J. B. Solomon, Z. Lin, A. Johnson, R. F. Jordan and W. Lin, *J. Am. Chem. Soc.*, 2017, **139**, 11325-11328.
34. H. Furukawa, F. Gandara, Y. B. Zhang, J. Jiang, W. L. Queen, M. R. Hudson and O. M. Yaghi, *J. Am. Chem. Soc.*, 2014, **136**, 4369-4381.
35. O. V. Gutov, M. Gonzalez Hevia, E. C. Escudero-Adan and A. Shafir, *Inorg. Chem.*, 2015, **54**, 8396-8400.
36. J. Ren, M. Ledwaba, N. M. Musyoka, H. W. Langmi, M. Mathe, S. Liao and W. Pang, *Coord. Chem. Rev.*, 2017, **349**, 169-197.
37. F. A. Son, M. C. Wasson, T. Islamoglu, Z. Chen, X. Gong, S. L. Hanna, J. Lyu, X. Wang, K. B. Idrees, J. J. Mahle, G. W. Peterson and O. K. Farha, *Chem. Mater.*, 2020, **32**, 4609-4617.
38. G. C. Shearer, S. Chavan, S. Bordiga, S. Svelle, U. Olsbye and K. P. Lillerud, *Chem. Mater.*, 2016, **28**, 3749-3761.
39. X. Feng, J. Hajek, H. S. Jena, G. Wang, S. K. P. Veerapandian, R. Morent, N. De Geyter, K. Leyssens, A. E. J. Hoffman, V. Meynen, C. Marquez, D. E. De Vos, V. Van Speybroeck, K. Leus and P. Van Der Voort, *J. Am. Chem. Soc.*, 2020, **142**, 3174-3183.

40. W. Xiang, J. Ren, S. Chen, C. Shen, Y. Chen, M. Zhang and C.-j. Liu, *Appl. Energy*, 2020, **277**.
41. L. Liu, Z. Chen, J. Wang, D. Zhang, Y. Zhu, S. Ling, K. W. Huang, Y. Belmabkhout, K. Adil, Y. Zhang, B. Slater, M. Eddaoudi and Y. Han, *Nat. Chem.*, 2019, **11**, 622-628.
42. X. Zhang, M. C. Wasson, M. Shayan, E. K. Berdichevsky, J. Ricardo-Noordberg, Z. Singh, E. K. Papazyan, A. J. Castro, P. Marino, Z. Ajoyan, Z. Chen, T. Islamoglu, A. J. Howarth, Y. Liu, M. B. Majewski, M. J. Katz, J. E. Mondloch and O. K. Farha, *Coord. Chem. Rev.*, 2020, **429**, 213615.
43. Z. Chen, S. L. Hanna, L. R. Redfern, D. Alezi, T. Islamoglu and O. K. Farha, *Coord. Chem. Rev.*, 2019, **386**, 32-49.
44. Z. Hu, Y. Wang and D. Zhao, *Chem. Soc. Rev.*, 2021, **50**, 4629-4683.
45. S. Smolders, K. A. Lomachenko, B. Bueken, A. Struyf, A. L. Bugaev, C. Atzori, N. Stock, C. Lamberti, M. B. J. Roeffaers and D. E. De Vos, *ChemPhysChem*, 2018, **19**, 373-378.
46. X. P. Wu, L. Gagliardi and D. G. Truhlar, *J. Chem. Phys.*, 2019, **150**, 041701.
47. Z. Zhang, S. Liu, X. Li, T. Qin, L. Wang, X. Bo, Y. Liu, L. Xu, S. Wang, X. Sun, Y. Lu, F. Luo and S. Liu, *ACS Appl. Mater. Interfaces*, 2018, **10**, 22023-22030.
48. J. Paier, C. Penschke and J. Sauer, *Chem. Rev.*, 2013, **113**, 3949-3985.
49. J. Jacobsen, A. Ienco, R. D'Amato, F. Costantino and N. Stock, *Dalton Trans.*, 2020, **49**, 16551-16586.
50. D. Yang, M. A. Ortuno, V. Bernales, C. J. Cramer, L. Gagliardi and B. C. Gates, *J. Am. Chem. Soc.*, 2018, **140**, 3751-3759.
51. X. Chen, Y. Lyu, Z. Wang, X. Qiao, B. C. Gates and D. Yang, *ACS Catal.*, 2020, **10**, 2906-2914.
52. Z. B. Fang, T. T. Liu, J. Liu, S. Jin, X. P. Wu, X. Q. Gong, K. Wang, Q. Yin, T. F. Liu, R. Cao and H. C. Zhou, *J. Am. Chem. Soc.*, 2020, **142**, 12515-12523.
53. A. J. Howarth, Y. Liu, P. Li, Z. Li, T. C. Wang, J. T. Hupp and O. K. Farha, *Nat. Rev. Mater.*, 2016, **1**.
54. C. K. Brozek and M. Dinca, *Chem. Soc. Rev.*, 2014, **43**, 5456-5467.
55. M. Lalonde, W. Bury, O. Karagiaridi, Z. Brown, J. T. Hupp and O. K. Farha, *J. Mater. Chem. A*, 2013, **1**, 5453-5468.
56. J. D. Evans, C. J. Sumby and C. J. Doonan, *Chem. Soc. Rev.*, 2014, **43**, 5933-5951.
57. Z. Zhang, L. Wojtas, M. Eddaoudi and M. J. Zaworotko, *J. Am. Chem. Soc.*, 2013, **135**, 5982-5985.
58. P. Cui, P. Wang, Y. Zhao and W.-Y. Sun, *Cryst. Growth Des.*, 2019, **19**, 1454-1470.
59. E. D. Metzger, C. K. Brozek, R. J. Comito and M. Dinca, *ACS Cent. Sci.*, 2016, **2**, 148-153.
60. R. J. Comito, K. J. Fritzsching, B. J. Sundell, K. Schmidt-Rohr and M. Dinca, *J. Am. Chem. Soc.*, 2016, **138**, 10232-10237.
61. E. D. Metzger, R. J. Comito, C. H. Hendon and M. Dinca, *J. Am. Chem. Soc.*, 2017, **139**, 757-762.
62. R. J. Comito, E. D. Metzger, Z. Wu, G. Zhang, C. H. Hendon, J. T. Miller and M. Dincă, *Organometallics*, 2017, **36**, 1681-1683.
63. R. J. Dubey, R. J. Comito, Z. Wu, G. Zhang, A. J. Rieth, C. H. Hendon, J. T. Miller and M. Dinca, *J. Am. Chem. Soc.*, 2017, **139**, 12664-12669.
64. A. W. Stubbs, L. Braglia, E. Borfecchia, R. J. Meyer, Y. Román- Leshkov, C. Lamberti and M. Dincă, *ACS Catal.*, 2017, **8**, 596-601.
65. R. J. Comito, Z. Wu, G. Zhang, J. A. Lawrence, 3rd, M. D. Korzynski, J. A. Kehl, J. T. Miller and M. Dinca, *Angew. Chem. Int. Ed.* , 2018, **57**, 8135-8139.
66. H. D. Park, R. J. Comito, Z. Wu, G. Zhang, N. Ricke, C. Sun, T. Van Voorhis, J. T. Miller, Y. Román-Leshkov and M. Dincă, *ACS Catal.*, 2020, **10**, 3864-3870.
67. M. S. Denny, Jr., L. R. Parent, J. P. Patterson, S. K. Meena, H. Pham, P. Abellan, Q. M. Ramasse, F. Paesani, N. C. Gianneschi and S. M. Cohen, *J. Am. Chem. Soc.*, 2018, **140**, 1348-1357.
68. L. Zou, D. Feng, T. F. Liu, Y. P. Chen, S. Yuan, K. Wang, X. Wang, S. Fordham and H. C. Zhou, *Chem. Sci.*, 2016, **7**, 1063-1069.
69. M. Dan-Hardi, C. Serre, T. Frot, L. Rozes, G. Maurin, C. Sanchez and G. Férey, *J. Am. Chem. Soc.*, 2009, **131**, 10857-10859.
70. C. H. Hendon, D. Tiana, M. Fontecave, C. Sanchez, L. D'Arras, C. Sassoye, L. Rozes, C. Mellot-Draznieks and A. Walsh, *J. Am. Chem. Soc.*, 2013, **135**, 10942 - 10945.
71. S. Vaesen, V. Guillerm, Q. Yang, A. D. Wiersum, B. Marszalek, B. Gil, A. Vimont, M. Daturi, T. Devic, P. L. Llewellyn, C. Serre, G. Maurin and G. De Weireld, *ChemComm.*, 2013, **49**, 10082-10084.
72. S.-N. Kim, J. Kim, H.-Y. Kim, H.-Y. Cho and W.-S. Ahn, *Catal. Today*, 2013, **204**, 85-93.
73. J. G. Santaclara, M. A. Nasalevich, S. Castellanos, W. H. Evers, F. C. Spoor, K. Rock, L. D. Siebbeles, F. Kapteijn, F. Grozema, A. Houtepen, J. Gascon, J. Hunger and M. A. van der Veen, *ChemSusChem*, 2016, **9**, 388-395.
74. G. Capano, F. Ambrosio, S. Kampouri, K. C. Stylianou, A. Pasquarello and B. Smit, *J. Phys. Chem. C*, 2020, **124**, 4065-4072.
75. M. A. Syzgantseva, C. P. Ireland, F. M. Ebrahim, B. Smit and O. A. Syzgantseva, *J. Am. Chem. Soc.*, 2019, **141**, 6271-6278.
76. D. Ao, J. Zhang and H. Liu, *J. Photochem. Photobiol. A*, 2018, **364**, 524-533.
77. L. Hanna, C. L. Long, X. Zhang and J. V. Lockard, *ChemComm.*, 2020, **56**, 11597-11600.
78. M. O'Keeffe, M. A. Peskov, S. J. Ramsden and O. M. Yaghi, *Acc. Chem. Res.*, 2008, **41**, 1782-1789.
79. W. Xu, X. Pei, C. S. Diercks, H. Lyu, Z. Ji and O. M. Yaghi, *J. Am. Chem. Soc.*, 2019, **141**, 17522-17526.
80. Y. Fan, X. Li, K. Gao, Y. Liu, X. Meng, J. Wu and H. Hou, *CrystEngComm*, 2019, **21**, 1666-1673.
81. V. Stavila, M. E. Foster, J. W. Brown, R. W. Davis, J. Edgington, A. I. Benin, R. A. Zarkesh, R. Parthasarathi, D. W. Hoyt, E. D. Walter, A. Andersen, N. M. Washton, A. S. Lipton and M. D. Allendorf, *Chem. Sci.*, 2019, **10**, 9880-9892.
82. M. Rimoldi, A. J. Howarth, M. R. DeStefano, L. Lin, S. Goswami, P. Li, J. T. Hupp and O. K. Farha, *ACS Catal.*, 2017, **7**, 997-1014.
83. Y. Zhang, X. Zhang, J. Lyu, K. I. Otake, X. Wang, L. R. Redfern, C. D. Malliakas, Z. Li, T. Islamoglu, B. Wang and O. K. Farha, *J. Am. Chem. Soc.*, 2018, **140**, 11179-11183.
84. Y. Chen, X. Zhang, M. R. Mian, F. A. Son, K. Zhang, R. Cao, Z. Chen, S. J. Lee, K. B. Idrees, T. A. Goetjen, J. Lyu, P. Li, Q. Xia, Z. Li, J. T. Hupp, T. Islamoglu, A. Napolitano, G. W. Peterson and O. K. Farha, *J. Am. Chem. Soc.*, 2020, **142**, 21428-21438.
85. T. Islamoglu, K.-i. Otake, P. Li, C. T. Buru, A. W. Peters, I.

Akpinar, S. J. Garibay and O. K. Farha, *CrystEngComm*, 2018, **20**, 5913-5918.

86. Y. Zhao, S. Qi, Z. Niu, Y. Peng, C. Shan, G. Verma, L. Wojtas, Z. Zhang, B. Zhang, Y. Feng, Y. S. Chen and S. Ma, *J. Am. Chem. Soc.*, 2019, **141**, 14443-14450.
87. A. W. Peters, K. Otake, A. E. Platero-Prats, Z. Li, M. R. DeStefano, K. W. Chapman, O. K. Farha and J. T. Hupp, *ACS Appl. Mater. Interfaces*, 2018, **10**, 15073-15078.
88. J. H. Cavka, Jakobsen, S., Olsbye, U. Guillou, N., Lamberti, C., Bordiga, S., Lillerud, K. P., *J. Am. Chem. Soc.*, 2008, **130**, 13850-13851.
89. S. Ahn, S. L. Nauert, K. E. Hicks, M. A. Ardagh, N. M. Schweitzer, O. K. Farha, and J. M. Notestein, *ACS Catal.*, 2020, **10**, 2817-2825.
90. X. Wang, X. Zhang, P. Li, K. I. Otake, Y. Cui, J. Lyu, M. D. Krzyaniak, Y. Zhang, Z. Li, J. Liu, C. T. Buru, T. Islamoglu, M. R. Wasielewski, Z. Li and O. K. Farha, *J. Am. Chem. Soc.*, 2019, **141**, 8306-8314.
91. T. A. Goetjen, X. Zhang, J. Liu, J. T. Hupp and O. K. Farha, *ACS Sustain. Chem. Eng.*, 2019, **7**, 2553-2557.
92. X. Zhang, N. A. Vermeulen, Z. Huang, Y. Cui, J. Liu, M. D. Krzyaniak, Z. Li, H. Noh, M. R. Wasielewski, M. Delferro and O. K. Farha, *ACS Appl. Mater. Interfaces*, 2018, **10**, 635-641.
93. Z. Li, A. W. Peters, J. Liu, X. Zhang, N. M. Schweitzer, J. T. Hupp and O. K. Farha, *Inorg. Chem. Front.*, 2017, **4**, 820-824.
94. J. Liu, L. R. Redfern, Y. Liao, T. Islamoglu, A. Atilgan, O. K. Farha and J. T. Hupp, *ACS Appl. Mater. Interfaces*, 2019, **11**, 47822-47829.
95. R. H. Palmer, C. W. Kung, J. Liu, O. K. Farha and J. T. Hupp, *Langmuir*, 2018, **34**, 14143-14150.
96. I. S. Kim, S. Ahn, N. A. Vermeulen, T. E. Webber, L. C. Gallington, K. W. Chapman, R. L. Penn, J. T. Hupp, O. K. Farha, J. M. Notestein and A. B. F. Martinson, *J. Am. Chem. Soc.*, 2020, **142**, 242-250.
97. S. De, G. C. Quan, B. Gikonyo, C. Martineau-Corcos, C. Bousige, L. Veyre, T. Devic, C. Marichy and A. Fateeva, *Inorg. Chem.*, 2020, **59**, 10129-10137.
98. A. W. Peters, Z. Li, O. K. Farha and J. T. Hupp, *ACS Appl. Mater. Interfaces*, 2016, **8**, 20675-20681.
99. H. Noh, C.-W. Kung, K.-i. Otake, A. W. Peters, Z. Li, Y. Liao, X. Gong, O. K. Farha and J. T. Hupp, *ACS Catal.*, 2018, **8**, 9848-9858.
100. Z. Li, A. W. Peters, A. E. Platero-Prats, J. Liu, C. W. Kung, H. Noh, M. R. DeStefano, N. M. Schweitzer, K. W. Chapman, J. T. Hupp and O. K. Farha, *J. Am. Chem. Soc.*, 2017, **139**, 15251-15258.
101. D. Yang and B. C. Gates, *ACS Catal.*, 2019, **9**, 1779-1798.
102. Z. Li, N. M. Schweitzer, A. B. League, V. Bernales, A. W. Peters, A. B. Getsoian, T. C. Wang, J. T. Miller, A. Vjunov, J. L. Fulton, J. A. Lercher, C. J. Cramer, L. Gagliardi, J. T. Hupp and O. K. Farha, *J. Am. Chem. Soc.*, 2016, **138**, 1977-1982.
103. I. S. Kim, Z. Li, J. Zheng, A. E. Platero-Prats, A. Mavrandonakis, S. Pellizzeri, M. Ferrandon, A. Vjunov, L. C. Gallington, T. E. Webber, N. A. Vermeulen, R. L. Penn, R. B. Getman, C. J. Cramer, K. W. Chapman, D. M. Camaioni, J. L. Fulton, J. A. Lercher, O. K. Farha, J. T. Hupp and A. B. F. Martinson, *Angew. Chem. Int. Ed.* , 2018, **57**, 909-913.
104. Y. Yang, H. Noh, Q. Ma, R. Wang, Z. Chen, N. M. Schweitzer, J. Liu, K. W. Chapman and J. T. Hupp, *ACS Appl. Mater. Interfaces*, 2021, **13**, 36232-36239.
105. A. M. Abdel-Mageed, B. Rungtaweevoranit, M. Parlinska-Wojtan, X. Pei, O. M. Yaghi and R. J. Behm, *J. Am. Chem. Soc.*, 2019, **141**, 5201-5210.
106. A. E. Platero-Prats, A. B. League, V. Bernales, J. Ye, L. C. Gallington, A. Vjunov, N. M. Schweitzer, Z. Li, J. Zheng, B. L. Mehdi, A. J. Stevens, A. Dohnalkova, M. Balasubramanian, O. K. Farha, J. T. Hupp, N. D. Browning, J. L. Fulton, D. M. Camaioni, J. A. Lercher, D. G. Truhlar, L. Gagliardi, C. J. Cramer and K. W. Chapman, *J. Am. Chem. Soc.*, 2017, **139**, 10410-10418.
107. J. Li, H. Huang, P. Liu, X. Song, D. Mei, Y. Tang, X. Wang and C. Zhong, *Journal of Catalysis*, 2019, **375**, 351-360.
108. Z. H. Syed, F. Sha, X. Zhang, D. M. Kaphan, M. Delferro and O. K. Farha, *ACS Catal.*, 2020, **10**, 11556-11566.
109. X. He, B. G. Looker, K. T. Dinh, A. W. Stubbs, T. Chen, R. J. Meyer, P. Serna, Y. Román-Leshkov, K. M. Lancaster and M. Dincă, *ACS Catal.*, 2020, **10**, 7820-7825.
110. X. Feng, Y. Song, J. S. Chen, Z. Xu, S. J. Dunn and W. Lin, *J. Am. Chem. Soc.*, 2021, **143**, 1107-1118.
111. Y. Pi, X. Feng, Y. Song, Z. Xu, Z. Li and W. Lin, *J. Am. Chem. Soc.*, 2020, **142**, 10302-10307.
112. P. Ji, Y. Song, T. Drake, S. S. Veroneau, Z. Lin, X. Pan and W. Lin, *J. Am. Chem. Soc.*, 2018, **140**, 433-440.
113. K. Manna, P. Ji, F. X. Greene and W. Lin, *J. Am. Chem. Soc.*, 2016, **138**, 7488-7491.
114. K. I. Otake, Y. Cui, C. T. Buru, Z. Li, J. T. Hupp and O. K. Farha, *J. Am. Chem. Soc.*, 2018, **140**, 8652-8656.
115. R. R. Langeslay, D. M. Kaphan, C. L. Marshall, P. C. Stair, A. P. Sattelberger and M. Delferro, *Chem. Rev.*, 2019, **119**, 2128-2191.
116. A. S. Rosen, J. M. Notestein and R. Q. Snurr, *J. Comput. Chem.*, 2019, **40**, 1305-1318.
117. V. Bernales, M. A. Ortuno, D. G. Truhlar, C. J. Cramer and L. Gagliardi, *ACS Cent. Sci.*, 2018, **4**, 5-19.
118. K. D. Vogiatzis, E. Haldoupis, D. J. Xiao, J. R. Long, J. I. Siepmann and L. Gagliardi, *J. Phys. Chem. C*, 2016, **120**, 18707-18712.
119. G. A. McCarver, T. Rajeshkumar and K. D. Vogiatzis, *Coord. Chem. Rev.*, 2021, **436**, 213777.
120. X. P. Wu, I. Choudhuri and D. G. Truhlar, *Energy Environ. Mater.*, 2019, **2**, 251-263.
121. A. B. Thompson, D. R. Pahls, V. Bernales, L. C. Gallington, C. D. Malonzo, T. Webber, S. J. Tereniak, T. C. Wang, S. P. Desai, Z. Li, I. S. Kim, L. Gagliardi, R. L. Penn, K. W. Chapman, A. Stein, O. K. Farha, J. T. Hupp, A. B. F. Martinson and C. C. Lu, *Chem. Mater.*, 2016, **28**, 6753-6762.
122. J. Baek, B. Rungtaweevoranit, X. Pei, M. Park, S. C. Fakra, Y. S. Liu, R. Matheu, S. A. Alshmimri, S. Alshehri, C. A. Trickett, G. A. Somorjai and O. M. Yaghi, *J. Am. Chem. Soc.*, 2018, **140**, 18208-18216.
123. W. Peng, X. Qu, S. Shaik and B. Wang, *Nat. Catal.*, 2021, **4**, 266-273.
124. G. E. Cutsail, 3rd, M. O. Ross, A. C. Rosenzweig and S. DeBeer, *Chem. Sci.*, 2021, **12**, 6194-6209.
125. Y. Song, Z. Li, P. Ji, M. Kaufmann, X. Feng, J. S. Chen, C. Wang and W. Lin, *ACS Catal.*, 2019, **9**, 1578-1583.
126. X. Feng, P. Ji, Z. Li, T. Drake, P. Oliveres, E. Y. Chen, Y. Song, C. Wang and W. Lin, *ACS Catal.*, 2019, **9**, 3327-3337.
127. C. Copéret, M. Chabanas, R. Petroff Saint-Arroman and J.-M. Basset, *Angew. Chem. Int. Ed.* , 2003, **42**, 156-181.
128. M. K. Samantaray, V. D'Elia, E. Pump, L. Falivene, M. Harb,

S. Ould Chikh, L. Cavallo and J. M. Basset, *Chem. Rev.*, 2020, **120**, 734-813.

129. Z. Thiam, E. Abou-Hamad, B. Dereli, L. Liu, A. H. Emwas, R. Ahmad, H. Jiang, A. A. Isah, P. B. Ndiaye, M. Taoufik, Y. Han, L. Cavallo, J. M. Basset and M. Eddaoudi, *J. Am. Chem. Soc.*, 2020, **142**, 16690-16703.
130. M. Rimoldi, A. Nakamura, N. A. Vermeulen, J. J. Henkelis, A. K. Blackburn, J. T. Hupp, J. F. Stoddart and O. K. Farha, *Chem. Sci.*, 2016, **7**, 4980-4984.
131. S. T. Madrahimov, J. R. Gallagher, G. Zhang, Z. Meinhart, S. J. Garibay, M. Delferro, J. T. Miller, O. K. Farha, J. T. Hupp and S. T. Nguyen, *ACS Catal.*, 2015, **5**, 6713-6718.
132. N. Van Velthoven, M. Henrion, J. Dallenes, A. Krajnc, A. L. Bugaev, P. Liu, S. Bals, A. V. Soldatov, G. Mali and D. E. De Vos, *ACS Catal.*, 2020, **10**, 5077-5085.
133. D. Yang, S. O. Odoh, T. C. Wang, O. K. Farha, J. T. Hupp, C. J. Cramer, L. Gagliardi and B. C. Gates, *J. Am. Chem. Soc.*, 2015, **137**, 7391-7396.
134. V. Bernales, D. Yang, J. Yu, G. Gumuslu, C. J. Cramer, B. C. Gates and L. Gagliardi, *ACS Appl. Mater. Interfaces*, 2017, **9**, 33511-33520.
135. S. P. Desai, J. Ye, J. Zheng, M. S. Ferrandon, T. E. Webber, A. E. Platero-Prats, J. Duan, P. Garcia-Holley, D. M. Camaioni, K. W. Chapman, M. Delferro, O. K. Farha, J. L. Fulton, L. Gagliardi, J. A. Lercher, R. L. Penn, A. Stein and C. C. Lu, *J. Am. Chem. Soc.*, 2018, **140**, 15309-15318.
136. R. C. Klet, S. Tussupbayev, J. Borycz, J. R. Gallagher, M. M. Stalzer, J. T. Miller, L. Gagliardi, J. T. Hupp, T. J. Marks, C. J. Cramer, M. Delferro and O. K. Farha, *J. Am. Chem. Soc.*, 2015, **137**, 15680-15683.
137. C. Larabi and E. A. Quadrelli, *Eur. J. Inorg. Chem.*, 2012, **18**, 3014-3022.
138. C.-D. Wu, A. Hu, L. Zhang and W. Lin, *J. Am. Chem. Soc.*, 2005, **127**, 8940-8941.
139. K. S. Suslick, P. Bhyrappa, J. H. Chou, M. E. Kosal, S. Nakagaki, D. W. Smithenry and S. R. Wilson, *Acc. Chem. Res.*, 2005, **38**, 283-291.
140. S. H. Cho, B. Ma, S. T. Nguyen, J. T. Hupp and T. E. Albrecht-Schmitt, *Chem. Commun.*, 2006, 2563-2565.
141. X. Feng, Y. Pi, Y. Song, Z. Xu, Z. Li and W. Lin, *ACS Catal.*, 2021, **11**, 1024-1032.
142. T. Sawano, Z. Lin, D. Boures, B. An, C. Wang and W. Lin, *J. Am. Chem. Soc.*, 2016, **138**, 9783-9786.
143. H. Fei and S. M. Cohen, *Chem. Commun.*, 2014, **50**, 4810-4812.
144. A. Schneemann, L. F. Wan, A. S. Lipton, Y. S. Liu, J. L. Snider, A. A. Baker, J. D. Sugar, C. D. Spataru, J. Guo, T. S. Autrey, M. Jørgensen, T. R. Jensen, B. C. Wood, M. D. Allendorf and V. Stavila, *ACS Nano*, 2020, **14**, 10294 - 10304.
145. S. Abednatanzi, P. G. Derakhshandeh, A. Abbasi, P. Van Der Voort and K. Leus, *ChemCatChem*, 2016, **8**, 3672-3679.
146. T. Toyao, K. Miyahara, M. Fujiwaki, T.-H. Kim, S. Dohshi, Y. Horiuchi and M. Matsuoka, *J. Phys. Chem. C*, 2015, **119**, 8131-8137.
147. K. Manna, T. Zhang and W. Lin, *J. Am. Chem. Soc.*, 2014, **136**, 6566-6569.
148. K. Manna, T. Zhang, F. X. Greene and W. Lin, *J. Am. Chem. Soc.*, 2015, **137**, 2665-2673.
149. H. Fei, M. D. Sampson, Y. Lee, C. P. Kubiak and S. M. Cohen, *Inorg. Chem.*, 2015, **54**, 6821-6828.
150. D. Kim, D. R. Whang and S. Y. Park, *J. Am. Chem. Soc.*, 2016, **138**, 8698-8701.
151. Z. H. Syed, Z. Chen, K. B. Idrees, T. A. Goetjen, E. C. Wegener, X. Zhang, K. W. Chapman, D. M. Kaphan, M. Delferro and O. K. Farha, *Organometallics*, 2020, **39**, 1123-1133.
152. N. C. Thacker, P. Ji, Z. Lin, A. Urban and W. Lin, *Faraday Discuss.*, 2017, **201**, 303-315.
153. J. Li, J. Liao, Y. Ren, C. Liu, C. Yue, J. Lu and H. Jiang, *Angew. Chem. Int. Ed.*, 2019, **58**, 17148-17152.
154. H. Fei and S. M. Cohen, *J. Am. Chem. Soc.*, 2015, **137**, 2191-2194.
155. H. Fei, J. Shin, Y. S. Meng, M. Adelhardt, J. Sutter, K. Meyer and S. M. Cohen, *J. Am. Chem. Soc.*, 2014, **136**, 4965-4973.
156. H. G. T. Nguyen, M. H. Weston, A. A. Sarjeant, D. M. Gardner, Z. An, R. Carmieli, M. R. Wasielewski, O. K. Farha, J. T. Hupp and S. T. Nguyen, *Cryst. Growth Des.*, 2013, **13**, 3528-3534.
157. S. Nakagaki, G. K. Ferreira, G. M. Ucoski and K. A. Dias de Freitas Castro, *Molecules*, 2013, **18**, 7279-7308.
158. I. Hod, M. D. Sampson, P. Deria, C. P. Kubiak, O. K. Farha and J. T. Hupp, *ACS Catal.*, 2015, **5**, 6302-6309.
159. A. M. Szczepkowska, M. Janeta, M. Siczek, W. Tylus, A. M. Trzeciak and W. Bury, *Dalton Trans.*, 2021, **50**, 9051-9058.
160. X. N. Wang, P. Zhang, A. Kirchon, J. L. Li, W. M. Chen, Y. M. Zhao, B. Li and H. C. Zhou, *J. Am. Chem. Soc.*, 2019, **141**, 13654-13663.
161. B. A. Johnson, A. Bhunia and S. Ott, *Dalton Trans.*, 2017, **46**, 1382-1388.
162. Y. Y. Zhu, G. Lan, Y. Fan, S. S. Veroneau, Y. Song, D. Micheroni and W. Lin, *Angew. Chem. Int. Ed.*, 2018, **57**, 14090-14094.
163. S. Lin, A. K. Ravari, J. Zhu, P. M. Usov, M. Cai, S. R. Ahrenholtz, Y. Pushkar and A. J. Morris, *ChemSusChem*, 2018, **11**, 464-471.
164. M. I. Gonzalez, E. D. Bloch, J. A. Mason, S. J. Teat and J. R. Long, *Inorg. Chem.*, 2015, **54**, 2995-3005.
165. P. Valvekens, E. D. Bloch, J. R. Long, R. Ameloot and D. E. De Vos, *Catal. Today*, 2015, **246**, 55-59.
166. T. Zhang, K. Manna and W. Lin, *J. Am. Chem. Soc.*, 2016, **138**, 3241-3249.
167. X. Feng, Y. Song, Z. Li, M. Kaufmann, Y. Pi, J. S. Chen, Z. Xu, Z. Li, C. Wang and W. Lin, *J. Am. Chem. Soc.*, 2019, **141**, 11196-11203.
168. C. Sun, G. Skorupskii, J. H. Dou, A. M. Wright and M. Dinca, *J. Am. Chem. Soc.*, 2018, **140**, 17394-17398.
169. M. B. Andrus and D. Asgari, *Tetrahedron*, 2000, **56**, 5775-5780.
170. C. T. Buru, J. Lyu, J. Liu and O. K. Farha, *Front. Mater.*, 2019, **6**, 1 - 9.
171. C. T. Buru and O. K. Farha, *ACS Appl. Mater. Interfaces*, 2020, **12**, 5345-5360.
172. C. T. Buru, A. E. Platero-Prats, D. G. Chica, M. G. Kanatzidis, K. W. Chapman and O. K. Farha, *J. Mater. Chem. A*, 2018, **6**, 7389-7394.
173. C. T. Buru, P. Li, B. L. Mehdi, A. Dohnalkova, A. E. Platero-Prats, N. D. Browning, K. W. Chapman, J. T. Hupp and O. K. Farha, *Chem. Mater.*, 2017, **29**, 5174-5181.
174. J. Sun, S. Abednatanzi, P. Van Der Voort, Y.-Y. Liu and K. Leus, *Catalysts*, 2020, **10**, 578.
175. M. Samaniyan, M. Mirzaei, R. Khajavian, H. Eshtiagh-Hosseini and C. Streb, *ACS Catal.*, 2019, **9**, 10174-10191.
176. P. Mialane, C. Mellot-Draznieks, P. Gairola, M. Duguet, Y.

This journal is © The Royal Society of Chemistry 20xx

Please do not adjust margins

Benseghir, O. Oms and A. Dolbecq, *Chem. Soc. Rev.*, 2021, **50**, 6152-6220.

177. S. Mukhopadhyay, J. Debgupta, C. Singh, A. Kar and S. K. Das, *Angew. Chem. Int. Ed.*, 2018, **57**, 1918-1923.
178. K. S. Park, Z. Ni, A. P. Côté, J. Y. Choi, R. Huang, F. J. Uribe-Romo, H. K. Chae, M. O'Keeffe and O. M. Yaghi, *Proc. Natl. Acad. Sci. U.S.A.*, 2006, **103**, 10186.
179. Y. Liu, V. Kravtsov and M. Eddaoudi, *Angew. Chem. Int. Ed.*, 2008, **47**, 8446-8449.
180. P. Kukkar, K. Kim, D. Kukkar, P. Singh, *Coord. Chem. Rev.*, 2021, **446**, 214109.
181. L. Bromberg, Y. Diao, H. Wu, S. A. Speakman and T. A. Hatton, *Chem. Mater.*, 2012, **24**, 1664-1675.
182. L. H. Wee, F. Bonino, C. Lamberti, S. Bordiga and J. A. Martens, *Green Chem.*, 2014, **16**, 1351-1357.
183. A. Grigoropoulos, A. I. McKay, A. P. Katsoulidis, R. P. Davies, A. Haynes, L. Brammer, J. Xiao, A. S. Weller and M. J. Rosseinsky, *Angew. Chem. Int. Ed.*, 2018, **57**, 4532-4537.
184. G. Zhou, B. Wang and R. Cao, *J. Am. Chem. Soc.*, 2020, **142**, 14848-14853.
185. J. Pang, S. Yuan, J. S. Qin, C. T. Lollar, N. Huang, J. Li, Q. Wang, M. Wu, D. Yuan, M. Hong and H. C. Zhou, *J. Am. Chem. Soc.*, 2019, **141**, 3129-3136.
186. R. Adam, M. Mon, R. Greco, L. H. G. Kalinke, A. Vidal-Moya, A. Fernandez, R. E. P. Winpenny, A. Domenech-Carbo, A. Leyva-Perez, D. Armentano, E. Pardo and J. Ferrando-Soria, *J. Am. Chem. Soc.*, 2019, **141**, 10350-10360.
187. J. Ren, P. C. Lan, M. Chen, W. Zhang and S. Ma, *Organometallics*, 2019, **38**, 3460-3465.
188. A. Rossin, G. Tuci, L. Luconi and G. Giambastiani, *ACS Catal.*, 2017, **7**, 5035-5045.
189. T. Friscic, C. Mottillo and H. M. Titi, *Angew. Chem. Int. Ed.*, 2020, **59**, 1018-1029.
190. T. Stolar and K. Užarević, *CrystEngComm*, 2020, **22**, 4511-4525.
191. B. Szczęśniak, S. Borysiuk, J. Choma and M. Jaroniec, *Mater. Horiz.*, 2020, **7**, 1457-1473.
192. G. E. Dobereiner, N. Hazari and N. D. Schley, *Organometallics*, 2021, **40**, 295-301.
193. D. T. Genna, A. G. Wong-Foy, A. J. Matzger and M. S. Sanford, *J. Am. Chem. Soc.*, 2013, **135**, 10586-10589.
194. D. T. Genna, L. Y. Pfund, D. C. Samblanet, A. G. Wong-Foy, A. J. Matzger and M. S. Sanford, *ACS Catal.*, 2016, **6**, 3569-3574.
195. R. C. Klet, Y. Liu, T. C. Wang, J. T. Hupp and O. K. Farha, *J. Mater. Chem. A*, 2016, **4**, 1479-1485.
196. Y. Liao, T. Sheridan, J. Liu, O. Farha and J. Hupp, *ACS Appl. Mater. Interfaces*, 2021, **13**, 30565-30575.
197. J. An, O. K. Farha, J. T. Hupp, E. Pohl, J. I. Yeh and N. L. Rosi, *Nat. Commun.*, 2012, **3**, 604.
198. Z. Li, T. M. Rayder, L. Luo, J. A. Byers and C. K. Tsung, *J. Am. Chem. Soc.*, 2018, **140**, 8082-8085.
199. J. V. Morabito, L. Y. Chou, Z. Li, C. M. Manna, C. A. Petroff, R. J. Kyada, J. M. Palomba, J. A. Byers and C. K. Tsung, *J. Am. Chem. Soc.*, 2014, **136**, 12540-12543.
200. M. Viciano-Chumillas, M. Mon, J. Ferrando-Soria, A. Corma, A. Leyva-Perez, D. Armentano and E. Pardo, *Acc. Chem. Res.*, 2020, **53**, 520-531.
201. M. A. Nasalevich, R. Becker, E. V. Ramos-Fernandez, S. Castellanos, S. L. Veber, M. V. Fedin, F. Kapteijn, J. N. H. Reek, J. I. van der Vlugt and J. Gascon, *Energy Environ. Sci.*, 2015, **8**, 364-375.
202. X. Wang, F. M. Wisser, J. Canivet, M. Fontecave and C. Mellot-Draznieks, *ChemSusChem*, 2018, **11**, 3315-3322.
203. W.-L. Liu, S. Lirio, H.-Y. Huang and S. Ma, in *Functional Supramolecular Materials: From Surfaces to MOFs*, The Royal Society of Chemistry, 2017, DOI: 10.1039/9781788010276-00281, pp. 281-296.
204. X. Wang, P. C. Lang and S. Ma, *ACS Cent. Sci.*, 2020, **6**, 1497 - 1506.
205. P. R. A. F. Garcia, R. N. Bicev, C. L. P. Oliveira, O. A. Sant'Anna and M. C. A. Fantini, *Microporous Mesoporous Mater.*, 2016, **235**, 59-68.
206. C.-H. Lee, T.-S. Lin and C.-Y. Mou, *Nano Today*, 2009, **4**, 165-179.
207. P. Li, S. Y. Moon, M. A. Guelta, L. Lin, D. A. Gomez-Gualdron, R. Q. Snurr, S. P. Harvey, J. T. Hupp and O. K. Farha, *ACS Nano*, 2016, **10**, 9174-9182.
208. V. Lykourinou, Y. Chen, X. Wang, L. Meng, T. Hoang, L. J. Ming, R. L. Musselman and S. Ma, *J. Am. Chem. Soc.*, 2011, **133**, 10382–10385.
209. Y. Chen, S. Han, X. Li, Z. Zhang and S. Ma, *Inorg. Chem.*, 2014, **53**, 10006 - 10008.
210. Y. Pan, H. Li, J. Farmakes, F. Xiao, B. Chen, S. Ma and Z. Yang, *J. Am. Chem. Soc.*, 2018, **140**, 16032–16036.
211. Y. Chen, P. Li, J. A. Modica, R. J. Drout and O. K. Farha, *J. Am. Chem. Soc.*, 2018, **140**, 5678 - 5681.
212. X. Wu, J. Ge, C. Yang, M. Hou and Z. Liu, *Chem. Commun.*, 2015, **51**, 13408 - 13411.
213. X. Lian, Y. Huang, Y. Zhu, Y. Fang, R. Zhao, E. Joseph, J. Li, J. P. Pellois and H. C. Zhou., *Angew. Chem. Int. Ed.*, 2018, **130**, 5827 - 5833.
214. W. Liang, H. Xu, F. Carraro, N. K. Maddigan, Q. Li, S. G. Bell, D. M. Huang, A. Tarzia, M. B. Solomon, H. Amenitsch, L. Vaccari, C. J. Sumby, P. Falcaro and C. J. Doonan, *J. Am. Chem. Soc.*, 2019, **141**, 2348 - 2355.
215. P. Li, J. A. Modica, A. J. Howarth, L. E. Vargas, P. Z. Moghadam, R. Q. Snurr, M. Mrksich, J. T. Hupp and O. K. Farha, *Chem*, 2016, **1**, 154 - 169.
216. P. Li, Q. Chen, T. C. Wang, N. A. Vermeulen, B. L. Mehdi, A. Dohnalkova, N. D. Browning, D. Shen, R. Anderson, D. A. Gómez-Gualdrón, F. M. Cetin, J. Jagiello, A. M. Asiri, J. F. Stoddart and O. K. Farha, *Chem*, 2018, **4**, 1022-1034.
217. Y. Chen, P. Li, H. Noh, C. W. Kung, C. T. Buru, X. Wang, X. Zhang and O. K. Farha, *Angew. Chem. Int. Ed.*, 2019, **58**, 7682-7686.
218. Y. Chen, P. Li, J. Zhou, C. T. Buru, L. Dordevic, P. Li, X. Zhang, M. M. Cetin, J. F. Stoddart, S. I. Stupp, M. R. Wasielewski and O. K. Farha, *J. Am. Chem. Soc.*, 2020, **142**, 1768-1773.
219. P. Li, S. Y. Moon, M. A. Guelta, S. P. Harvey, J. T. Hupp and O. K. Farha, *J. Am. Chem. Soc.*, 2016, **138**, 8052-8055.
220. F. Lyu, Y. Zhang, R. N. Zare, J. Ge and Z. Liu, *Nano Lett.*, 2014, **14**, 5761 - 5765.
221. A. Maleki, M. A. Shahbazi, V. Alinezhad and H. A. Santos, *Adv. Healthc. Mater.*, 2020, **9**, e2000248.
222. W. Liang, P. Wied, F. Carraro, C. J. Sumby, B. Nidetzky, C. K. Tsung, P. Falcaro and C. J. Doonan, *Chem. Rev.*, 2021, **121**, 1077-1129.
223. N. Liedana, A. Galve, C. Rubio, C. Tellez and J. Coronas, *ACS Appl. Mater. Interfaces*, 2012, **4**, 5016-5021.
224. J. Guo, L. Yang, Z. Gao, C. i. Zhao, Y. Mei and Y.-Y. Song, *ACS Catal.*, 2020, **10**, 5949 - 5958.
225. Y. Cao, X. Li, J. Xiong, L. Wang, L.-T. Yan and J. Ge, *Nanoscale*, 2019, **11**, 22108 - 22117.

226. H. Wu, J. Yang, Z. M. Su, S. R. Batten and J. F. Ma, *J. Am. Chem. Soc.*, 2011, **133**, 11406-11409.
227. J. Park, D. Yuan, K. T. Pham, J. R. Li, A. Yakovenko and H. C. Zhou, *J. Am. Chem. Soc.*, 2012, **134**, 99-102.
228. Y. Feng, Q. Chen, M. Jiang and J. Yao, *Ind. Eng. Chem. Res.*, 2019, **58**, 17646-17659.
229. A. Ghoufi, K. Benhamed, L. Boukli-Hacene and G. Maurin, *ACS Cent. Sci.*, 2017, **3**, 394-398.
230. L. R. Parent, C. H. Pham, J. P. Patterson, M. S. Denny, Jr., S. M. Cohen, N. C. Gianneschi and F. Paesani, *J. Am. Chem. Soc.*, 2017, **139**, 13973-13976.
231. A. Schneemann, V. Bon, I. Schwedler, I. Senkovska, S. Kaskel and R. A. Fischer, *Chem. Soc. Rev.*, 2014, **43**, 6062-6096.
232. C. Serre, F. Millange, C. Thouvenot, M. Noguès, G. Marsolier, D. Louër and G. Férey, *J. Am. Chem. Soc.*, 2002, **124**, 13519–13526.
233. D. Fairen-Jimenez, S. A. Moggach, M. T. Wharmby, P. A. Wright, S. Parsons and T. Duren, *J. Am. Chem. Soc.*, 2011, **133**, 8900-8902.
234. T. Tian, M. T. Wharmby, J. B. Parra, C. O. Ania and D. Fairen-Jimenez, *Dalton Trans.*, 2016, **45**, 6893-6900.
235. G. Lu, S. Li, Z. Guo, O. K. Farha, B. G. Hauser, X. Qi, Y. Wang, X. Wang, S. Han, X. Liu, J. S. DuChene, H. Zhang, Q. Zhang, X. Chen, J. Ma, S. C. J. Loo, W. D. Wei, Y. Yang, J. T. Hupp and F. Huo, *Nat. Chem.*, 2012, **4**, 310.
236. Y. Jiang, X. Zhang, X. Dai, W. Zhang, Q. Sheng, H. Zhuo, Y. Xiao and H. Wang, *Nano Res.*, 2017, **10**, 876–889.
237. T. Zeng, X. Zhang, S. Wang, H. Niu and Y. Cai, *Environ. Sci. Technol.*, 2015, **49**, 2350-2357.
238. Y. Y. Zhang, J. X. Li, L. L. Ding, L. Liu, S. M. Wang and Z. B. Han, *Inorg. Chem.*, 2018, **57**, 13586-13593.
239. I. Gumus, Y. Karataş and M. Gülcan, *Catal. Sci. Technol.*, 2020, **10**, 4990-4999.
240. U. Stoeck, S. Krause, V. Bon, I. Senkovska and S. Kaskel, *Chem. Commun.*, 2012, **48**, 10841-10843.
241. D. Feng, Z. Y. Gu, J. R. Li, H. L. Jiang, Z. Wei and H. C. Zhou, *Angew. Chem. Int. Ed.*, 2012, **51**, 10307-10310.
242. W. Morris, B. Volosskiy, S. Demir, F. Gandara, P. L. McGrier, H. Furukawa, D. Cascio, J. F. Stoddart and O. M. Yaghi, *Inorg. Chem.*, 2012, **51**, 6443-6445.
243. Y. Chen, T. Hoang and S. Ma, *Inorg. Chem.*, 2012, **51**, 12600-12602.
244. S. Goswami, H. Noh, L. R. Redfern, K.-i. Otake, C.-W. Kung, Y. Cui, K. W. Chapman, O. K. Farha and J. T. Hupp, *Chem. Mater.*, 2019, **31**, 1485-1490.
245. Z. Zhang, S. Zhang, Q. Yao, X. Chen and Z. H. Lu, *Inorg. Chem.*, 2017, **56**, 11938-11945.
246. A. Corma, H. Garcia and F. X. Llabres i Xamena, *Chem. Rev.*, 2010, **110**, 4606-4655.
247. A. E. Platero-Prats, Z. Li, L. C. Gallington, A. W. Peters, J. T. Hupp, O. K. Farha and K. W. Chapman, *Faraday Discuss.*, 2017, **201**, 337-350.
248. M. R. Mian, L. R. Redfern, S. M. Pratik, D. Ray, J. Liu, K. B. Idrees, T. Islamoglu, L. Gagliardi and O. K. Farha, *Chem. Mater.*, 2020, **32**, 3078-3086.
249. Y. Yang, X. Zhang, S. Kanchanakungwankul, Z. Lu, H. Noh, Z. H. Syed, O. K. Farha, D. G. Truhlar and J. T. Hupp, *J. Am. Chem. Soc.*, 2020, **142**, 21169-21177.
250. Z. Lu, J. Liu, X. Zhang, Y. Liao, R. Wang, K. Zhang, J. Lyu, O. K. Farha and J. T. Hupp, *J. Am. Chem. Soc.*, 2020, **142**, 21110-21121.
251. X. Qiu, J. Chen, X. Zou, R. Fang, L. Chen, Z. Chen, K. Shen and Y. Li, *Chem. Sci.*, 2018, **9**, 8962-8968.
252. L. Luo, W. S. Lo, X. Si, H. Li, Y. Wu, Y. An, Q. Zhu, L. Y. Chou, T. Li and C. K. Tsung, *J. Am. Chem. Soc.*, 2019, **141**, 20365–20370.
253. J. Cure, E. Mattson, K. Cocq, H. Assi, S. Jensen, K. Tan, M. Catalano, S. Yuan, H. Wang, L. Feng, P. Zhang, S. Kwon, J.-F. Veyan, Y. Cabrera, G. Zhang, J. Li, M. Kim, H.-C. Zhou, Y. J. Chabal and T. Thonhauser, *J. Mater. Chem. A*, 2019, **7**, 17536-17546.
254. S. Abedi and A. Morsali, *New J. Chem.*, 2017, **41**, 5846-5852.
255. J. Su, S. Yuan, T. Wang, C. T. Lollar, J.-L. Zuo, J. Zhang and H.-C. Zhou, *Chem. Sci.*, 2020, **11**, 1918-1925.
256. K. Zhang, R. P. Lively, M. E. Dose, A. J. Brown, C. Zhang, J. Chung, S. Nair, W. J. Koros and R. R. Chance, *Chem. Commun.*, 2013, **49**, 3245-3247.
257. I. Hod, W. Bury, D. M. Gardner, P. Deria, V. Roznyatovskiy, M. R. Wasielewski, O. K. Farha and J. T. Hupp, *J. Phys. Chem. Lett.*, 2015, **6**, 586-591.
258. P. J. Celis-Salazar, M. Cai, C. A. Cucinell, S. R. Ahrenholtz, C. C. Epley, P. M. Usov and A. J. Morris, *J. Am. Chem. Soc.*, 2019, **141**, 11947-11953.
259. B. Chen, Z. Yang, Y. Zhu and Y. Xia, *J. Mater. Chem. A*, 2014, **2**, 16811-16831.
260. A. Phan, C. J. Doonan, F. J. Uribe-Romo, C. B. Knobler, M. O'Keeffe and O. M. Yaghi, *Acc. Chem. Res.*, 2010, **43**, 58-67.
261. J. Winarta, B. Shan, S. M. McIntyre, L. Ye, C. Wang, J. Liu and B. Mu, *Cryst. Growth Des.*, 2019, **20**, 1347-1362.
262. L. Diestel, H. Bux, D. Wachsmuth and J. Caro, *Microporous Mesoporous Mater.*, 2012, **164**, 288-293.
263. G. Lu and J. T. Hupp, *J. Am. Chem. Soc.*, 2010, **132**, 7832-7833.
264. C. O. Audu, D. Chen, C. W. Kung, R. Q. Snurr, S. T. Nguyen, O. K. Farha and J. T. Hupp, *Langmuir*, 2021, **37**, 9405-9414.
265. A. Demessence, C. Boissière, D. Grosso, P. Horcajada, C. Serre, G. Férey, G. J. A. A. Soler-Illia and C. Sanchez, *J. Mater. Chem.*, 2010, **20**.
266. C. J. Stephenson, J. T. Hupp and O. K. Farha, *Inorg. Chem. Front.*, 2015, **2**, 448-452.
267. X. Wang, M. Li, C. Cao, C. Liu, J. Liu, Y. Zhu, S. Zhang and W. Song, *ChemCatChem*, 2016, **8**, 3224-3228.
268. Y. Zhao, X. Ni, S. Ye, Z.-G. Gu, Y. Li and T. Ngai, *Langmuir*, 2020, **36**, 2037-2043.
269. Y. Yang, F. Wang, Q. Yang, Y. Hu, H. Yan, Y.-Z. Chen, H. Liu, G. Zhang, J. Lu, H.-L. Jiang and H. Xu, *ACS Appl. Mater. Interfaces*, 2014, **6**, 18163-18171.
270. P. Deria, J. E. Mondloch, O. Karagiaridi, W. Bury, J. T. Hupp and O. K. Farha, *Chem. Soc. Rev.*, 2014, **43**, 5896-5912.
271. M. Kim, J. F. Cahill, H. Fei, K. A. Prather and S. M. Cohen, *J. Am. Chem. Soc.*, 2012, **134**, 18082-18088.
272. C. J. Stephenson, J. T. Hupp and O. K. Farha, *Inorg. Chem.*, 2016, **55**, 1361-1363.
273. W. Zhang, G. Lu, C. Cui, Y. Liu, S. Li, W. Yan, C. Xing, Y. R. Chi, Y. Yang and F. Huo, *Adv. Mater.*, 2014, **26**, 4056-4060.
274. H. Liu, L. Chang, C. Bai, L. Chen, R. Luque and Y. Li, *Angew. Chem. Int. Ed.*, 2016, **55**, 5019-5023.
275. S. Navalon, M. Alvaro, A. Dhakshinamoorthy, H. Garcia, *Molecules*, 2019, **24**, 3050.

This journal is © The Royal Society of Chemistry 20xx

276. Y. Jiang, X. Zhang, X. Dai, Q. Sheng, H. Zhuo, J. Yong, Y. Wang, K. Yu, L. Yu, C. Luan, H. Wang, Y. Zhu, X. Duan and P. Che, *Chem. Mater.*, 2017, **29**, 6336-6345.
277. C. Rösler, S. Dissegna, V. L. Rechac, M. Kauer, P. Guo, S. Turner, K. Ollegott, H. Kobayashi, T. Yamamoto, D. Peeters, Y. Wang, S. Matsumura, G. Van Tendeloo, H. Kitagawa, M. Muhler, F. X. Llabrés i Xamena and R. A. Fischer, *Chem. Eur. J.*, 2017, **23**, 3583-3594.
278. L. Chen, W. Zhan, H. Fang, Z. Cao, C. Yuan, Z. Xie, Q. Kuang and L. Zheng, *Chem. Eur. J.*, 2017, **23**, 11397-11403.
279. C. J. Stephenson, C. L. Whitford, P. C. Stair, O. K. Farha and J. T. Hupp, *ChemCatChem*, 2016, **8**, 855-860.
280. Z. Guo, C. Xiao, R. V. Maligal-Ganesh, L. Zhou, T. W. Goh, X. Li, D. Tesfagaber, A. Thiel and W. Huang, *ACS Catal.*, 2014, **4**, 1340-1348.
281. S. Zheng, P. Yang, F. Zhang, D.-L. Chen and W. Zhu, *Chem. Eng. J.*, 2017, **328**, 977-987.
282. L. Chang and Y. Li, *Mol. Catal.*, 2017, **433**, 77-83.
283. B. Rungtaweevoranit, J. Baek, J. R. Araujo, B. S. Archanjo, K. M. Choi, O. M. Yaghi and G. A. Somorjai, *Nano Lett.*, 2016, **16**, 7645-7649.
284. H. Kobayashi, J. M. Taylor, Y. Mitsuka, N. Ogiwara, T. Yamamoto, T. Toriyama, S. Matsumura and H. Kitagawa, *Chem. Sci.*, 2019, **10**, 3289-3294.
285. Y. Zhu, J. Zheng, J. Ye, Y. Cui, K. Koh, L. Kovarik, D. M. Camaioni, J. L. Fulton, D. G. Truhlar, M. Neurock, C. J. Cramer, O. Y. Gutierrez and J. A. Lercher, *Nat. Commun.*, 2020, **11**, 5849.
286. B. An, J. Zhang, K. Cheng, P. Ji, C. Wang and W. Lin, *J. Am. Chem. Soc.*, 2017, **139**, 3834-3840.
287. E. S. Gutterød, S. Øien-Ødegaard, K. Bossers, A.-E. Nieuwelink, M. Manzoli, L. Braglia, A. Lazzarini, E. Borfecchia, S. Ahmadigoltapeh, B. Bouchevreau, B. T. Lønstad-Bleken, R. Henry, C. Lamberti, S. Bordiga, B. M. Weckhuysen, K. P. Lillerud and U. Olsbye, *Ind. Eng. Chem. Res.*, 2017, **56**, 13206-13218.
288. E. S. Gutterod, A. Lazzarini, T. Fjermestad, G. Kaur, M. Manzoli, S. Bordiga, S. Svelle, K. P. Lillerud, E. Skulason, S. Oien-Odegaard, A. Nova and U. Olsbye, *J. Am. Chem. Soc.*, 2020, **142**, 999-1009.
289. E. S. Gutterod, S. H. Pulumati, G. Kaur, A. Lazzarini, B. G. Solemsli, A. E. Gunnaes, C. Ahoba-Sam, M. E. Kalyva, J. A. Sannes, S. Svelle, E. Skulason, A. Nova and U. Olsbye, *J. Am. Chem. Soc.*, 2020, **142**, 17105-17118.
290. X. Wang, X. Zhang, P. Li, K.-i. Otake, Y. Cui, J. Lyu, M. D. Krzyaniak, Y. Zhang, Z. Li, J. Liu, C. T. Buru, T. Islamoglu, M. R. Wasielewski, Z. Li and O. K. Farha, *J. Am. Chem. Soc.*, 2019, **141**, 8306-8314.
291. X. Wang, X. Zhang, R. Pandharkar, J. Lyu, D. Ray, Y. Yang, S. Kato, J. Liu, M. C. Wasson, T. Islamoglu, Z. Li, J. T. Hupp, C. J. Cramer, L. Gagliardi and O. K. Farha, *ACS Catal.*, 2020, **10**, 8995-9005.
292. Z. Li, A. W. Peters, V. Bernales, M. A. Ortuno, N. M. Schweitzer, M. R. DeStefano, L. C. Gallington, A. E. Platero-Prats, K. W. Chapman, C. J. Cramer, L. Gagliardi, J. T. Hupp and O. K. Farha, *ACS Cent. Sci.*, 2017, **3**, 31-38.
293. B. Yang, J. I. Wheeler, B. Sorensen, R. Steagall, T. Nielson, J. Yao, J. Mendez-Arroyo and D. H. Ess, *Mater. Adv.*, 2021, **2**, 4246-4254.
294. C. A. Trickett, T. M. Osborn Popp, J. Su, C. Yan, J. Weisberg, A. Huq, P. Urban, J. Jiang, M. J. Kalmutzki, Q. Liu, J. Baek, M. P. Head-Gordon, G. A. Somorjai, J. A. Reimer and O. M. Yaghi, *Nat. Chem.*, 2019, **11**, 170-176.
295. A. J. Howarth, T. C. Wang, S. S. Al-Juaid, S. G. Aziz, J. T. Hupp and O. K. Farha, *Dalton Trans.*, 2016, **45**, 93-97.
296. J. M. Fernández-Morales, L. A. Lozano, E. Castillejos-López, I. Rodríguez-Ramos, A. Guerrero-Ruiz and J. M. Zamaro, *Microporous Mesoporous Mater.*, 2019, **290**, 109686.
297. L. H. T. Nguyen, T. T. Nguyen, H. L. Nguyen, T. L. H. Doan and P. H. Tran, *Catal. Sci. Technol.*, 2017, **7**, 4346-4350.
298. J. Jiang, F. Gandara, Y. B. Zhang, K. Na, O. M. Yaghi and W. G. Klemperer, *J. Am. Chem. Soc.*, 2014, **136**, 12844-12847.
299. K.-i. Otake, J. Ye, M. Mandal, T. Islamoglu, C. T. Buru, J. T. Hupp, M. Delferro, D. G. Truhlar, C. J. Cramer and O. K. Farha, *ACS Catal.*, 2019, **9**, 5383-5390.
300. J. Liu, J. Ye, Z. Li, K.-i. Otake, Y. Liao, A. W. Peters, H. Noh, D. G. Truhlar, L. Gagliardi, C. J. Cramer, O. K. Farha and J. T. Hupp, *J. Am. Chem. Soc.*, 2018, **140**, 11174-11178.
301. J. Liu, Z. Li, X. Zhang, K.-i. Otake, L. Zhang, A. W. Peters, M. J. Young, N. M. Bedford, S. P. Letourneau, D. J. Mandia, J. W. Elam, O. K. Farha and J. T. Hupp, *ACS Catal.*, 2019, **9**, 3198-3207.
302. J. S. Lee, E. A. Kapustin, X. Pei, S. Llopis, O. M. Yaghi and F. D. Toste, *Chem*, 2020, **6**, 142-152.
303. K. A. Grice and C. P. Kubiak, in *CO2 Chemistry*, 2014, DOI: 10.1016/b978-0-12-420221-4.00005-6, pp. 163-188.
304. M. D. Sampson, A. D. Nguyen, K. A. Grice, C. E. Moore, A. L. Rheingold and C. P. Kubiak, *J. Am. Chem. Soc.*, 2014, **136**, 5460-5471.
305. M. Bourrez, M. Orio, F. Molton, H. Vezin, C. Duboc, A. Deronzier and S. Chardon-Noblat, *Angew. Chem. Int. Ed.*, 2014, **53**, 240-243.
306. C. Wang, Z. Xie, K. E. deKrafft and W. Lin, *J. Am. Chem. Soc.*, 2011, **133**, 13445-13454.
307. K. M. Choi, K. Na, G. A. Somorjai and O. M. Yaghi, *J. Am. Chem. Soc.*, 2015, **137**, 7810-7816.
308. X. Li, T. W. Goh, L. Li, C. Xiao, Z. Guo, X. C. Zeng and W. Huang, *ACS Catal.*, 2016, **6**, 3461-3468.
309. T. Islamoglu, Z. Chen, M. C. Wasson, C. T. Buru, K. O. Kirlikovali, U. Afrin, M. R. Mian and O. K. Farha, *Chem. Rev.*, 2020, **120**, 8130-8160.
310. J. E. Mondloch, M. J. Katz, W. C. Isley, 3rd, P. Ghosh, P. Liao, W. Bury, G. W. Wagner, M. G. Hall, J. B. DeCoste, G. W. Peterson, R. Q. Snurr, C. J. Cramer, J. T. Hupp and O. K. Farha, *Nat. Mater.*, 2015, **14**, 512-516.
311. M. J. Katz, S. Y. Moon, J. E. Mondloch, M. H. Beyzavi, C. J. Stephenson, J. T. Hupp and O. K. Farha, *Chem. Sci.*, 2015, **6**, 2286-2291.
312. T. Islamoglu, M. A. Ortuno, E. Proussaloglou, A. J. Howarth, N. A. Vermeulen, A. Atilgan, A. M. Asiri, C. J. Cramer and O. K. Farha, *Angew. Chem. Int. Ed.*, 2018, **57**, 1949-1953.
313. M. Kalaj, M. R. Momeni, K. C. Bentz, K. S. Barcus, J. M. Palomba, F. Paesani and S. M. Cohen, *Chem. Commun.*, 2019, **55**, 3481-3484.
314. M. Goldsmith, Y. Ashani, Y. Simo, M. Ben-David, H. Leader, I. Silman, J. L. Sussman and D. S. Tawfik, *Chem. Biol.*, 2012, **19**, 456-466.
315. H. B. Luo, A. J. Castro, M. C. Wasson, W. Flores, O. K. Farha and Y. Liu, *ACS Catal.*, 2021, **11**, 1424-1429.
316. N. S. Bobbitt, M. L. Mendonca, A. J. Howarth, T. Islamoglu, J. T. Hupp, O. K. Farha and R. Q. Snurr, *Chem. Soc. Rev.*, 2017, **46**, 3357-3385.

Please do not adjust margins

317. D. B. Dwyer, J. Liu, J. C. Gomez, T. M. Tovar, A. Davoodabadi, W. E. Bernier, J. B. DeCoste and W. E. Jones, Jr., *ACS Appl. Mater. Interfaces*, 2019, **11**, 31378-31385.
318. D. L. McCarthy, J. Liu, D. B. Dwyer, J. L. Troiano, S. M. Boyer, J. B. DeCoste, W. E. Bernier and J. W. E. Jones, *New J. Chem.*, 2017, **41**, 8748-8753.
319. A. W. Peters, Z. Li, O. K. Farha and J. T. Hupp, *ACS Nano*, 2015, **9**, 8484 - 8490.
320. H. Choi, A. W. Peters, H. Noh, L. C. Gallington, A. E. Platero-Prats, M. R. DeStefano, M. Rimoldi, S. Goswami, K. W. Chapman, O. K. Farha and J. T. Hupp, *ACS Appl. Energy Mater.*, 2019, **2**, 8695-8700.
321. H. Noh, Y. Yang, S. Ahn, A. W. Peters, O. K. Farha and J. T. Hupp, *J. Electrochem. Soc.*, 2019, **166**, H3154-H3158.
322. H. Noh, Y. Yang, X. Zhang, T. A. Goetjen, Z. H. Syed, Z. Lu, S. Ahn, O. K. Farha and J. T. Hupp, *ChemElectroChem*, 2020, **7**, 509-516.
323. H.-Q. Xu, S. Yang, X. Ma, J. Huang and H.-L. Jiang, *ACS Catal.*, 2018, **8**, 11615-11621.
324. Y. Guo, J. Tang, H. Qian, Z. Wang and Y. Yamauchi, *Chem. Mater.*, 2017, **29**, 5566-5573.
325. Y. Chen, P. Li, H. Noh, C. Kung, C. T. Buru, X. Wang, X. Zhang and O. K. Farha, *Angew. Chem. Int. Ed.*, 2019, **131**, 7764 - 7768.
326. Y. Chen, P. Li, J. Zhou, C. T. Buru, L. Aorević, P. Li, X. Zhang, M. M. Cetin, J. F. Stoddart, S. I. Stupp, M. R. Wasielewski and O. K. Farha, *J. Am. Chem. Soc.*, 2020, **142**, 1768 - 1773.
327. T. Uemura, D. Hiramatsu, Y. Kubota, M. Takata and S. Kitagawa, *Angew. Chem. Int. Ed.*, 2007, **46**, 4987-4990.
328. T. Uemura, R. Kitaura, Y. Ohta, M. Nagaoka and S. Kitagawa, *Angew. Chem. Int. Ed.*, 2006, **45**, 4112-4116.
329. X. Guo, S. Geng, M. Zhuo, Y. Chen, M. J. Zaworotko, P. Cheng and Z. Zhang, *Coord. Chem. Rev.*, 2019, **391**, 44-68.
330. C. Zhou, A. Li, D. Wang, E. Pan, X. Chen, M. Jia and H. Song, *Chem. Commun.*, 2019, **55**, 4071-4074.
331. S. Mochizuki, T. Kitao and T. Uemura, *Chem. Commun.*, 2018, **54**, 11843-11856.
332. B. Le Ouay and T. Uemura, *Isr. J. Chem.*, 2018, **58**, 995-1009.
333. F. Gao, L. Zhang, C. Yu, X. Yan, S. Zhang and X. Li, *Macromol. Rapid Commun.*, 2018, **39**, 1800002.
334. L. Chen, Y. Jiang, H. Huo, J. Liu, Y. Li, C. Li, N. Zhang and J. Wang, *Appl. Catal. A.*, 2020, **594**, 117457.
335. P. Deria, D. A. Gómez-Gualdrón, I. Hod, R. Q. Snurr, J. T. Hupp and O. K. Farha, *J. Am. Chem. Soc.*, 2016, **138**, 14449-14457.
336. J. Yuan, A. M. Fracaroli and W. G. Klemperer, *Organometallics*, 2016, **35**, 2149-2155.
337. H. Deng, S. Grunder, K. E. Cordova, C. Valente, H. Furukawa, M. Hmadeh, F. Gándara, A. C. Whalley, Z. Liu, S. Asahina, H. Kazumori, M. O'Keeffe, O. Terasaki, J. F. Stoddart and O. M. Yaghi, *Science*, 2012, **336**, 1018-1023.
338. M. T. Huxley, A. Burgun, H. Ghodrati, C. J. Coghlan, A. Lemieux, N. R. Champness, D. M. Huang, C. J. Doonan and C. J. Sumby, *J. Am. Chem. Soc.*, 2018, **140**, 6416-6425.
339. G. Bauer, D. Ongari, D. Tiana, P. Gäumann, T. Rohrbach, G. Pareras, M. Tarik, B. Smit and M. Ranocchiari, *Nat. Commun.*, 2020, **11**, 1059.
340. K. Manna, P. Ji, Z. Lin, F. X. Greene, A. Urban, N. C. Thacker and W. Lin, *Nat. Commun.*, 2016, **7**, 12610.
341. X. Ye and D. Liu, *Cryst. Growth Des.*, 2021, **21**, 4780-4804.
342. D. J. Xiao, J. Oktawiec, P. J. Milner and J. R. Long, *J. Am. Chem. Soc.*, 2016, **138**, 14371-14379.
343. G. Bauer, D. Ongari, X. Xu, D. Tiana, B. Smit and M. Ranocchiari, *J. Am. Chem. Soc.*, 2017, **139**, 18166-18169.
344. X. Zhang, Z. Huang, M. Ferrandon, D. Yang, L. Robison, P. Li, T. C. Wang, M. Delferro and O. K. Farha, *Nat. Catal.*, 2018, **1**, 356-362.
345. S. Ahn, S. L. Nauert, C. T. Buru, M. Rimoldi, H. Choi, N. M. Schweitzer, J. T. Hupp, O. K. Farha, and J. M. Notestein, *J. Am. Chem. Soc.*, 2018, **140**, 8535-8543.
346. Z. Sharifzadeh, K. Berijani and A. Morsali, *Coord. Chem. Rev.*, 2021, **445**, 214083.
347. W. Xuan, C. Ye, M. Zhang, Z. Chen and Y. Cui, *Chem. Sci.*, 2013, **4**, 3154-3159.
348. M. Banerjee, S. Das, M. Yoon, H. J. Choi, M. H. Hyun, S. M. Park, G. Seo and K. Kim, *J. Am. Chem. Soc.*, 2009, **131**, 7524-7525.
349. K. D. Nguyen, C. Kutzscher, S. Ehrling, I. Senkovska, V. Bon, M. de Oliveira, T. Gutmann, G. Buntkowsky and S. Kaskel, *J. Catal.*, 2019, **377**, 41-50.
350. L. Liu and S. G. Telfer, *J. Am. Chem. Soc.*, 2015, **137**, 3901-3909.
351. K. Berijani, A. Morsali and J. T. Hupp, *Catal. Sci. Technol.*, 2019, **9**, 3388-3397.
352. A. Gheorghe, B. Strudwick, D. M. Dawson, S. E. Ashbrook, S. Woutersen, D. Dubbeldam and S. Tanase, *Chem. Eur. J.*, 2020, **26**, 13957-13965.
353. X.-W. Dong, Y. Yang, J.-X. Che, J. Zuo, X.-H. Li, L. Gao, Y.-Z. Hu and X.-Y. Liu, *Green Chem.*, 2018, **20**, 4085-4093.
354. B. C. Bukowski, F. J. Keil, P. I. Ravikovitch, G. Sastre, R. Q. Snurr and M.-O. Coppens, *Adsorption*, 2021, **27**, 683-760.
355. W. Y. Gao, A. D. Cardenal, C. H. Wang and D. C. Powers, *Chem*, 2019, **25**, 3465-3476.
356. P. Li, R. C. Klet, S. Y. Moon, T. C. Wang, P. Deria, A. W. Peters, B. M. Klahr, H. J. Park, S. S. Al-Juaid, J. T. Hupp and O. K. Farha, *Chem. Commun.* , 2015, **51**, 10925-10928.
357. Y. Feng, Z. Wang, W. Fan, Z. Kang, S. Feng, L. Fan, S. Hu and D. Sun, *J. Mater. Chem. A*, 2020, **8**, 13132-13141.
358. X. Jiang, H. B. Duan, S. I. Khan and M. A. Garcia-Garibay, *ACS Cent. Sci.*, 2016, **2**, 608-613.
359. R. Wang, B. C. Bukowski, J. Duan, J. Sui, R. Q. Snurr and J. T. Hupp, *Chem. Mater.*, 2021, **33**, 6832-6840.
360. R. J. Drout, L. Robison, Z. Chen, T. Islamoglu and O. K. Farha, *Trends Chem.*, 2019, **1**, 304-317.
361. R. Wang, B. C. Bukowski, J. Duan, T. R. Sheridan, A. Atilgan, K. Zhang, R. Q. Snurr and J. T. Hupp, *Langmuir*, 2020, **36**, 10853-10859.
362. S. Hwang, A. Gopalan, M. Hovestadt, F. Piepenbreier, C. Chmelik, M. Hartmann, R. Q. Snurr and J. Karger, *Molecules*, 2018, **23**, 668.
363. W. Xiang, Y. Zhang, Y. Chen, C.-j. Liu and X. Tu, *J. Mater. Chem. A*, 2020, **8**, 21526-21546.
364. R. A. Dodson, A. G. Wong-Foy and A. J. Matzger, *Chemistry of Materials*, 2018, **30**, 6559-6565.
365. L. Heinke, Z. Gu and C. Woll, *Nat. Commun.*, 2014, **5**, 4562.
366. M. Gao, H. Li, M. Yang, S. Gao, P. Wu, P. Tian, S. Xu, M. Ye and Z. Liu, *Commun. Chem.*, 2019, **2**, 1-10.
367. F. Hibbe, C. Chmelik, L. Heinke, S. Pramanik, J. Li, D. M. Ruthven, D. Tzoulaki and J. Karger, *J. Am. Chem. Soc.*, 2011, **133**, 2804-2807.
368. F. G. Cirujano, N. Martin and L. H. Wee, *Chem. Mater.*, 2020, **32**, 10268-10295.

This journal is © The Royal Society of Chemistry 20xx

369. J. Lyu, X. Zhang, P. Li, X. Wang, C. T. Buru, P. Bai, X. Guo and O. K. Farha, *Chem. Mater.*, 2019, **31**, 4166-4172.
370. J. W. Maina, C. Pozo-Gonzalo, L. Kong, J. Schütz, M. Hill and L. F. Dumée, *Mater. Horiz.*, 2017, **4**, 345-361.
371. B. Ugale, S. S. Dhankhar and C. M. Nagaraja, *Inorg. Chem.*, 2016, **55**, 9757-9766.
372. P.-Z. Li, X.-J. Wang, J. Liu, J. S. Lim, R. Zou and Y. Zhao, *J. Am. Chem. Soc.*, 2016, **138**, 2142-2145.
373. Y. Wang, H. Cui, Z.-W. Wei, H.-P. Wang, L. Zhang and C.-Y. Su, *Chem. Sci.*, 2017, **8**, 775-780.
374. D. Feng, W. C. Chung, Z. Wei, Z. Y. Gu, H. L. Jiang, Y. P. Chen, D. J. Darensbourg and H. C. Zhou, *J. Am. Chem. Soc.*, 2013, **135**, 17105-17110.
375. B. Abeykoon, T. Devic, J.-M. Grenèche, A. Fateeva and A. B. Sorokin, *Chem. Commun.*, 2018, **54**, 10308-10311.
376. A. E. Allen and D. W. Macmillan, *Chem. Sci.*, 2012, **2012**, 633-658.
377. F. X. Felpin and E. Fouquet, *ChemSusChem*, 2008, **1**, 718-724.
378. V. R. Bakuru, D. Davis and S. B. Kalidindi, *Dalton Trans.*, 2019, **48**, 8573-8577.
379. B. Rungtaweevoranit, Y. Zhao, K. M. Choi and O. M. Yaghi, *Nano Res.*, 2016, **9**, 47-58.
380. A. H. Chughtai, N. Ahmad, H. A. Younus, A. Laypkov and F. Verpoort, *Chem. Soc. Rev.*, 2015, **44**, 6804-6849.
381. C. D. Wu and M. Zhao, *Adv. Mater.*, 2017, **29**.
382. Y. B. Huang, J. Liang, X. S. Wang and R. Cao, *Chem. Soc. Rev.*, 2017, **46**, 126-157.
383. Z. Lin, Z.-M. Zhang, Y.-S. Chen and W. Lin, *Angew. Chem. Int. Ed.*, 2016, **55**, 13739 - 13743.
384. B. An, Z. Li, Y. Song, J. Zhang, L. Zeng, C. Wang and W. Lin, *Nat. Catal.*, 2019, **2**, 709-717.
385. S. S. Fu, X. Y. Ren, S. Guo, G. Lan, Z. M. Zhang, T. B. Lu and W. Lin, *iScience*, 2020, **23**, 100793.
386. X. Gu, Z. H. Lu, H. L. Jiang, T. Akita and Q. Xu, *J. Am. Chem. Soc.*, 2011, **133**, 11822-11825.
387. H. D. Park, M. Dinca and Y. Roman-Leshkov, *ACS Cent. Sci.*, 2017, **3**, 444-448.
388. P. M. Usov, S. R. Ahrenholtz, W. A. Maza, B. Stratakes, C. C. Epley, M. C. Kessinger, J. Zhu and A. J. Morris, *J. Mater. Chem. A*, 2016, **4**, 16818-16823.
389. J. E. Mondloch, W. Bury, D. Fairen-Jimenez, S. Kwon, E. J. DeMarco, M. H. Weston, A. A. Sarjeant, S. T. Nguyen, P. C. Stair, R. Q. Snurr, O. K. Farha and J. T. Hupp, *J. Am. Chem. Soc.*, 2013, **135**, 10294-10297.
390. L. Zeng, Z. Wang, Y. Wang, J. Wang, Y. Guo, H. Hu, X. He, C. Wang and W. Lin, *J. Am. Chem. Soc.*, 2020, **142**, 75-79.
391. M. Lee, A. De Riccardis, R. V. Kazantsev, J. K. Cooper, A. K. Buckley, P. W. W. Burroughs, D. M. Larson, G. Mele and F. M. Toma, *ACS Appl. Energy Mater.*, 2020, **3**, 1286-1291.
392. C. Prasittichai, J. R. Avila, O. K. Farha and J. T. Hupp, *J. Am. Chem. Soc.*, 2013, **135**, 16328-16331.
393. S. Andonova, E. Ivanova, J. Yang and K. Hadjiivanov, *J. Phys. Chem. C*, 2017, **121**, 18665-18673.
394. X. Qian, B. Yadian, R. Wu, Y. Long, K. Zhou, B. Zhu and Y. Huang, *Int. J. Hydrog. Energy*, 2013, **38**, 16710-16715.
395. J.-C. Wasilke, S. J. Obrey, R. T. Baker and G. C. Bazan, *Chem. Rev.*, 2005, **105**, 1001 - 1020.
396. T. L. Lohr and T. J. Marks, *Nat. Chem.*, 2015, **7**, 477-482.
397. M. Huang, Y. Li, M. Li, J. Zhao, Y. Zhu, C. Wang and V. K. Sharma, *Environ. Sci. Technol.*, 2019, **53**, 3610-3619.
398. M. J. Climent, A. Corma, S. Iborra and M. J. Sabater, *ACS Catal.*, 2014, **4**, 870-891.
399. P. Ji, T. Drake, A. Murakami, P. Oliveres, J. H. Skone and W. Lin, *J. Am. Chem. Soc.*, 2018, **140**, 10553-10561.
400. S. Li, W. Wang, S. Lei and J. z. Cui, *ChemistrySelect*, 2021, **6**, 7732-7735.
401. X. Zhang, Z. Chen, X. Liu, S. L. Hanna, X. Wang, R. Taheri-Ledari, A. Maleki, P. Li and O. K. Farha, *Chem. Soc. Rev.*, 2020, **49**, 7406-7427.
402. J. Liu, Z. Lu, Z. Chen, M. Rimoldi, A. J. Howarth, H. Chen, S. Alayoglu, R. Q. Snurr, O. K. Farha and J. T. Hupp, *ACS Appl. Mater. Interfaces*, 2021, **13**, 20081-20093.
403. J. Liu, Z. Chen, R. Wang, S. Alayoglu, T. Islamoglu, S.-J. Lee, T. R. Sheridan, H. Chen, R. Q. Snurr, O. K. Farha and J. T. Hupp, *ACS Appl. Mater. Interfaces*, 2021, **13**, 22485-22494.
404. J. Jiang and O. M. Yaghi, *Chem. Rev.*, 2015, **115**, 6966-6997.
405. W. Gong, X. Chen, H. Jiang, D. Chu, Y. Cui and Y. Liu, *J. Am. Chem. Soc.*, 2019, **141**, 7498-7508.
406. L. Feng, Y. Wang, S. Yuan, K.-Y. Wang, J.-L. Li, G. S. Day, D. Qiu, L. Cheng, W.-M. Chen, S. T. Madrahimov and H.-C. Zhou, *ACS Catal.*, 2019, **9**, 5111-5118.
407. J. Turconi, F. Griolet, R. Guevel, G. Oddon, R. Villa, A. Geatti, M. Hvala, K. Rossen, R. Göller and A. Burgard, *Org. Process Res. Dev.*, 2014, **18**, 417-422.
408. K. Li, J. Yang, R. Huang, S. Lin and J. Gu, *Angew. Chem. Int. Ed.*, 2020, **59**, 14124-14128.
409. G. Cai, P. Yan, L. Zhang, H. C. Zhou and H. L. Jiang, *Chem. Rev.*, 2021, DOI: 10.1021/acs.chemrev.1c00243.
410. K. Li, S. Lin, Y. Li, Q. Zhuang and J. Gu, *Angew. Chem. Int. Ed.*, 2018, **57**, 3439-3443.
411. X. Lian, Y. P. Chen, T. F. Liu and H. C. Zhou, *Chem. Sci.*, 2016, **7**, 6969-6973.
412. R. Limvorapitux, L.-Y. Chou, A. P. Young, C.-K. Tsung and S. T. Nguyen, *ACS Catal.*, 2017, **7**, 6691-6698.
413. J. Zhuang, A. P. Young and C. K. Tsung, *Small*, 2017, **13**, 1700880.
414. P. Deria, S. Li, H. Zhang, R. Q. Snurr, J. T. Hupp and O. K. Farha, *Chem. Commun.*, 2015, **51**, 12478-12481.
415. A. M. Fracaroli, P. Siman, D. A. Nagib, M. Suzuki, H. Furukawa, F. D. Toste and O. M. Yaghi, *J. Am. Chem. Soc.*, 2016, **138**, 8352-8355.
416. C. Marti-Gastaldo, D. Antypov, J. E. Warren, M. E. Briggs, P. A. Chater, P. V. Wiper, G. J. Miller, Y. Z. Khimyak, G. R. Darling, N. G. Berry and M. J. Rosseinsky, *Nat. Chem.*, 2014, **6**, 343-351.
417. T. Schnitzer, E. Paenurk, N. Trapp, R. Gershoni-Poranne and H. Wennemers, *J. Am. Chem. Soc.*, 2021, **143**, 644-648.
418. X. Han, W. Lu, Y. Chen, I. da Silva, J. Li, L. Lin, W. Li, A. M. Sheveleva, H. G. W. Godfrey, Z. Lu, F. Tuna, E. J. L. McInnes, Y. Cheng, L. L. Daemen, L. J. M. McPherson, S. J. Teat, M. D. Frogley, S. Rudic, P. Manuel, A. J. Ramirez-Cuesta, S. Yang and M. Schroder, *J. Am. Chem. Soc.*, 2021, **143**, 3153-3161.
419. F. Drache, F. G. Cirujano, K. D. Nguyen, V. Bon, I. Senkovska, F. X. Llabrés i Xamena and S. Kaskel, *Cryst. Growth Des.*, 2018, **18**, 5492-5500.
420. D. W. Lim, M. Sadakiyo and H. Kitagawa, *Chem. Sci.*, 2019, **10**, 16-33.
421. L. C. Applegate and T. Z. Forbes, *CrystEngComm*, 2020, **22**, 3406-3418.
422. S. M. Towsif Abtab, D. Alezi, P. M. Bhatt, A. Shkurenko, Y. Belmabkhout, H. Aggarwal, Ł. J. Weseliński, N. Alsadun, U.

Samin, M. N. Hedhili and M. Eddaoudi, *Chem*, 2018, **4**, 94-105.

423. X. Liu, X. Wang and F. Kapteijn, *Chem. Rev.*, 2020, **120**, 8303-8377.
424. S. Dutta, N. Kumari, S. Dubbu, S. W. Jang, A. Kumar, H. Ohtsu, J. Kim, S. H. Cho, M. Kawano and I. S. Lee, *Angew. Chem. Int. Ed.*, 2020, **59**, 3416-3422.
425. B. Gole, U. Sanyal, R. Banerjee and P. S. Mukherjee, *Inorg. Chem.*, 2016, **55**, 2345-2354.
426. S. Rojas-Buzo, P. Concepcion, J. L. Olloqui-Sariego, M. Moliner and A. Corma, *ACS Appl. Mater. Interfaces*, 2021, **13**, 31021-31030.
427. M. Mon, R. Adam, J. Ferrando−Soria, A. Corma, D. Armentano, E. Pardo and A. Leyva−Pérez, *ACS Catal.*, 2018, **8**, 10401-10406.
428. M. Mon, M. A. Rivero-Crespo, J. Ferrando-Soria, A. Vidal-Moya, M. Boronat, A. Leyva-Perez, A. Corma, J. C. Hernandez-Garrido, M. Lopez-Haro, J. J. Calvino, G. Ragazzon, A. Credi, D. Armentano and E. Pardo, *Angew. Chem. Int. Ed.*, 2018, **57**, 6186-6191.
429. M. A. Rivero-Crespo, M. Mon, J. Ferrando-Soria, C. W. Lopes, M. Boronat, A. Leyva-Perez, A. Corma, J. C. Hernandez-Garrido, M. Lopez-Haro, J. J. Calvino, E. V. Ramos-Fernandez, D. Armentano and E. Pardo, *Angew. Chem. Int. Ed.*, 2018, **57**, 17094-17099.
430. B. Villoria-Del-Alamo, S. Rojas-Buzo, P. Garcia-Garcia and A. Corma, *Chem*, 2021, **27**, 4588-4598.
431. Y. Zhu, W. D. Wang, X. Sun, M. Fan, X. Hu and Z. Dong, *ACS Appl. Mater. Interfaces*, 2020, **12**, 7285-7294.
432. C. Cuadrado-Collados, G. Mouchaham, L. Daemen, Y. Cheng, A. Ramirez-Cuesta, H. Aggarwal, A. Missyul, M. Eddaoudi, Y. Belmabkhout and J. Silvestre-Albero, *J. Am. Chem. Soc.*, 2020, **142**, 13391-13397.
433. K. Epp, B. Bueken, B. J. Hofmann, M. Cokoja, K. Hemmer, D. De Vos and R. A. Fischer, *Catal. Sci. Technol.*, 2019, **9**, 6452-6459.
434. K. Hemmer, M. Cokoja and R. A. Fischer, *ChemCatChem*, 2021, **13**, 1683-1691.
435. S. Sartipi, M. J. Valero Romero, E. Rozhko, Z. Que, H. A. Stil, J. de With, F. Kapteijn and J. Gascon, *ChemCatChem*, 2015, **7**, 3243-3247.
436. I. Yarulina, S. Bailleul, A. Pustovarenko, J. R. Martinez, K. D. Wispelaere, J. Hajek, B. M. Weckhuysen, K. Houben, M. Baldus, V. Van Speybroeck, F. Kapteijn and J. Gascon, *ChemCatChem*, 2016, **8**, 3057-3063.
437. D. Y. Osadchii, A. I. Olivos-Suarez, Á. Szécsényi, G. Li, M. A. Nasalevich, I. A. Dugulan, P. S. Crespo, E. J. M. Hensen, S. L. Veber, M. V. Fedin, G. Sankar, E. A. Pidko and J. Gascon, *ACS Catal.*, 2018, **8**, 5542-5548.
438. C. Kutzscher, G. Nickerl, I. Senkovska, V. Bon and S. Kaskel, *Chem. Mater.*, 2016, **28**, 2573-2580.
439. U. S. F. Arrozi, V. Bon, S. Krause, T. Lubken, M. S. Weiss, I. Senkovska and S. Kaskel, *Inorg. Chem.*, 2020, **59**, 350-359.
440. H. Kobayashi, Y. Mitsuka and H. Kitagawa, *Inorg. Chem.*, 2016, **55**, 7301-7310.
441. N. Ogiwara, H. Kobayashi, M. Inukai, Y. Nishiyama, P. Concepcion, F. Rey and H. Kitagawa, *Nano Lett.*, 2020, **20**, 426-432.
442. B. M. Weckhuysen, S. Kitagawa and M. Tsapatsis, *ChemPhysChem*, 2018, **19**, 339-340.
443. M. I. Gonzalez, A. B. Turkiewicz, L. E. Darago, J. Oktawiec, K. Bustillo, F. Grandjean, G. J. Long and J. R. Long, *Nature*, 2020, **577**, 64-68.
444. R. Abazari, L. Esrafili, A. Morsali, Y. Wu and J. Gao, *Appl. Catal. B.* , 2021, **283**, 119582.
445. F. Afshariazar and A. Morsali, *Cryst. Growth Des.*, 2019, **19**, 4239-4245.
446. A. Grigoropoulos, G. F. S. Whitehead, N. Perret, A. P. Katsoulidis, F. M. Chadwick, R. P. Davies, A. Haynes, L. Brammer, A. S. Weller, J. Xiao and M. J. Rosseinsky, *Chem. Sci.*, 2016, **7**, 2037-2050.
447. T. N. Nguyen, S. Kampouri, B. Valizadeh, W. Luo, D. Ongari, O. M. Planes, A. Zuttel, B. Smit and K. C. Stylianou, *ACS Appl. Mater. Interfaces*, 2018, **10**, 30035-30039.
448. S. Kampouri, T. N. Nguyen, C. P. Ireland, B. Valizadeh, F. M. Ebrahim, G. Capano, D. Ongari, A. Mace, N. Guijarro, K. Sivula, A. Sienkiewicz, L. Forró, B. Smit and K. C. Stylianou, *J. Mater. Chem. A*, 2018, **6**, 2476-2481.
449. M. Lammert, M. T. Wharmby, S. Smolders, B. Bueken, A. Lieb, K. A. Lomachenko, D. D. Vos and N. Stock, *Chem. Commun.*, 2015, **51**, 12578-12581.
450. N. Reimer, B. Bueken, S. Leubner, C. Seidler, M. Wark, D. De Vos and N. Stock, *Chem*, 2015, **21**, 12517-12524.
451. A. Dhakshinamoorthy, N. Heidenreich, D. Lenzen and N. Stock, *CrystEngComm*, 2017, **19**, 4187-4193.
452. N. Van Velthoven, S. Waitschat, S. M. Chavan, P. Liu, S. Smolders, J. Vercammen, B. Bueken, S. Bals, K. P. Lillerud, N. Stock and D. E. De Vos, *Chem. Sci.*, 2019, **10**, 3616-3622.
453. H. Yang, S. J. Bradley, A. Chan, G. I. Waterhouse, T. Nann, P. E. Kruger and S. G. Telfer, *J. Am. Chem. Soc.*, 2016, **138**, 11872-11881.
454. L. Liu, T. Y. Zhou and S. G. Telfer, *J. Am. Chem. Soc.*, 2017, **139**, 13936-13943.
455. T. Y. Zhou, B. Auer, S. J. Lee and S. G. Telfer, *J. Am. Chem. Soc.*, 2019, **141**, 1577-1582.
456. M. W. Logan, S. Ayad, J. D. Adamson, T. Dilbeck, K. Hanson and F. J. Uribe-Romo, *J. Mater. Chem. A*, 2017, **5**, 11854-11863.
457. X. Yang, T. Liang, J. Sun, M. J. Zaworotko, Y. Chen, P. Cheng and Z. Zhang, *ACS Catal.*, 2019, **9**, 7486-7493.